Ultrafast Dynamics in condensed matter

University of Potsdam

Masters thesis

Magnetization Dynamics in Metallic Heterostructures studied by a combination of tr-MOKE and UXRD

Author:

Jasmin Jarecki

First Examiner:
Prof. Dr. Matias Bargheer
Universität Potsdam

Second Examiner:
Dr. Clemens von Korff-Schmising
Max-Born Institut, Berlin

Faculty of Mathematics and Science
Institute of Physics and Astronomy
April 30, 2023

Abstract

In this thesis I study the response of the magnetic system of a ferromagnetic nickel layer buried in a metallic heterostructure to ultrafast laser excitation. Combining time-resolved magneto-optical Kerr effect (MOKE) experiments and ultrafast x-ray diffraction (UXRD), which detect the transient magnetization and lattice dynamics, respectively, provides a comprehensive picture of the laser-induced dynamics within the investigated sample structures. For a systematic analysis, in addition to a sample of Pt, Cu and Ni, which is characterized by an indirect energy transfer by hot electrons into the buried nickel, two other samples with an integrated MgO layer are considered. The insulating film modifies the initial energy distribution, the subsequent heat transport and therefore also the resulting lattice and magnetization dynamics. UXRD provides a quantitative characterization of strain dynamics in each sample and a calibration of the related temperatures, which are obtained by simulations of the strain response on the basis of a two-temperatures model. The information gained from this is further used in the analysis of two different aspects of magnetization dynamics, namely ultrafast demagnetization and magnetization precession.

In the first part, I focus on modeling the measured magnetization dynamics upon slow and ultrafast excitation within the framework of the microscopic three-temperatures model (m3TM). Comparison with measured MOKE transients shows that it is not sufficient to describe the fast magnetization dynamics by a simple dependence on electron and phonon temperature. At the center of the second part is the excitation of magnetization precession by various driving mechanisms, such as demagnetization or magneto-acoustics, whose respective contributions are identified by the UXRD measurements. Based on systematic MOKE experiments and simulations in the framework of the Landau-Lifshitz-Gilbert equation, it can be shown that it is the laser-induced lattice dynamics that essentially determines precession dynamics in nickel.

Kurzfassung

In dieser Arbeit wird die laserinduzierte Magnetisierungsdynamik in Nickel untersucht, das in einer metallischen Heterostruktur eingebettet ist. Es wird eine Kombination aus zeitaufgelösten magneto-optischen Kerr Effekt (MOKE) Experimenten und ultraschneller Röntgenbeugung (UXRD) verwendet, die jeweils die transiente Magnetisierung und die Gitterdynamik detektieren, um ein möglichst vollständiges Bild der laserinduzierten Dynamik in den betrachteten Proben zu erhalten. Für eine systematische Analyse werden neben einer Probe aus Pt, Cu und Ni, die durch einen indirekten Energieeintrag durch heiße Elektronen in das Nickel charakterisiert ist, zwei weitere Proben betrachtet, in die jeweils eine nicht-leitende MgO-Schicht integriert ist, welche die initiale Energieverteilung, das Wärmetransportverhalten und somit auch die gesamte Gitter- und Magnetisierungsdynamik verändert. Mithilfe des UXRD-Experiments wird die Gitterdynamik in jeder Probe quantitativ charakterisiert und die damit verknüpfte Temperaturdynamik kalibriert, indem die UXRD-Messungen unter Verwendung eines zwei-Temperatur-Modells simuliert werden. Die daraus gewonnen Erkenntnisse werden im Weiteren bei der Analyse zweier unterschiedlicher Aspekte der Magnetisierungsdynamik verwendet, nämlich der ultraschnellen Demagnetisierung und der Magnetisierungspräzession.

Im ersten Teil liegt der Fokus auf der Beschreibung der gemesssenen Demagnetisierung anhand des mikroskopischen drei-Temperaturmodells (m3TM) nach ultraschneller sowie langsamer Anregung. Der Vergleich von Simulation und Messdaten zeigt allerdings, dass es nicht ausreichend ist, die schnelle Magnetisierungsdynamik durch eine einfache Abhängigkeit von der Elektronen- und Phononentemperaturen zu beschreiben. Weiterhin steht im Mittelpunkt des zweiten Teils die Anregung von Magnetisierungspräzession durch verschiedene laserinduzierte Effekte wie Demagnetisierung oder Magneto-Akustik, deren Beitrag durch die UXRD Messungen identifiziert wird. Auf Grundlage systematischer MOKE-Experimente und Simulationen im Rahmen der Landau-Lifshitz-Gilbert Gleichung kann gezeigt werden, dass es die laserinduzierte Gitterdynamik ist, die die Präzessionsdynamik in Nickel wesentlich bestimmt.

Contents

Introduction

The perspective of controlling magnetization dynamics on ultrafast timescales has attracted much attention in modern solid-state research [1–4], not only from a fundamental point of view, but also because of the promising possibilities regarding its applications in data storage and data processing devices. The response of the magnetic system to ultrafast excitation includes a variety of effects, such as ultrafast demagnetization [5–7], magnetization precession [8–10] or all optical magnetization switching [11–13], fueling visions of revolutionizing magnetic information memory technologies and data processing regarding their speed and energy efficiency. To this end, reliable predictions of the magnetic behavior and, accordingly, understanding of the microscopic processes is of crucial importance, animating ongoing experimental and theoretical efforts.

With regard to possible applications, the integration of magnetic materials in heterostructures is of particular interest, since only the combination of materials with different properties leads to functionality. On the one hand, this drastically expands the number of degrees of freedom, further complicating the situation, but on the other hand, it opens up a wide range of possibilities to shape the initial energy distribution as well as the subsequent heat transport and so also the spin dynamics [14–16]. Recently, interest has been aroused in the manipulation of spin dynamics by hot electrons excited in a transducer layer and subsequently depositing energy in a magnetic film by very fast electronic transport through an opaque metal layer, which has been shown to be as efficient as direct laser excitation [4, 17–19]. Using such structures enables, for example, adjusting the duration of the excitation of the magnetic system precisely by small changes in the metallic structure on top of the magnetic layer, leading to a variation of the demagnetization time [20, 21]. Demagnetization in a ferromagnet plays a central role in magnetization dynamics, since it occurs whenever heat is involved. This phenomenon is closely related to subsequent spin dynamics and can trigger all-optical switching [22, 23] or magnetization precession [8]. In addition to demagnetization-induced spin-wave excitation, magnetization precession can be also driven by other laser-induced effects, such as changes of the temperature-dependent magneto-crystalline anisotropy [24–26] or magneto-acoustics including both quasi-static strain [27] as well as propagating strain [10, 28–30], which provides a wide range of possibilities to control magnetization. Motivated by the idea of precessional switching of magnetization, it is important to find a way of efficient excitation of such a motion. To this end, heterostructures are also of great use in making further progress in this field, as they can be used to target the excitation of spin waves.

All these experiments have in common, regardless of the particular goal, that the resulting magnetization dynamics are closely linked to the dynamics of the other subsystems and that the macroscopic response of a magnetic material is mainly governed by the interplay between electrons, phonons, and spins. Therefore, it is of great advantage, if not mandatory, to include all subsystems in the experimental considerations in order to obtain a better understanding of magnetization phenomena. Combining time-resolved magneto-optical Kerr effect (MOKE) experiments and ultrafast x-ray diffraction (UXRD) represents a suitable approach, as shown by recent results [31, 32]. While MOKE experiments are a comparably simple method to detect the magnetization, UXRD measurements can quantify the lattice dynamics of the investigated system. In addition to

an exact characterization of the strain dynamics, it is also possible to obtain reliable information on electron and phonon temperatures due to the good understanding of this process [14, 15, 33, 34], which, together with the magnetization measurements, provides a much clearer picture of the overall dynamics.

In this thesis I study laser-induced magnetization dynamics of a thin nickel film integrated within a metallic heterostructure under varying temperature and strain dynamics. Excitation of the magnetic system is tailored by specific changes of the heat transport behavior by inserting isolating MgO-layers within the original Pt-Cu-Ni structure. Combining time-resolved MOKE experiments and UXRD yielding the transient magnetization and lattice dynamics, respectively, provides a comprehensive picture of the laser-induced dynamics of the total system. The thesis is structured as follows.

Chapter two reviews the physical concepts of laser-induced dynamics and origins of the macroscopic behaviors in solids, focusing on 3d transition metals. Parallels of strain and magnetization dynamics are highlighted, which are both governed by microscopic interactions between the involved subsystems, to clarify the complementary information comprised in these two macroscopic observables. The subsequent chapter summarizes the underlying experimental idea in more detail. First, the investigated sample structures and the corresponding properties regarding heat transport behavior and magnetism will be introduced, which is followed by a description of the experiments conducted within the scope of this thesis, i.e., MOKE and UXRD. In chapter four, I present the results of the UXRD experiments which characterize the strain dynamics of each metal layer within the heterostructure quantitatively. The calibrated spatio-temporal temperature profiles of the electrons and phonons, which are obtained by modeling the strain response taking into account a two-temperatures model, are shown here as well. The information gained from this is further used in the analysis of magnetization dynamics.

In the first part, I apply the calibrated thermophysical parameters calibrated to the electron and phonon temperature dynamics to the microscopic three-temperatures model (m3TM), which is commonly used to describe laser-induced demagnetization in ferromagnets. A comparison to the MOKE measurements reveals a good agreement between model and the transient magnetization in thermal equilibrium. Upon ultrafast excitation, however, the simulation greatly overestimates the initial demagnetization amplitude and underestimates the demagnetization time at early delays. The necessary acceleration of the energy transfer from electrons to phonons to describe both ultrafast demagnetization and the subsequent near-equilibrium after relaxation cannot be captured within the framework of the model.

In the second part, the efficiency of different driving mechanisms for magnetization precession in Ni is compared considering demagnetization, quasi-static strain, and propagating strain waves. The specific sample design of each Pt-Cu-Ni structure enables investigating the relevant effects separately, which are identified via UXRD in each sample. In the MOKE experiments, the orientation of the external field angle relative to the sample surface and thus the precession frequency is varied. Analyzing the angular dependence of the precession amplitudes demonstrates that a periodic change of the effective field by propagating strain waves represents the most efficient driving mechanism for magnetization precession, provided that pulse duration and the orbital frequency are resonant to the precession frequency. Off resonance, spin wave excitation is governed by thermal effects including demagnetization and rapid thermal expansion, which both induce a step-like change in the effective field. Furthermore, a closer look at the initial precession phase shows that the magneto-elastic field resulting from quasi-static strain represents the major contribution of the thermal mechanism. In addition to the conclusive experimental results, these findings are supported by simulations based on the Landau-Lifshitz-Gilbert equation, which involve the simulated temporal UXRD-strains.

Theory of Strain and Magnetization Dynamics

At the center of this thesis is the laser-induced magnetization dynamics of a thin nickel layer embedded within a metallic heterostructure. The behavior of the magnetization is determined not only by the excitation of the magnetic system itself but by the energy transfer processes between all degrees of freedom of the sample [5, 35]. Aiming to obtain a better picture of the sample's response to the laser excitation and the coupling between the subsystems, I use in addition to the separate magnetization measurements complementary experiments to access the strain dynamics providing essential information on the temperature dynamics of the whole structure.

To get an understanding of the relation between these fields, i.e., magnetization dynamics and strain dynamics, and of the relevant concepts in this context, I summarize the physical principles and results of previous works in this chapter. Therefore, I give a brief overview of the excited processes in metals after ultrafast laser irradiation and continue with explaining the generation of strain dynamics in more detail. Finally, I focus on the theory of two aspects of magnetization dynamics, i.e., ultrafast demagnetization and magnetization precession.

## 2.1 Metal response upon laser excitation

The understanding of ultrafast processes, especially at the nanoscale in solid state materials, is of great importance from an application-oriented point of view but interesting from the fundamental perspective as well. Technological progress enables advances in the physical insights, but at the same time, the increase of knowledge leads to an advancement of technology itself.

Even though properties of metals, semiconductors, and insulating solids have been investigated for decades, research efforts on this topic are not diminishing. One reason for that is the fact that existing models describing the behavior of solids in some cases are no longer sufficient at the decreasing length- and timescales that are accessible now [14, 15]. In this section I provide a rough overview of the effects and processes regarding laser-induced dynamics in metals in general, that are relevant within the scope of this thesis, and their observation by measurements of physical observables.

The experiments in the field of ultrafast dynamics are typically conducted in a pump-probe scheme. The basic principle is to excite a reversible process (pump) and measure the state of the system at a point in time relative to the excitation (probe). Those two steps are then repeated with varying delays of the probe, which provides a time-resolved picture of the system's behavior. Clearly, the reversibility of the excited processes is necessary for this measurement technique, and the subsequent excitation can take place only after equilibration of the system towards its initial state. In a pump-probe experiment, that studies the dynamics of a metal, the material usually gets excited by an ultrashort laser pulse (approx. 100 fs) of wavelengths that reach from the infrared to the optical part of the electromagnetic spectrum [5].

Probing is also often performed with an ultrashort laser pulse, however, its properties and the experimental details depend strongly on the underlying research question and the system. As an example, there are many experiments that use laser pulses with wavelengths in the visible, such as transient reflectivity measurements sensitive to changes of the refractive index of a material [36, 37].

The time-dependent reflection intensity of the delayed probe pulse contains information, e.g., about the electron-phonon interaction or strain propagation [38–40]. Another optical experiment in a similar setting is the time-resolved magneto-optical Kerr effect measurement (tr-MOKE). Here, the rotation of the polarization angle of the reflected probe beam is analyzed, which is proportional to the magnetization [41, 42].
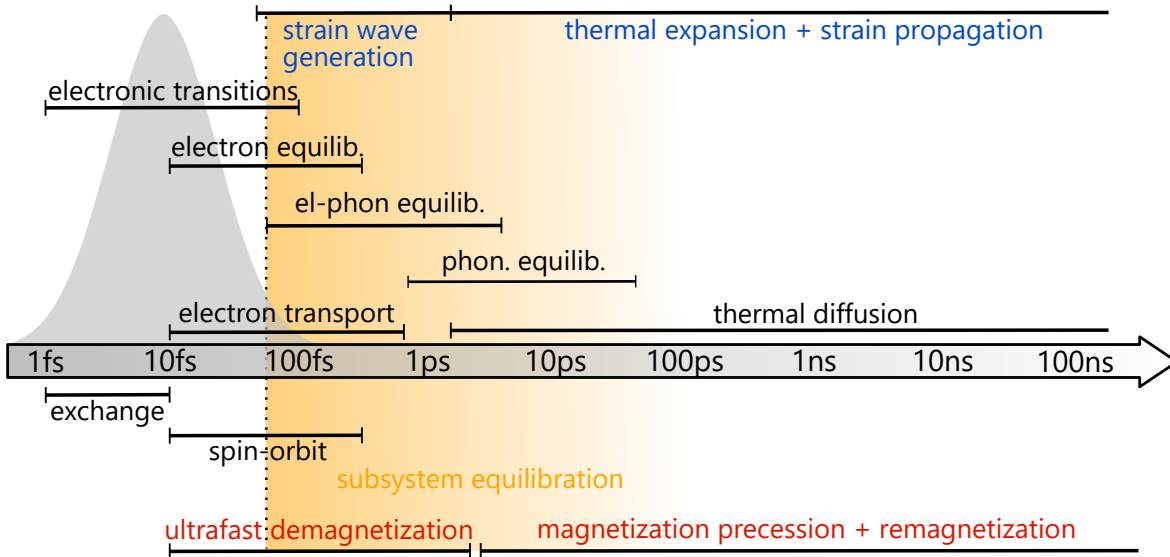
Figure 2.1.1: Laser-induced dynamics in a metal: Strain dynamics (blue) as well as magnetization dynamics (red) are both governed by the energy transfer processes within the material. The relevant microscopic processes in the context of this thesis, that occur in a laser-excited metal, and their corresponding timescales are shown schematically. The bars indicate typical timescales, even though they vary among different materials. The idea of this figure is taken from [43] including information from [44].

In order to understand the numerous experimental observations and the related physical processes, it is common to approximate the solid by three coupled subsystems: the electrons, phonons, and spin excitations [5, 33, 35]. The laser pump triggers multiple macroscopic, time-dependent changes of the metal properties, that are linked to several microscopic mechanisms and interactions between these subsystems occurring on different timescales [43, 44]. In the scope of this thesis, I study the time-dependent change of the average lattice spacing in out-of-plane direction, which is also referred to as the lattice constant in the following. Furthermore, I investigate magnetization dynamics, that are detected within a tr-MOKE experiment mentioned before. Several effects and their characteristic timescales are depicted in Fig. 2.1.1 to illustrate which interactions, that are somehow encoded in the measurement signals, can be observed. It is worth mentioning that the occurring timescales are highly material dependent. The sketched bars are meant to give a rough idea of the corresponding timescales for typical ferromagnetic metals that are frequently studied and relevant in the context of this thesis, such as nickel, for example.

In the following, I describe the typical series of events upon laser excitation. The absorption of the pump pulse photons, that leads to a strong imbalance among the electrons (electronic transitions), is determined by the optical properties of the metal and occurs over a characteristic depth. The excited free carriers, which dominate the dynamics of the solid in the first femtoseconds, are not confined to this optical penetration depth of the light but can diffuse deeper into the material instead (electron transport). Thus, the absorbed energy is spatially redistributed by the electrons, which may be also spin-polarized depending on the material [45–47].

The initial non-equilibrium of the electrons persists in metals typically only for a few 100 fs until the Fermi-Dirac distribution and thus a certain temperature is established (electron equilibration) [48, 49]. However, what remains is a strong imbalance between the hot electrons and the remaining

subsystems. By scattering events between the related quasiparticles, a fraction of the deposited energy is transferred to the other degrees of freedom so that a thermal equilibrium is developed (subsystem equilibration, see two- and three-temperature-models in the following sections). While the characteristic electron-phonon coupling time is only of the order of a picosecond in simple metals, such as nickel or platinum [50], it can take much longer in more complex heterostructures to establish a thermal equilibrium [14, 51]. Still, the electron-phonon coupling is a well understood mechanism in contrast to the equilibration processes with the magnetic system, which are still under debate. Nevertheless, it is commonly accepted that the interactions between electrons, phonons and spins are responsible for the temporal changes of the properties of a metal [14, 35]. An overview of existing models and approaches to describe the interplay between these three subsystems is given in the sections below (see chapter 2.2 and 2.3).

Moreover, the ultrafast energy deposition into each subsystem launches a propagating strain wave, i.e., generation of coherent acoustic phonons within the excited sample depth [52, 53]. This sound wave is related to a local change of the lattice constant, which can be observed in our UXRD experiments [14, 36]. On long timescales, that are dominated by thermal diffusion, the heat is redistributed all over the sample depth, and the time-dependent thermal profile governs the lattice expansion. Thus, the lattice strain contains insights into all involved microscopic interactions and the energy exchange processes between the electrons, phonons, and spins. However, these contributions have to be disentangled [15, 33].

The energy transfer into the magnetic subsystem can be monitored separately in the tr-MOKE experiment. At the macroscopic level, one can distinguish three different processes, that are discussed in detail below, namely ultrafast demagnetization [5, 6], that occurs typically on timescales of 50 fs to a few picoseconds, magnetization precession [8, 54], that is an analog to coherent acoustic phonon generation, and subsequently remagnetization [55]. The comparison of strain (Fig. 2.1.1, blue) and the magnetization dynamics (Fig. 2.1.1, red) reveals certain parallels, which are essentially related to the temperature dependence of these observables. Accordingly, both measurements contain almost equal information to some extend, that can be extracted by suitable models, and enable a quantitative comparison of both methods.

Since the energy density distribution and its temporal behavior is the governing force of all the mentioned dynamics, we have to take into account the three-dimensionality of the sample. However, it is common to choose the ratio between spatial pump and probe pulse width such that the pump pulse is much larger than the probe pulse. Therefore, we can assume a laterally homogeneously excited probe region, which allows for a one-dimensional approximation of the resulting dynamics. Spatial variations occur only along the out-of-plane direction (called z-direction in the following) parallel to the excitation plane. This approximation is used throughout the rest of this thesis.

2.2 Laser-induced strain dynamics

After a general summary of laser-induced effects in metals in the previous section, I continue with a more specific explanation of the strain dynamics generation and the underlying concepts and models here. Emphasis is placed on the description of metals to ensure a good understanding of the following UXRD-results and their interpretation. More detailed remarks and background information can be found elsewhere [43, 53, 56, 57].

Slow vs. fast temperature dynamics

Let's first consider the limit of slow heating in near-equilibrium. The slow energy deposition in this case allows for a one-temperature approximation, i.e., we describe the heat transport within

the solid by one temperature only, since all involved subsystems equilibrate faster than energy is deposited by slow heating. Thus, a spatial non-equilibrium of the temperature over the sample depth has to be dissolved, which occurs, for example, because of the limited penetration depth of the optical excitation light in the material. Provided that we consider an isotropic material with a material-specific heat capacity C and a constant heat conductivity κ, it is possible to apply the simple heat equation in order to model the energy transport (Eq. 2.2.1):

$$C\frac{\partial T(z,t)}{\partial t} = -\kappa \frac{\partial^2 T(z,t)}{\partial z^2} + S(z,t). \tag{2.2.1}$$

As a consequence of the heating, the material expands. The relative volume change $\Delta V/V_0$ is determined by the increase of the average lattice spacing of the crystal. Considering the excitation geometry and the resulting 1D-approximation, the relative volume change is simply proportional to a change of the lattice constant c along the z-direction so that the macroscopic strain η is defined as follows $\eta(t) = (c(t) - c_0)/c_0$, where c_0 corresponds to the lattice constant before excitation. Because of its intrinsic temperature dependence, this strain also exhibits a time dependence according to the temporal evolution of the temperature profile. In terms of small temperature changes ΔT in the slow heating process, we observe an equilibrium thermal expansion (see Eq. 2.2.2) defining the linear thermal expansion coefficient $\alpha(T)$, which is temperature-dependent itself:

$$\eta = \frac{\Delta c}{c_0} = \alpha(T) \cdot \Delta T. \tag{2.2.2}$$

It is important to note that equation 2.2.2 is only valid on very long timescales. Referring to the example given here, this means long after excitation, on a timescale of a few 100 ns, while the strain response earlier exhibits a more complex behavior, which will be discussed for the case of an ultrafast excitation below.

To give a simple example, figure 2.2.1 contrasts the numerical solutions of the one-temperature model (1TM) applied to model a 150 nm thick platinum layer on a glass substrate upon slow heating via a 1 ns laser pulse (a) and after ultrafast excitation by a 100 fs laser pulse (b). To be more precise, the depth dependence of the platinum temperature is depicted for several probing delays. Those results are compared to numerical solutions of a two-temperatures model (2TM) for the same excitation scenarios. While there is a very good agreement between both models for the slow heating case, distinct differences arise in the first few picoseconds after ultrafast energy deposition. The laser excitation by an ultrashort optical pulse represents the limit of energy absorption that is opposite to the slow heating. In this case, a large amount of energy is deposited almost instantaneously within the first few nanometers of the metal layer, generating a high non-equilibrium situation not only along the depth of the sample but also between the subsystems of the solid (see. Fig. 2.2.1b). Clearly, this requires a more detailed description of the processes involved in the energy redistribution.

As mentioned in the previous section, we consider the electrons, phonons, and spin subsystem participating in the heat transport processes in a magnetic metal - in case of a non-magnet, such as platinum, we omit the spin excitations. These subsystems represent coupled energy reservoirs, each of which is assigned its own local temperature T_n, where n indicates the respective subsystem (see Fig. 2.2.2). Initially, the electrons of the metal with energies less than $h\nu$ below the Fermi energy, where ν is the excitation light frequency, absorb the pump pulse photons and equilibrate within less than a few 100 fs to a Fermi-Dirac distribution. Therefore, the electronic temperature exceeds the phonon temperature directly after the excitation, as shown in the simulation of the platinum layer (see Fig. 2.2.1b). Following the zeroth law of thermodynamics, the metal strives for a thermal equilibrium, and on that account the initially deposited energy is redistributed over all degrees of freedom to adapt the subsystem temperatures. If we consider a non-magnetic metal, such as platinum, this equilibrium process is well described by a two-temperatures model (2TM,

see Eq. 2.2.3 and 2.2.4)

$$C_{e}(T_{e})\frac{\partial T_{e}}{\partial t} = \frac{\partial}{\partial z}\left(\kappa_{e}(T_{e},T_{ph})\frac{\partial T_{e}}{\partial z}\right) + g\left(T_{ph} - T_{e}\right) + S_{e}(z,t) \qquad (2.2.3)$$

$$C_{ph}\frac{\partial T_{ph}}{\partial t} = \frac{\partial}{\partial z}\left(\kappa_{ph}\frac{\partial T_{ph}}{\partial z}\right) + g\left(T_{e} - T_{ph}\right). \qquad (2.2.4)$$

Here C_n, κ_n, g and $S_e(z,t)$ are the subsystem-specific heat capacity, the thermal conductivity, the electron-phonon coupling constant, and a source term, which takes into account the initial energy deposition into the electronic system, respectively.

In platinum, the electron-phonon coupling time is about a picosecond. Shortly after this time, electrons and phonons are in a thermal equilibrium and exhibit the same temperature. Nevertheless, the calculated temperature profile of the 2TM deviates significantly longer from that of the 1TM (see Fig. 2.2.1b), which stresses the need of N-temperature models on ultrafast timescales.
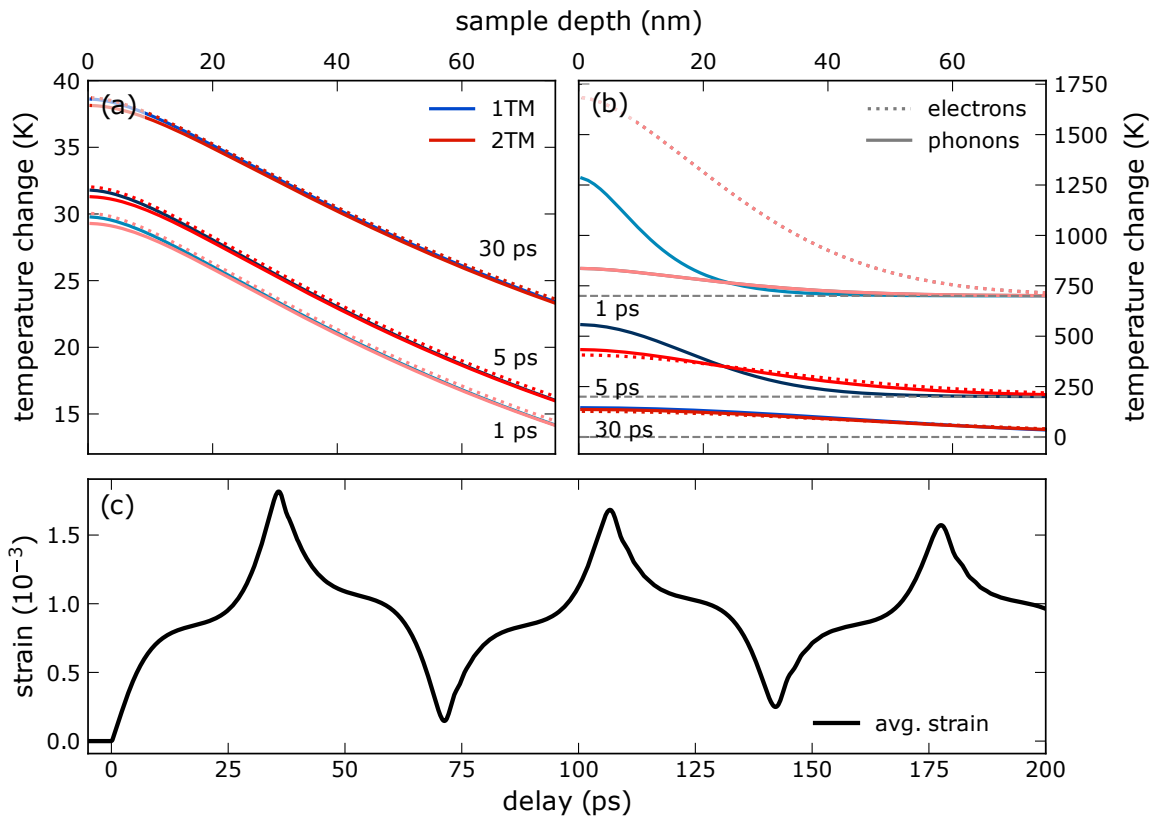
Figure 2.2.1: Slow vs. ultrafast excitation: Temperature profiles of the 150 nm Pt-sample are depicted in panel (a) for slow heating and (b) for an ultrafast excitation. While in a slow heating process all involved subsystems equilibrate faster than energy is deposited, a 1TM description (blue) of the system in the first few picoseconds is no longer sufficient upon ultrafast excitation (red). Instead a NTM (here N=2) is required accounting for the strong imbalance among the subsystem temperatures. (c) On ultrafast timescales, the lattice response is clearly different compared to a simple thermal expansion. The time-dependent average lattice strain is composed of a quasi-static contribution superimposed by propagating strain waves.

Furthermore, the lattice response, that is depicted in figure 2.2.1c, is far more complex on ultrafast timescales than the linear thermal expansion introduced before (Eq. 2.2.2). In addition to a quasi-static contribution, the ultrafast energy deposition results in a generation of coherent acoustic phonons, which propagate as wave packets through the material [37, 52]. This bipolar strain pulse, that has a leading compressive part and a following tensile component, does not affect the average strain significantly during the propagation through the sample. Only when the

sound wave reaches the interface to the substrate (at about 35 ps, see Fig. 2.2.1c) a clear change of the average lattice spacing is observed. Analogous to the reflection of light at an interface, a fraction of the strain wave gets reflected while the other is transmitted into the substrate. This is due to an impedance mismatch at the interface, which is similar to the change of the refractive index during light propagation. The acoustic impedance Z is defined as the product of sound velocity and mass density $Z = v_S \cdot \rho$ of each material. As a result of the reflection, the compression becomes an expansion, and a dominating expansion is clearly visible in the average strain for a short amount of time. However, this lasts only until the subsequent expansive component of the sound wave is reflected, which is accompanied by a sign change of the strain as well.

Similar behaviors occur at the sample surface, as can be seen in the example after the 70 ps round-trip time of the sound wave within the metal layer (see Fig. 2.2.1c). All the shown numerical calculations are done by utilization of the udkm1Dsim toolbox [58], that will be explained in more detail chapter 3.4.

Laser-induced generation of coherent strain

In order to understand the origin of the lattice dynamics after ultrafast excitation, we redefine the strain η in terms of continuum elasticity theory first (Eq. 2.2.5)

$$\eta_{ij} = \frac{1}{2} \left(\frac{\partial u_i}{\partial j} + \frac{\partial u_j}{\partial i} \right), \tag{2.2.5}$$

where the indices i, j account for the spatial coordinates x, y, z. We assume the crystalline solid as periodically ordered chains of masses, the nuclei, that are connected by springs, the electron mediated interactions between the atoms. The relative displacement u_i describes a small local shift of the atomic position relative to its rest position along a certain spatial direction i, which results in an elongation of the solid. In the scope of this thesis, we only consider elongations along the propagation direction, which is called longitudinal strain. Furthermore, since a lattice displacement is generated only along the direction perpendicular to the surface (z-direction), we can simplify the expression 2.2.5 to $\eta_{zz} = \partial u_z / \partial z$ (1D-approximation).

The generation of coherent phonons implies a conversion of optical energy, that is deposited in the material by electronic absorption, into elastic energy due to a laser-induced stress $\sigma(z,t)$. In the most general case, the relation between stress σ and strain η for small displacements is given by Hooke's law. For a laser-excited continuous thin film both variables are linked by the elastic constant c_{33}, which represents the component of the elastic tensor corresponding to the z-direction [34]:

$$\sigma_3 = c_{33}\,\eta_3. \tag{2.2.6}$$

The Voigt notation was used here for simplicity ($zz \rightarrow 3$) [57].

The inhomogeneous elastic wave equation describes the lattice dynamics induced by an external stress $\sigma(z,t)$ resulting from the absorption of the optical pulse

$$\frac{\partial^2 u_z}{\partial t^2} - v_S^2 \frac{\partial^2 u_z}{\partial z^2} = \frac{1}{\rho} \frac{\partial \sigma(z,t)}{\partial z}. \tag{2.2.7}$$

Here, ρ and $v_S = \sqrt{c_{33/\rho}}$ are the density and the sound velocity of longitudinal acoustic phonons along the z-direction, respectively.

The dominant mechanism of strain generation in metals is the thermo-elastic effect, which causes a very fast expansion of the solid as a consequence to a rapid increase of the temperature [53]. In fact, we obtain a propagating component of the time-dependent strain, that describes the coherent phonons, by solving equation 2.2.7 besides the quasi-static thermal expansion related to incoherent phonon generation during electron-phonon equilibration (see. Fig. 2.2.1c). The shape and the spectrum of the strain pulse are therefore determined by the generated stress profile

and its time-dependence. This in turn is determined by the wavelength-dependent penetration depth of the pump light, the incident fluence but also other properties of the material, such as the electron-phonon coupling. Free carrier diffusion into the depth of the material limited by the electron-phonon coupling time, as an example, can modify the energy density profile significantly. The previous considerations of lattice dynamics require at least one temperature. The phonon temperature is considered as the relevant temperature for the thermo-elastic effect in most cases. This is a good approximation in many metals due to the fast electron-phonon coupling and the small electronic linear expansion coefficient. A more general approach, that describes the stress profile generation by laser excitation, is given by the Grüneisen concept [34]. This macroscopic model links the laser-induced stresses σ_n to the energy density ρ_n^Q in the corresponding subsystem (see eq. 2.2.8). The great advantage of the Grüneisen concept is that it is a temperature-independent approach, that can be applied even before a defined subsystem-temperature is established.

$$\sigma_n = \Gamma_n \rho_n^Q. \tag{2.2.8}$$

In other words, the subsystem specific stress is directly proportional to the deposited energy density and the likewise subsystem-specific proportionality constant Γ_n, namely the Grüneisen constant, is defined as follows [34]:

$$\Gamma_n = \frac{c_{33}}{C_{Vn}(T)} \alpha_n^{\mathrm{uf}}(T) \tag{2.2.9}$$

with C_{Vn} the subsystem-specific heat capacity per constant volume and α_n^{uf} the ultrafast expansion coefficient, which may differ from the equilibrium thermal expansion coefficient introduced before [34].

As mentioned before in the context of the N-temperature model, we describe a metal depending on the magnetic properties by two or three subsystems, which exchange energy between each other. Numerous experiments, such as optical reflectivity, that accesses the electron-phonon coupling time in metals, or ultrafast demagnetization measurements, demonstrate a very rapid transfer of the energy deposited initially in the electronic system to the phonon and spin degrees of freedom. According to this, all subsystems can contribute to the strain dynamics, even though the phonons provide the major contribution because of their comparably high heat capacity. The electrons, however, affect the stress significantly only at very early times before their equilibration. The contribution of the spin system is highly material specific, but in certain cases it can also generate significant stresses related to large Grüneisen constants [33, 59]. For further details on laser-induced lattice dynamics I refer to this recent review [34].
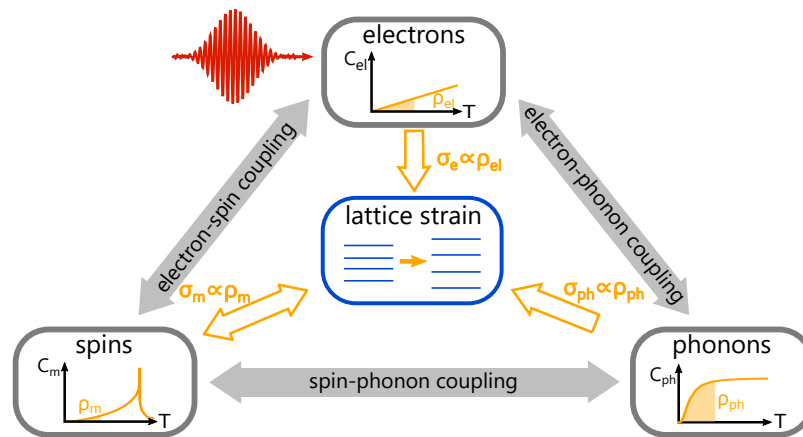
Figure 2.2.2: Origin of lattice dynamics: Optical energy absorbed by the electrons is redistributed among the coupled subsystems according to the corresponding heat capacity. As a consequence, subsystem-dependent stresses arise, that are directly proportional to the deposited energy density as stated by the Grüneisen concept. These stresses are related by Hooke's law to the lattice strain, so measurements of strain dynamics provide valuable information about energy transfer processes in a metal. Adapted from [43].

2.3 Laser-induced magnetization dynamics

Even though metals exhibiting magnetic ordering are typically separated into three coupled subsystems, the magnetic system is usually neglected regarding temperature and strain dynamics in 3d-transition metals [15, 51]. However, strong non-equilibrium dynamics can be also excited in the spin system by an ultrashort laser pulse, which is highly related to the energy transfer dynamics of the whole system [5, 17]. This section provides an overview of these macroscopic processes and the microscopic interactions induced by laser excitation. Since the field of magnetism is very broad and considerably complex, the descriptions in this section are focused on ferromagnetic materials, such as the investigated 3d-transition metal nickel.

Origin of Ferromagnetism

There are several forms of magnetism in solids, which are generally distinguished: diamagnetism, paramagnetism, ferro-, ferri-, and antiferromagnetism. The occurring magnetic properties are determined by the magnetic interactions within the material. Accordingly, dynamics of the spin system vary widely from material to material, and it is quite useful to take a closer look at the origin of magnetic properties, especially at the ferromagnetic behaviors, since these are at the center of this thesis.

Ferromagnets exhibit a characterizing spontaneous magnetization $\vec{M} = \vec{\mu}/V$, that is related to the volume density of permanent magnetic moments $\vec{\mu}$, which occur in atoms with only partially filled electronic states. This macroscopically observable property results from a parallel coupling of these magnetic moments and vanishes above a critical temperature T_C, the Curie temperature. However, unlike the ferroelectric order, this magnetic order cannot be explained by a direct interaction between magnetic dipoles. The related dipole-dipole interaction energy corresponds to temperatures of the order of $1\,\mathrm{K}$, which is in strong contradiction to observed Curie temperatures of several $100\,\mathrm{K}$. The interactions that instead lead to ferromagnetism in metals are considered in more detail in the following. The contents of this section are mainly based on the descriptions of the textbooks in Refs. [57, 60].

One of the first successful attempts to describe magnetic properties of ferromagnetic materials over a wide range of temperatures of several $100\,\mathrm{K}$ was given in the early 20th century, which is nowadays known as Weiss molecular field theory or mean field theory. On the basis of the observed spontaneous magnetization and the corresponding high Curie temperatures, Weiss postulated the existence of an intrinsic magnetic field in ferromagnets, that aligns the individual magnetic moments against thermal fluctuations (see Eq. 2.3.1). This molecular field $\vec{H}_W$ acting on an individual spin in the solid is attributed to an artificial mean field generated by the remaining spins. Accordingly, the energy assigned to this unknown interaction is given by the magneto-static energy of a magnetic moment $\vec{\mu}$ in an external field

$$E_W = -\vec{\mu} \cdot \vec{H}_W = -\beta\, \vec{\mu} \cdot \vec{M}, \tag{2.3.1}$$

where this molecular field is directly proportional to the magnetization linked by the molecular field constant β. Although this approach does not provide any microscopical insights, it still describes the principle of ferromagnetic ordering appropriately and succeeds quite well regarding the temperature dependence of the magnetization, which will be discussed below. Due to the development of the Heisenberg model proposed a few years later, which is based on the exchange interaction, this Weiss molecular field theory became also physically justified.

In fact, not only ferromagnetic materials exhibit a long-range ordering of their magnetic moments. Also most of the other forms of magnetism are defined by a specific ordering of the spins, that occurs below a critical temperature. This phenomenon is generally explained by the magnetic exchange interaction, which determines the relative orientation of neighboring magnetic moments. Because

of its origin in the electro-static Coulomb interaction, taking into account the Pauli principle, it is not, strictly speaking, a true magnetic interaction, and yet it is determining magnetism in many solids. The resulting ordering is illustrated very well within the framework of the Heisenberg model, which describes the coupling of the atomic spins $\hat{s}_i$ via

$$\hat{H}_{\text{ex}} = -\sum_{i \neq j} J_{ij} \hat{s}_i \cdot \hat{s}_j, \tag{2.3.2}$$

where we sum over all individual atoms i, and their next neighbors j considering each pair only once. Most importantly, equation 2.3.2 contains the exchange constants J_{ij}, which defines the relative orientation of the spins and the strength of the observed coupling. J_{ij} comprises the origin of the magnetic alignment and is determined by the overlap of the electronic wave functions and therefore also by the underlying potential. As can be seen from equation 2.3.2, a parallel alignment of the magnetic moments, i.e., ferromagnetic coupling, is preferred for a positive value of the exchange constant $J_{ij} > 0$. In comparison to the magnetic dipole-dipole interaction, which is of the order of 0.1 meV, the exchange coupling is clearly stronger with a strength of about 0.5 eV [44].

Although the Heisenberg model (Eq. 2.3.2) underlines the principle of the exchange interaction between spins very well, it does not explain all observations, such as the non-integer values of the magnetic moments in units of μ_{B} in 3d-ferromagnets. On this account, another model is typically consulted to explain the spontaneous magnetization in transition metals: the Stoner model for band-ferromagnets. The Stoner model is also based on an exchange interaction that couples delocalized spins of band-electrons. The origin of the finite macroscopic magnetization, however, becomes clear without having to go into the details of the universal exchange interaction.

Considering the illustrative case of a free electron gas, one determines that in such systems a parallel alignment of the spins is energetically favorable. Applying this observation to 3d-ferromagnets, that are characterized by the itinerant character of the 3d electrons, provides a good picture of the critical energy balance determining magnetic ordering. Let's consider a situation in which a small fraction of the electrons from one spin-band, e.g, of spin-↑ is placed into the band with opposite spin-orientation (spin-↓) (see Fig. 2.3.1). In doing so, the kinetic energy of the shifted electron increases by δE so that the total change of the kinetic energy of the system ΔE_{kin} is given by equation:

$$\Delta E_{\text{kin}} = \frac{1}{2} D(E_{\text{F}}) (\delta E)^2, \tag{2.3.3}$$

where $D(E_{\text{F}})$ corresponds to the electronic density of states at the Fermi level E_{F}.

This cost of kinetic energy, that makes this electron redistribution seem to be energetically unfavorable, is accompanied, however, by a reduction of the Coulomb repulsion, which is the reason for the parallel spin alignment in a free electron gas in the first place. The corresponding gain of potential energy ΔE_{pot} can be determined then within the scope of the molecular field theory (see Eq. 2.3.4) describing the impact of the electron sea on an individual magnetic moment through an artificial magnetic mean field $\vec{H}_{\text{M}} = \beta \vec{M}$, as discussed before. The magnetization in this expression arises from the difference of the spin-dependent electron densities multiplied by μ_{B}, which also explains already the mentioned non-integer character of the magnetic moments.

$$\Delta E_{\text{pot}} = -\int_0^M \beta M' \, dM' = -\frac{1}{2} \beta M^2 = -\frac{1}{2} U V [D(E_{\text{F}}) \delta E]^2 \tag{2.3.4}$$

The parameter $U = 2\mu_{\text{B}}^2 \beta / V$ in equation 2.3.4 represents the material-specific energy density that is necessary to have two electrons at the same site, i.e., the Coulomb energy. Taking into account these competing energy contributions, one can find a condition for the observed spontaneous spin-dependent band-splitting, that in turns leads to a finite magnetization. This so-called Stoner

criterion (see Eq. 2.3.5) highlights that on the one hand a high intra-atomic Coulomb-repulsion and on the other hand a high density of states at the Fermi-edge is required for a ferromagnetic ordering, leading to a high gain of potential energy and keeping the increase of kinetic energy small at the same time

$$\frac{1}{2}UD(E_\mathrm{F}) > 1. \tag{2.3.5}$$
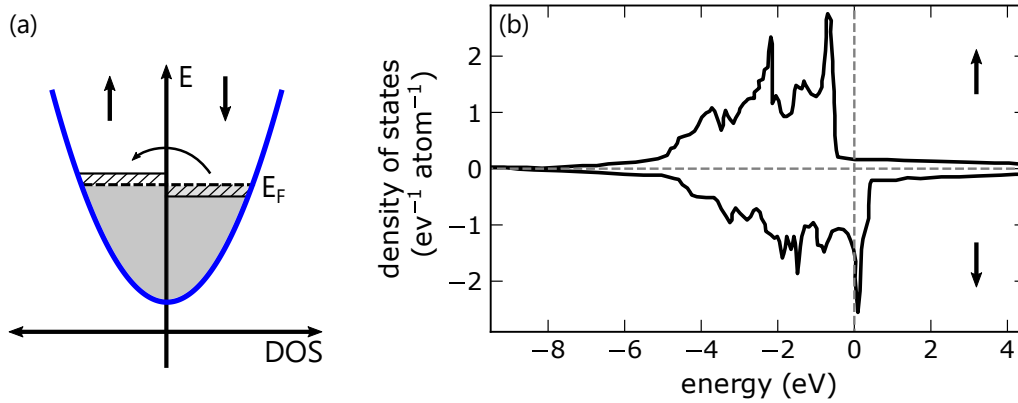
Figure 2.3.1: Magnetization of 3d-transition metals: Within the Stoner model, ferromagnetism arises from a redistribution of electrons from one spin-band into the other band with opposite spin polarization, leading to a band splitting. The final density of states in each band is governed by a subtle energy balance between an increase of kinetic energy and gain of potential energy. (Adapted from [57]) (b) The spin-dependent density of states in nickel exhibits an exchange splitting inducing a magnetic moment of $|\vec{\mu}| = 0.66\,\mu_\mathrm{B}$. The depicted data is taken from [61].

Although the Stoner model is capable of predicting the ferromagnetic 3d-transition metals and additionally provides an illustrative picture of the appearance of the non-integer values of their magnetic moments, it fails at describing the temperature dependence of the magnetization including the prediction of the phase transition temperature T_C. The Stoner-exchange energy assigned to the spin-splitting of the band structure, that is of the order of $1\,\mathrm{eV}$, would lead to Curie temperatures of several thousand Kelvin, which is much higher than observed (e.g. $T_\mathrm{C,\,Ni}$ = 631 K). So it needs a brief conclusion that contrasts the meaning of exchange in the two models introduced before: The stoner exchange is considered as the relevant energy to form local moments. It describes the energy required to flip a spin in the sea of the surrounding spins, whereas the Heisenberg-Weiss exchange determines the long range interatomic ordering and the Curie-temperature. The Heisenberg-Weiss energy describes the energy cost of flipping an individual atomic moment among the others [60].

In addition to this general alignment of the magnetic moments discussed in the previous paragraphs, measurements of the magnetization reveal a distinct preferential direction of $\vec{M}$ within the solid, which cannot be explained by the isotropic exchange interaction. This magnetic anisotropy may have several contributions that are closely related to the symmetry of the system and are therefore highly sample-dependent. It is particularly interesting in the context of magnetization precession, which is why it will be introduced in the following paragraphs and discussed in more detail in the corresponding chapter about precession.

First to be mentioned is the magneto-crystalline anisotropy originating from the spin-orbit interaction, which couples the orbital moment of the electron $\vec{L}$ to the spin $\vec{S}$. The orientation of the orbital moment is typically bound by the crystal symmetry to a certain direction within the crystal, which automatically also determines the spin direction (see Eq. 2.3.6). In a semi-classical approach, this coupling is considered as an alignment of the spin-moment by the magnetic field $\vec{H}_\mathrm{orb}$ associ-

ated with the orbital motion of the electron around the nucleus. Considering the magneto-static energy of a magnetic dipole in an external field $E = -\vec{\mu} \cdot \vec{H}_{\text{orb}}$, we find an energetically favorable orientation of the spin that is parallel to $\vec{L}$. This preferential direction is furthermore denoted as magnetic easy axis. Here, the anisotropy is defined as the energy required to force the spins rotate from the easy-axis along the hard-axis, i.e., from a parallel to a perpendicular orientation relative to the orbital angular momentum. It is mainly determined by the material-specific spin-orbit coupling constant $\xi(r)$, which depends on the orbital radius r. The spin-orbit coupling is typically smaller by a factor of 10-100 compared to the exchange interaction, which in turn results in a larger characteristic timescale (see Fig. 2.1.1).

$$\hat{H}_{\text{SO}} = \xi(\vec{r})\vec{L} \cdot \vec{S} \tag{2.3.6}$$

The other contributions to the magnetic anisotropy are also induced by a symmetry breaking within the system. For example, the shape of the investigated sample plays a crucial role due to the surfaces that break the periodicity of the crystal lattice. Stray field arising at these sample boundaries cause an unfavorable energy increase, which is then preferably minimized by the shape anisotropy. In thin films with weak magneto-crystalline anisotropy, this may be even the main contribution forcing the magnetization lying parallel to the surface plane. Moreover, elastic strain of the lattice induces an anisotropy and thus affects the equilibrium orientation of the magnetization. Finally, applying an external field $\vec{H}_{\text{ext}}$ to the ferromagnetic sample aligns its magnetization in addition to these intrinsic interactions. This is known as Zeeman energy corresponding to the energy of a magnetic dipole in an external field:

$$\hat{H}_{\text{Zee}} = \frac{\mu_{\text{B}}}{\hbar} \vec{H}_{\text{ext}} \cdot (\vec{L} + 2\vec{S}). \tag{2.3.7}$$

The Zeeman energy also affects the equilibrium orientation of the magnetization and forces $\vec{M}$ to align parallel with respect to the external field direction, provided that the field is strong enough to overcome the anisotropy energies.
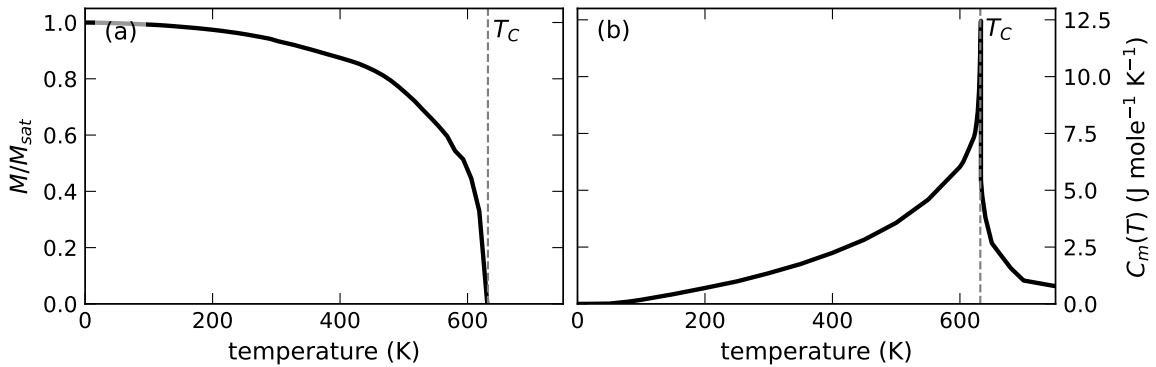
Figure 2.3.2: Static temperature-dependences in ferromagnets: (a) The normalized magnetization of nickel decreases with increasing temperature until it vanishes completely when T exceeds the Curie temperature. This decrease can be associated with an increase of energy in the magnetic system, that is determined by the temperature-dependent magnetic heat capacity depicted in panel (b). ($M(T)$ data taken from Ref. [62], $C_{\text{m}}(T)$ data taken from [63])

Ultrafast Demagnetization

The response of the magnetic system exhibits significant differences upon slow and ultrafast excitation similar to the temperature and strain dynamics. Before discussing the magnetization

dynamics after absorption of an ultrashort optical pulse by the electrons, the temperature dependence of the magnetization in the quasi-static case is considered. At finite temperatures, thermal excitations has to be considered to act against the exchange interaction that establishes the ferromagnetic ordering. Just like the theoretical model of magnetism in general, the description of the temperature-dependence of the magnetization over the whole ferromagnetic range is complicated. The mentioned Heisenberg-Weiss model predicts static magnetization comparably well, although deviations occur at very small temperatures and close to T_C. Measurements offer a great possibility to access $M(T)$ quantitatively, which is shown exemplary for nickel in figure 2.3.2a. In contrast to quasi-static thermal expansion, magnetization exhibits a highly non-linear behavior, especially when T approaches the phase transition temperature. When overcoming T_C, the material switches from a ferromagnetic to a paramagnetic phase, in which the magnetic moments are no longer macroscopically ordered. It is certainly possible to align the statistically fluctuating moments in the paramagnetic phase by an external magnetic field, the saturation fields, however, are usually huge. The material reestablishes its ferromagnetic ordering upon cooling.

In 1996, Beaurepaire et al. demonstrated for the first time that such a loss of magnetic order can also be observed on ultrafast timescales [5]. The surprisingly fast demagnetization time in their experiment of less than 1 ps has raised the question on the mechanism responsible for such a rapid change of the angular momentum, which is still under debate today. Confirmed by numerous studies, a lot of experimental and theoretical efforts have been made to explain this surprising result. In a first attempt, Beaurepaire et al. proposed a purely phenomenological extension of the known 2TM (see Chap. 2.2) to model their observations by assigning an additional temperature to the spin system that is coupled to the electrons and phonons. The temporal evolution of the magnetization is then determined by the time-dependent spin system temperature via the static magnetization. Even though this model, that is based on pure energy exchange, allows for a qualitative description of the spin dynamics, it remains unsatisfactory, since it does not involve any physical explanation of the observed phenomenon.

An answer to this issue has been proposed by Koopmans et al. some years later, including a mechanism in compliance with the conservation of angular momentum, which they referred to as microscopic three-temperatures model (m3TM) [64]. It describes the interaction between electrons and phonons in the framework of a 2TM. In addition, it includes a direct coupling of these two subsystems to the magnetization $m = M/M_S$ rather than to a spin temperature, which is mathematically expressed by three coupled differential equations:

$$C_{el}(T_{el})\frac{dT_{el}}{dt} = \nabla_z(\kappa \nabla_z T_{el}) + g(T_{ph} - T_{el}) \tag{2.3.8}$$

$$C_{ph}\frac{dT_{ph}}{dt} = g(T_{el} - T_{ph}) \tag{2.3.9}$$

$$\frac{dm}{dt} = Rm\frac{T_{ph}}{T_C}\left(1 - m\coth\left(\frac{mT_C}{T_{el}}\right)\right). \tag{2.3.10}$$

The 2TM in the m3TM describing the temperature evolution of the electrons and the phonons is given here in the form proposed by Koopmans et al. (see Eq. 2.3.8, 2.3.9). It is possible of course to adjust these equations individually in order to have an optimum description of the temporal dependence of both temperatures. In fact, this is a crucial step within the modeling, since T_{el} and T_{ph} are governing the resulting magnetization dynamics (see Eq. 2.3.10). Moreover, the parameter R in equation 2.3.10 is a material-specific quantity that contains the proposed demagnetization mechanism, the Elliott-Yafet spin-flip scattering. This scaling factor determining the demagnetization rate is defined as follows

$$R = \frac{4\alpha_{sf}g k_B T_C{}^2 V_{at}}{(\mu_{at}/\mu_B)E_D{}^2}. \tag{2.3.11}$$

In addition to the electron-phonon coupling constant g, other material parameters are collected in R, such as the atomic volume V_{at}, the magnetic moment per atom μ_{at}, the Curie temperature T_C, and the Debye-energy E_D.

The coupling of the spin-system to the remaining subsystems, that is of central interest within this model, is schematically depicted in figure 2.3.3b. Energy exchange, that is indicated by the two-sided arrows, is only considered between electrons and phonons and optionally between electrons and spins. However, an additional channel for angular momentum exchange between spin and phonon degrees of freedom is introduced (dashed line). Given by a certain probability α_{sf}, which is also included in the parameter R, an electron flips its spin in a electron-phonon scattering event. The difference in angular momentum of magnitude $\hbar$ is transferred to the emitted phonon so that the total angular momentum is conserved (see Fig. 2.3.3a). For further explanations of the model, e.g., the derivation of the spin-flip scattering probabilities, I refer to the corresponding publication in reference [64].
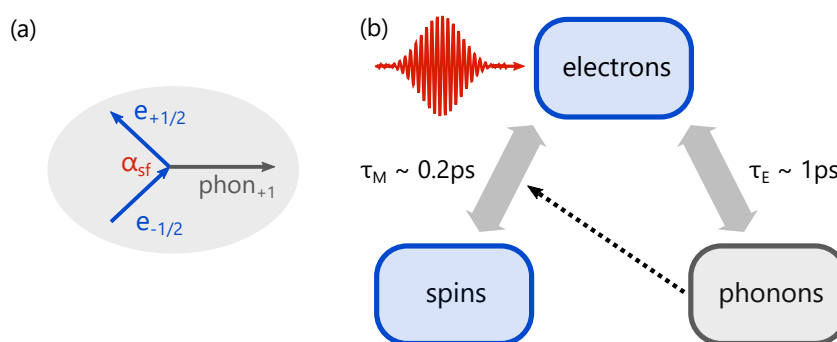
Figure 2.3.3: The m3TM for ultrafast demagnetization: (a) The model is based on the Elliott-Yafet spin flip mechanism, which describes a electron-phonon scattering event accompanied by a spin-flip resulting in a macroscopic loss of magnetic order. The difference in angular momentum is transferred to the emitted phonon so that the total angular momentum is conserved. (b) The m3TM considers three coupled reservoirs for energy and angular momentum. In contrast to the phenomenological 3TM, the spin-phonon interaction contains only a channel for angular momentum exchange (dashed line). (Figures adapted from [64]).

Apart from Elliott-Yafet spin-flip scattering, another effect that can contribute to a decrease of magnetization in measurements is superdiffusive spin transport [65, 66]. It is considered to play a substantial role especially in multilayered samples containing various magnetic films [46, 67]. The model proposed by Battiato et al. describes a local demagnetization not by a spin reversal but by a spatial redistribution of spin-polarized electrons, which leads to an increase of magnetization in other sample regions. On this account, spin-dependent lifetimes of the excited electrons are of key importance. Since the inelastic scattering probability of majority spins is smaller due to less unoccupied states, their mean free path is usually larger compared to that of minority electrons [48]. Thus, the excited electrons carrying the majority spin can be transported further away from the region of absorption, while the minority spin is virtually trapped.

Since both models, i.e., m3TM and superdiffusive spin transport, are associated with very different processes, it should not be very complicated to combine them in the discussion of demagnetization. In practice, however, this is rarely done, although convincing experimental evidence for Elliott-Yafet spin-flip scattering [68, 69] and superdiffusive spin transport [46, 67, 70] has been provided, highlighting the importance of both effects. It is worth to mention that both models are also attributed to different timescales and thus do not contradict each other. While electrons are considered thermalized in the framework of the m3TM in order to define a temperature, superdiffusive spin transport takes place before an thermal equilibrium of the electronic system is established.

Magnetization precession

A different field of magnetization dynamics is represented by investigations of magnetization precession predominantly in ferromagnetic materials, which is covered in this section. Only shortly after the pioneering experiment by Beaurepaire et al. [5], it was shown that an ultrafast excitation of a ferromagnetic layer may also induce a precessional motion of the magnetization [8, 54], that occurs on much longer timescales (see Fig. 2.1.1). This phenomenon is governed by the effective field of the magnetic material, an intrinsic magnetic field that determines the equilibrium orientation of the magnetization. A fast transient change of its direction results in a precessional motion of the magnetic moments. There are various mechanisms that may affect the effective field of the ferromagnet. Provided that the absolute value of the magnetization vector does not change upon excitation and assuming a single domain system, in which all spins are aligned parallel, it is common to describe the magnetization precession using the Landau-Lifshitz-Gilbert (LLG) equation (see Eq. 2.3.12). This approach links the normalized magnetization vector $\vec{m} = \vec{M}/M_{\mathrm{sat}}$ to the effective field $\vec{H}_{\mathrm{eff}}$ via:

$$\frac{d\vec{m}}{dt} = -\gamma \cdot \vec{m} \times \vec{H}_{\mathrm{eff}}(\vec{m},t) + \gamma \alpha \vec{m} \times (\vec{m} \times \vec{H}_{\mathrm{eff}}(\vec{m},t)), \qquad (2.3.12)$$

where γ is the gyromagnetic ratio and α a constant accounting for a phenomenological damping. The schematics in figure 2.3.4 illustrate the processes captured by the LLG equation, which provides a qualitative understanding of this phenomenon. In equilibrium, before excitation, the magnetization is aligned parallel to the effective field. Assuming a thin film with an in-plane easy-axis, the effective field is aligned at an angle θ between the surface normal and the surface plane by an external field $\vec{H}_{\mathrm{ext}}$ applied along the out-of-plane direction (see Fig. 2.3.4a). Due to an ultrafast excitation, the direction of $\vec{H}_{\mathrm{eff}}$ changes abruptly so that $\vec{H}_{\mathrm{eff}}$ and $\vec{M}$ are no longer parallel (see Fig. 2.3.4b). Consequently, a torque acts on the magnetization, which starts to precess around the new direction of the effective field. Shortly after the excitation, $\vec{H}_{\mathrm{eff}}$ relaxes to a quasi-equilibrium, but due to the initial deflection of the magnetization and the fact that the effective field and the magnetization are still not parallel, $\vec{M}$ precesses around this new equilibrium direction, which is described by the first term of Eq. 2.3.12 (see Fig. 2.3.4c). The second term of the LLG equation describes a phenomenological damping of the precession amplitude resulting in a situation where the magnetization is aligned again with the effective field. This damping accounts for energy dissipation processes between magnetic excitations and other degrees of freedom, that are usually observed in experiments.
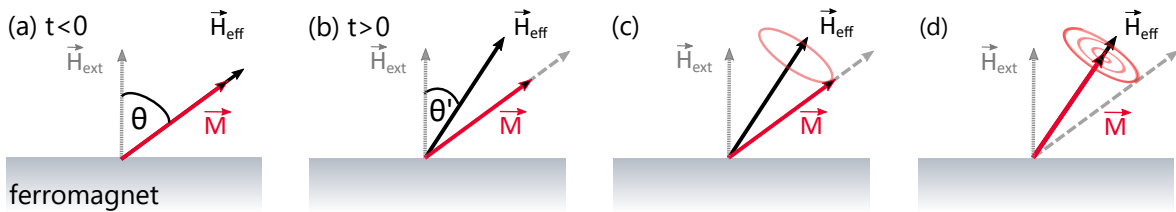
Figure 2.3.4: Origin of magnetization precession: (a) In equilibrium, the magnetization $\vec{M}$ of a thin ferromagnetic film is aligned parallel to the effective field direction. Due to the applied external field, this equilibrium orientation is canted away from the easy-axis (assumed to be in-plane) to an angle θ. (b) An ultrashort laser pulse modifies the magneto-crystalline anisotropy field. Thus, the effective field is tilted from its initial orientation, and $\vec{H}_{\mathrm{eff}}$ and $\vec{M}$ are no longer parallel. (c) As a result, the magnetization starts to precess around the new effective field direction. (d) Due to energy dissipation, this precessional motion is damped towards the new equilibrium.

The effective field is determined by the gradient of the normalized free energy density $F(\vec{m},t)$ of the corresponding ferromagnetic material $\mu_0 \vec{H}_{\mathrm{eff}}(\vec{m},t) = -\nabla_{\vec{m}} F_{\mathrm{M}}(\vec{m},t)$. This free energy comprises several energy contributions resulting from the sample-dependent magnetic interactions,

as discussed in the first subsection of this section. The Zeeman energy related to the external field $\vec{H}_{\text{ext}}$, the demagnetization energy, and anisotropy contributions, that are determined by the crystal symmetry resulting from the spin-orbit coupling, can be added. To discuss possible excitation mechanisms separately, let's consider a thin ferromagnetic film with several typical contributions to the effective field in the following. The free energy of this system is given by

$$F_{\text{M}}(\vec{m},t) = -(\vec{m} \cdot \mu_0 \vec{H}_{\text{ext}}) + \frac{\mu_0 M_{\text{sat}}}{2} m_z^2$$
$$+ \frac{K_{\text{c}}}{M_{\text{sat}}} [m_x^2 m_y^2 + m_y^2 m_z^2 + m_x^2 m_z^2] \qquad (2.3.13)$$
$$+ \frac{b\eta}{M_{\text{sat}}} m_z^2.$$

The first two terms of equation 2.3.13 account for the already mentioned Zeeman energy as well as the shape anisotropy, which forces the magnetization of thin films to be preferentially in-plane. Furthermore, equation 2.3.13 considers a cubic anisotropy determined by a temperature dependent anisotropy constant $K_{\text{c}}(T)$ and a magneto-elastic coupling term, that links the magnetization to the lattice strain η via inverse magnetostriction. Considering an unstrained sample, the latter term plays a role only after laser excitation when $\eta \neq 0$ in the magnetic layer. For simplicity, only longitudinal strain is taken into account here.

With respect to the following considerations, it is useful to rewrite equation 2.3.13 in terms of spherical coordinates. Moreover, the external field is chosen such that it lies in the xz-plane and one may write $\vec{H}_{\text{ext}} = (H_x, H_y, H_z) = (H_0 \sin \phi_{\text{ext}}, 0, H_0 \cos \phi_{\text{ext}})$, where ϕ_{ext} is the angle with respect to the surface normal. The free energy is then given by

$$F_{\text{M}}(\theta, \phi) = -H_x \cdot \sin \theta \cos \phi - H_z \cdot \cos \theta + \frac{\mu_0 M_{\text{sat}}}{2} \cos^2 \theta$$
$$+ \frac{K_{\text{c}}}{M_{\text{sat}}} [\sin^4 \theta \sin^2 \phi \cos^2 \phi + \sin^2 \theta \cos^2 \theta] \qquad (2.3.14)$$
$$+ \frac{b\eta}{M_{\text{sat}}} \cdot \cos^2 \theta.$$

Using this form (Eq. 2.3.14), it is possible to calculate the precession frequency corresponding to the ferromagnetic resonance (FMR), that is given by the following standard expression [71, 72]

$$\omega_0 = \frac{\gamma}{\sin \theta_0} \sqrt{\frac{\partial^2 F}{\partial \theta^2} \frac{\partial^2 F}{\partial \phi^2} - \left(\frac{\partial^2 F}{\partial \theta \partial \phi} \right)^2}, \qquad (2.3.15)$$

where the partial derivatives are evaluated at the equilibrium orientation (θ_0, ϕ_0) of the effective field. These equilibrium angles can be determined from the energy minimum of the free energy: $0 = \partial F / \partial \theta$ and $0 = \partial F / \partial \phi$, which is related to the effective field direction and therefore of $\vec{M}$ before excitation.

There are several possible effects that can induce a change of $\vec{H}_{\text{eff}}$. One can distinguish between changes of temperature-dependent anisotropy constants [24, 54], strain-induced magneto-elastic fields [10, 27, 71], and demagnetization [8, 26], each acting as a driving source of magnetization precession. However, their particular contributions depend on material properties and the excitation geometry, so a careful analysis is necessary in order to identify the predominant excitation mechanism. While precession frequencies are usually independent from the driving effect, amplitudes and phases provide information on the initial interaction. In the following, I discuss the typical effects after laser excitation that induce magnetization precession.

Since all terms of the effective field except for the Zeeman term depend on the magnitude of the magnetization, demagnetization can play an important role in the excitation of magnetization

precession. Depending on the induced temperature change and the corresponding time-dependent magnetization profile, the precession can vary noticeably. Considering only weak excitations, that change $\vec{M}$ significantly solely within the first few picoseconds, this contribution is treated as perturbation of the effective field via the demagnetization field related to the shape anisotropy. The more decisive contribution is given by demagnetization on long timescales, which causes long-lasting change of the effective field. Due to the non-linear temperature dependence of the magnetization, the demagnetization field change increases also non-linearly with increasing excitation fluence. Simultaneously, a decreasing magnetization magnitude reduces the contribution of the magneto-elastic field, that is directly proportional to the m_z-component.

The temperature dependence of the anisotropy constants K_{ani}, that are implicitly determined by the time-evolution of the phonon temperature T_{pho}, also depends directly on the magnetization in ferromagnetic metals [26, 73]:

$$K_{ani}(T_{pho}) = K_{ani}(0\,\text{K}) \left(\frac{|\vec{M}(T_{pho})|}{M_{sat}} \right)^{m_T}, \tag{2.3.16}$$

where the exponent $m_T = 10$ in iron and cobalt, and $m_T = 26$ in nickel. Equation 2.3.16 shows that the relative impact of demagnetization in terms of changes of the magneto-crystalline anisotropy compared to its direct contribution to the effective field is much higher. Even at small demagnetization amplitudes, the anisotropy constant can change significantly.

Considering the magneto-elastic mechanism for excitation of magnetization precession, two cases have to be distinguished, since lattice dynamics include quasi-static strain (incoherent phonons) [27, 74] as well as propagating strain waves (coherent phonons) [10, 30, 71, 75]. Both strain components may elongate the effective field but lead to different precession phases. While quasi-static thermal expansion cannot be disentangled easily from the other thermal mechanisms, propagating strain is particularly interesting as driving source due to its non-local character. The shape of the sound wave plays a crucial role, which is defined not only by its amplitude. As explained previously in chapter 2.2, the optically excited strain pulses are typically composed of a preceding compression followed by an tensile component. Accordingly, this bipolar shape results in a positive as well as a negative contribution to the effective field. Assuming a perfectly symmetric pulse, the absolute effect will be zero. Thus, to drive magnetization precession by short bipolar strain waves, an asymmetry is required, leading to a net contribution to the effective field. Considering such an asymmetric strain pulse, the change of $\vec{H}_{eff}$ is proportional to the integral over the strain profile with respect to the time [76]

$$\Delta H_{eff} \propto \int \eta(t)dt, \tag{2.3.17}$$

provided that the pulse duration $\tau_{sound} \ll T_{prec}$ with $T_{prec} = 2\pi/\omega_{prec}$ the precession period. Generally, it is not straightforward to investigate the excitation mechanisms separately, as they occur simultaneously as a result to optical excitation of a ferromagnetic metal. It is possible to disable individual contributions by choosing certain experimental geometries. For example, the dominant excitation mechanism for spin waves has been studied in several low-symmetry materials, such as iron or galfenol [25, 74, 77]. In these experiments, they exploited an in-plane anisotropy of their samples. By also applying the external magnetic field in-plane they suppressed a demagnetization field to prevent its contribution to the effective field change simplifying the analysis.

Sample structures and experimental details

A purposeful manipulation of the spin system in a material is of high interest from a fundamental perspective as well as for technological reasons. The magnetization of a ferromagnet can be affected by several effects, most prominently by demagnetization due to temperature increase, but also temperature-induced changes of the anisotropy constants and inverse magnetostriction play a role. Since these effects usually occur simultaneously upon direct laser excitation, it is not straightforward to estimate their respective influence. The key is a customized sample design that allows a separation of the different interactions in the magnetic material, as can be seen in the following chapters of this thesis.

In this chapter the samples with the same underlying structure of Pt-Cu-Ni are presented. The first part is focused on their expected temperature and strain characteristics and the magnetic properties of the studied nickel films. In the second part, attention is placed on the experimental techniques, which are ultrafast x-ray diffraction for strain measurements and time-resolved MOKE experiments for detecting magnetization dynamics.

3.1 Tailoring the heat and strain response

All samples* studied within the scope of this thesis are variations of a metallic heterostructure, that is built of 7 nm platinum, 95 nm copper and 20 nm nickel of [111]-orientation. The response of the samples after laser-excitation by an 800 nm pump pulse, that hits the sample from the platinum side, is measured in two different pump-probe experiments, i.e., tr-MOKE and UXRD (see Fig. 3.1.1).

The copper thickness is chosen such that a direct optical excitation of the nickel layer by the laser light can be ruled out. However, it has been shown for this and similar sample structures that a fraction of the absorbed energy is transferred into the nickel by hot electron transport in less than a picosecond [14, 17, 20]. The thickness of the platinum layer is adjusted with regard to the most effective excitation of the buried magnetic film. While the amount of absorbed energy increases with increasing film thickness, the probability of emission of an electron decreases due to their short inelastic mean free path of a few angstrom in Pt [50, 78]. At a layer thickness of 7 nm, we achieve an optimum absorption of optical energy and at the same time a maximum probability of an excited electron to leave the platinum without scattering [79].

Figure 3.1.1: Measurement geometry for UXRD and tr-MOKE with laser excitation from the Pt side with an 800 nm laser pulse.

800 nm pump

8 keV x-ray probe

400 nm MOKE probe

All investigated sample structures are depicted in figure 3.1.2 in order to illustrate the main

---

*All sample structures are sputtered by Michel Hehn at the Institut Jean Lamour (UMR CNRS 7198), Université Lorraine, Nancy, France

differences between each of them. Although the implemented variations are small, temperature and strain dynamics change significantly, which is particularly noticeable in the number and the shape of the propagating sound waves. Beginning from the left, one can see the previously mentioned Pt-Cu-Ni-structure, which is also referred to as sample 1a in the following (see fig. 3.1.2a). The metal stack is sputtered on a glass substrate with a thin tantalum layer in between, which ensures the single crystalline growth beneficial for the UXRD-experiment.

Sample 1b represents an inverted alternative, in which the original order of the metal layers is reversed. This brings the advantage that the MOKE-probing does not need to be carried out through the substrate. On the other hand, this sample cannot currently be studied by UXRD under the chosen excitation conditions due to limitations of the experimental setup. In order to prevent an oxidation of the nickel, a gold capping layer is added on top.

Considering the same initial energy deposition, it is expected that both samples (1a and 1b) exhibit a similar behavior of the magnetization as well as the same temperature and strain dynamics on short timescales. Negligible differences occur in the shape of the generated strain waves. Additionally, the direction of heat transport is reversed with respect to the metal film ordering on long timescales, since it is always oriented towards the substrate.
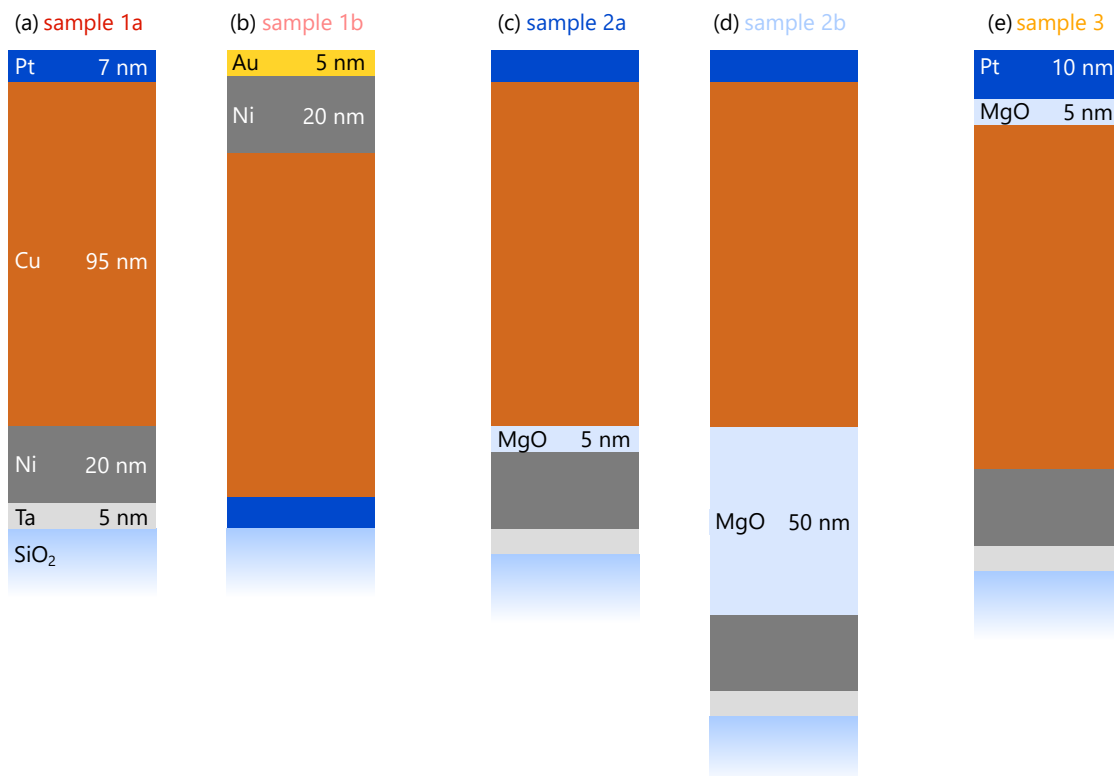
Figure 3.1.2: The temperature and strain dynamics in the ferromagnetic Ni get continuously simplified going from left to the right. Hot electrons bring energy into the Ni very rapidly in Pt-Cu-Ni and Ni-Cu-Pt (sample 1a, b). Additionally, a complex strain profile arises from the excitation of each layer. The inserted MgO-layer suppresses the hot electron transport into the adjacent films. Hence, their temperatures increases slowly and the strain dynamics do not include propagating strain from those films.

Significant changes are introduced in the remaining samples by inserting an insulating magnesium oxide (MgO) layer between the metals. In sample 2a (see fig. 3.1.2c), this MgO layer of 5 nm thickness is placed between copper and nickel. As a result, the electronic transport of energy into the magnetic film is interrupted. Accordingly, the heat propagates only slowly by phonons into the nickel and arrives later than the propagating strain, that is generated in the Pt and Cu film only. This delay is expanded in sample 2b, in which a 50 nm MgO layer is inserted (see Fig. 3.1.2d).

In sample 3, the MgO layer is grown between platinum and copper. Neglecting a small optical absorption of the copper, the entire pump energy is deposited in the platinum layer, that has a slightly larger thickness of about 10 nm in order to prevent laser excitation of the Cu film below. The temperature as well as the strain dynamics change considerably compared to that of sample 1 and 2. The heat transport is dominated by phonons through the whole sample and excitation of the platinum transducer alone generates only a short bipolar strain pulse in this sample.

The respective temperature and strain dynamics will be verified in the following chapter, where the UXRD results are presented (Chap. 3). The measurements facilitate a quantitative analysis of incoherent as well as coherent strain. Furthermore, we can calibrate the temperatures of the electron and phonon subsystem by utilizing the modular udkm1Dsim Python library [58], which provides an accurate characterization of temperature and strain in each sample.

3.2 Magnetic properties

All samples (see Fig. 3.1.2) contain a 20 nm nickel layer of [111]-orientation. The Curie temperature of bulk nickel is typically 631 K [62] and changes significantly only in monolayered samples [80, 81]. Figure 3.2.1 summarizes the measured hystereses of the nickel layers in Pt-Cu-Ni, Pt-Cu-MgO-Ni, and Pt-MgO-Cu-Ni, that are taken from different experiments. The out-of-plane hystereses (Fig. 3.2.1a, b) are detected in static polar-MOKE measurements, while the in-plane hystereses (Fig. 3.2.1c) are obtained from superconducting quantum interference device measurements (SQUID). The advantage of SQUID over MOKE is that it also accesses the saturation magnetization of the samples quantitatively, which is about $M_{sat} = 5 \cdot 10^5 \, A \, m^{-1}$ here. The difference in signal-to-noise ratio between sample 2 and the remaining samples originates from the different setups used to measure these hystereses.
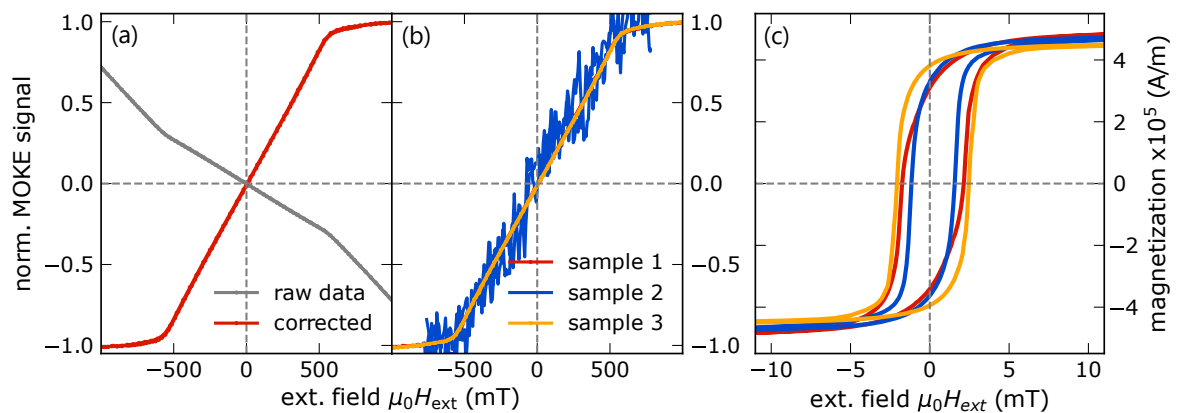

Figure 3.2.1: Ni hystereses: (a) In order to determine the out-of-plane hysteresis of the nickel film (red line) the measurement signal (grey line), that is detected in a static polar-MOKE experiment, must be corrected for the Faraday-rotation that results from probing through the paramagnetic SiO_2. (b) The out-of-plane hystereses of samples 1 to 3 show a saturation field of about 600 mT each. (c) In contrast, nickel exhibits a very small saturation field for the magnetization oriented along the easy axis, which is in-plane.

The chosen order of the metal layers within the heterostructures requires probing through the SiO_2-substrate, which is a paramagnet itself exhibiting a strong Faraday rotation. This Faraday rotation strongly contributes to the measured signal via a linear background depending on the applied external field. The signal has a kink when reaching the ferromagnetic saturation field, which is around 600 mT here. To determine the pure nickel hysteresis, it is necessary to subtract the paramagnetic background of the substrate, which is easily done by fitting the slope of the signal for fields beyond the saturation field, since it corresponds to the paramagnet only (see Fig.

3.2.1a). In time-resolved measurements, this contribution can be neglected, since it is assumed to be time-independent.

All samples exhibit almost equal hystereses measured in out-of-plane direction, which indicates the same magnetic properties. The shape of these curves clearly reveals that the out-of-plane direction coincides with the magnetic hard axis. Thus, the magnetization lies preferentially in-plane, as it is typical for thin films. The saturation field in out-of-plane direction is about 600 mT for all nickel layers, while the in-plane saturation field of approximately 2-3 mT is much smaller (see Fig.3.2.1c). Furthermore, we have looked for additional anisotropies within the sample plane of the nickel films, which is relevant for the following analysis of the magnetization precession in chapter 6. For this purpose, vibrating-sample magnetometry (VSM) measurements were performed, varying the angle of the external field from $0 - 360°$. The results, that are depicted in figure 3.2.2, show that all nickel layers exhibit no or only weak anisotropy.
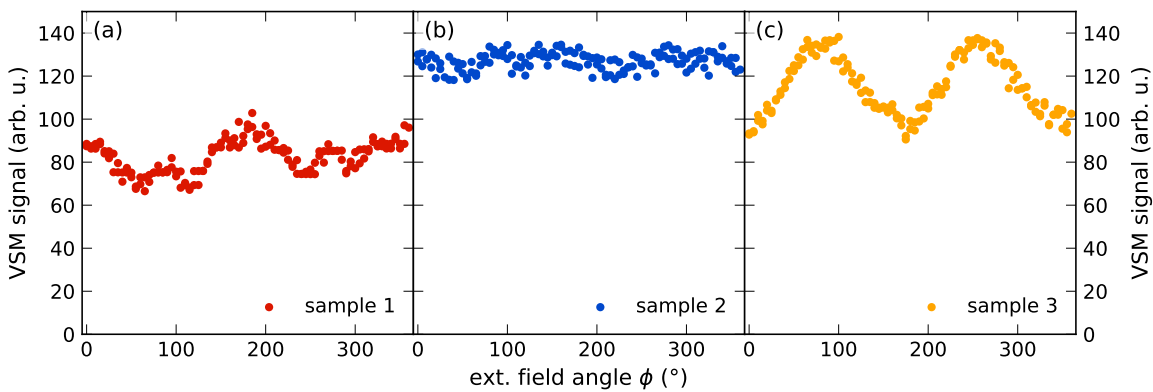
Figure 3.2.2: In-plane characterization: The in-plane anisotropy of the Pt-Cu-Ni (a), Pt-Cu-MgO-Ni (b) and Pt-MgO-Cu-Ni (c) is analyzed by VSM-measurements. All samples are almost fully isotropic, which is indicated by the rather constant VSM signal.

Both SQUID and VSM measurements were kindly performed by Juan-Carlos Rojas-Sanchez at the Institut Jean Lamour (UMR CNRS 7198), Université Lorraine, Nancy, France.

3.3 The principle of ultrafast x-ray diffraction

Ultrafast x-ray diffraction is one of many pump-probe techniques that is less frequently applied in the field of picosecond ultrasonics, although it enables the quantitative determination of the laser-induced time-dependent lattice strain in crystalline materials [34]. The measured signal contains rich information on heat transport and coherent strain dynamics, that both are related to the excited physical processes on the microscopic level. An overview of the physics behind the lattice dynamics is provided in chapter two, in this section I explain the experimental background in more detail. I start with a short introduction of the main principle of x-ray diffraction and continue then with its application to a time-resolved experiment with a time-resolution of about 100 fs.

As for other diffraction phenomena, x-ray diffraction describes the scattering process of a wave from a periodic structure. In this case, the periodicity of the lattice is imaged by scattering of an electromagnetic wave with wavelengths in the x-ray range. More specifically, sending x-rays on a crystalline sample produces a scattering pattern that is characteristic for the respective material. The analysis of the position of the intensity maxima provides information about the average lattice constant in the studied material. This relation between scattering and material lattice constant is schematically depicted in figure 3.3.1: The x-ray radiation, that is incident at a certain angle θ_{in}

relative to the sample surface with wave vector $\vec{k}_{in}$, is reflected at an angle θ_{out} with $\vec{k}_{out}$. The intensity maximum, that is also called Bragg peak, will occur if the Laue condition is satisfied (see Eq. 3.3.1)

$$\vec{k}_{out} - \vec{k}_{in} = \vec{G}, \tag{3.3.1}$$

where $\vec{G}$ is the reciprocal lattice vector representing a set of parallel lattice planes from which diffraction occurs. The absolute value of the reciprocal lattice vector is $|\vec{G}| = 2\pi/d$, where d is the average distance between the lattice planes. Furthermore, the scattering process is considered to be elastic, therefore $|\vec{k}_{in}| = |\vec{k}_{out}|$ applies. This already highlights the link between the scattering and the lattice constant.

For this explanation of x-ray diffraction here, I only consider the symmetric case, in which the scattering planes are aligned parallel relative to the surface plane implying a perpendicular lattice vector. Hence, we also measure the out-of-plane lattice constant in this geometry. Furthermore, we can rewrite the Laue-condition in terms of an equivalent formulation. The Bragg-condition (Eq. 3.3.2) underlines the relation between the Bragg-peak position and the lattice constant even more clearly:

$$n\lambda = 2c\sin\theta, \tag{3.3.2}$$

where $n = 1, 2, ...$, and λ, c, θ are the diffraction order, the wavelength of the x-ray radiation, the out-of-plane lattice constant and the incidence or scattering angle, respectively.
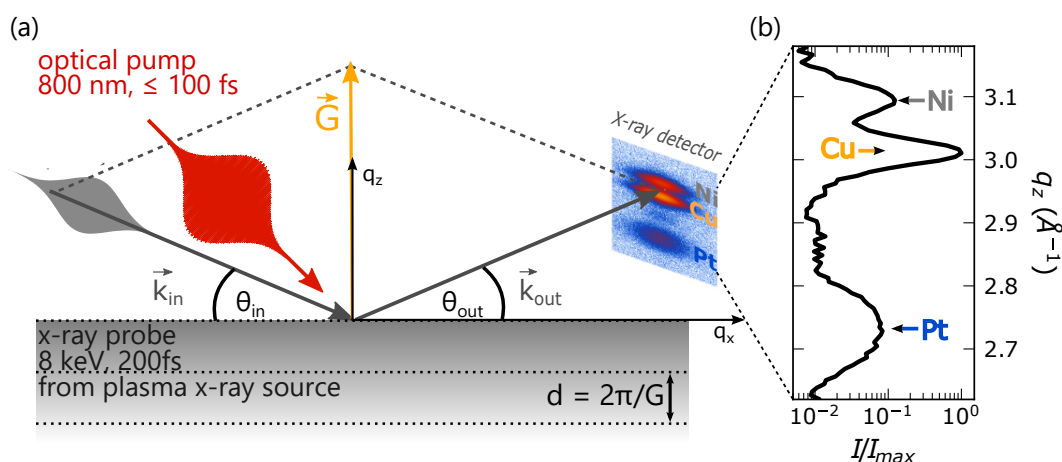

Figure 3.3.1: Principle of x-ray diffraction: (a) The incident x-ray light with wave vector $\vec{k}_{in}$ is scattered by the lattice planes. A variation of the incident angle θ_{in} provides a scan of the reciprocal space. A maximum scattering intensity occurs when the Laue condition is met, i.e., when the scattering vector $\vec{Q} = \vec{k}_{out} - \vec{k}_{in}$ coincides with a reciprocal lattice vector $\vec{G}$. Therefore, the position of a Bragg-Peak is directly related to the average lattice plane spacing. (b) Because of the large penetration depth of x-rays, it is possible to perform measurements on heterostructures combining different layers of materials, that can be analyzed separately. Each material produces an individual Bragg-peak due to the material-specific lattice constant.

A typical intensity profile is depicted in figure 3.3.1b, where the variable q_z is directly related to the scattering angle θ and therefore also to the lattice constant c. The presented scan exhibits three distinguished intensity peaks that can be assigned to different materials. These spatially separated Bragg-reflection peaks occur due to the material-specific lattice constants that define the scattering pattern. Because of this material-selectivity of x-ray diffraction, it is possible to measure the response of different layers in a heterostructure separately, which is favored additionally by the relatively high penetration depth of x-rays. A careful analysis of the peaks is necessary to disentangle the individual layer responses.

In order to conduct time-resolved measurements of the lattice expansion, the x-ray radiation can be applied as a probe in a picosecond ultrasonics experiment. The excitation in the presented experiments results from the absorption of an ultrashort optical pump pulse at a central wavelength of 800 nm by the electrons. As discussed in chapter 2.2, this ultrafast energy deposition generates subsystem-specific stresses that induce temporal changes of the lattice constant according to the spatial stress profile. The detection of the time-dependent Bragg-peak position in reciprocal space is performed by sending ultrashort x-ray pulses delayed relative to the pump pulse (see Fig. 3.3.2). The corresponding strain dynamics can be then calculated according to

$$\eta(t) = \frac{c(t) - c(t < 0)}{c(t < 0)}. \tag{3.3.3}$$
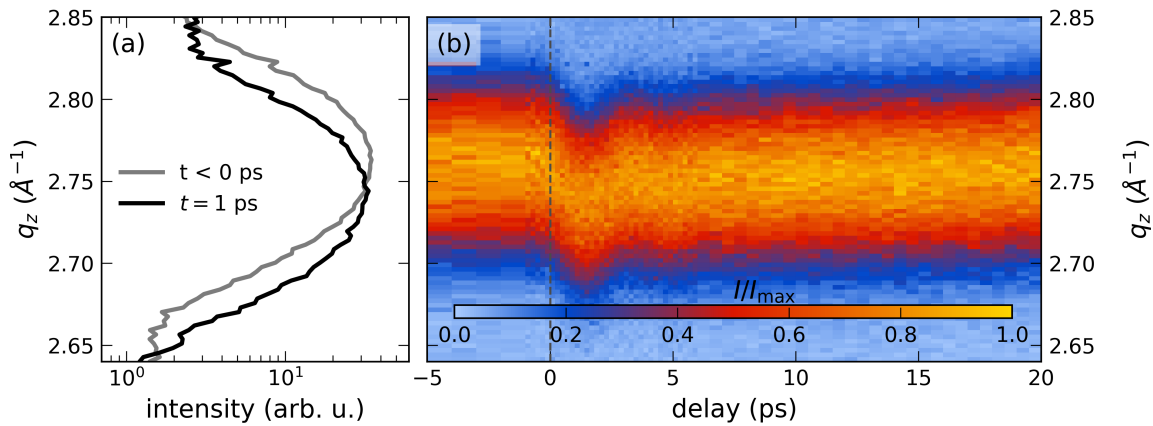
Figure 3.3.2: UXRD-measurement signal: of a 7 nm Pt film embedded within a Pt-Cu-Ni heterostructure (sample 1) excited at 800 nm. The material-specific Bragg-peak, which is depicted in panel (a), shifts in time according to the change of the average lattice spacing. (b) The time-dependent position of the Bragg-peak reveals a very fast expansion directly after the laser-excitation by shifting to smaller q_z, i.e., diffraction angles. Subsequently, the intensity maximum shifts slowly back towards its initial position according to the energy relaxation.

Clearly, the detection process in this pump-probe experiment requires ultrashort x-ray pulses in order to ensure an sub-ps time resolution. The generation of such pulses, that is submitted to several difficulties, will not be explained here, and I refer to [82, 83], for example, in which the laser-driven plasma x-ray source is introduced that is also used for the experiments presented here. Likewise further details on (time-resolved) x-ray diffraction can be found in dedicated literature [31, 34, 43, 51, 84].

3.4 Heat and strain simulation

In order to extract quantitative information from the measurements about the energy transport within the sample system, we calculate the time-dependent strain by the use of a suitable model that involves the energy redistribution between the subsystems as well as the resulting strain dynamics. Due to the strong temperature dependence of the strain, this is a good way to obtain a reliable calibration of the temperature dynamics. We use the modular Python library udkm1Dsim, which contains Python classes and routines to simulate the laser-induced temperature evolution, lattice and magnetic response along the out-of-plane direction of the modeled sample structures [58]. Since Pudell et al. discuss the simulation of the Pt-Cu-Ni heterostructure and the underlying model in detail [14], and a general description of the functionality of the udkm1Dsim is provided in the corresponding publication [58], I summarize just roughly the three steps of the simulation

and the related model assumptions applied here.

The main physical ingredients of the model have been presented already in the theory chapter on strain generation by an ultrashort laser pulse (see Chap. 2.2). In the first step of the simulation, we calculate the temperature dynamics, that in turn determine the resulting strain dynamics of the metal stack via a spatio-temporal stress. We assume a diffusive two-temperatures model (see Eq. 2.2.3 and 2.2.4) that assigns separate electron and phonon temperatures to each material layer. As mentioned before, 3d-transition metals exhibit only a small magnetic heat capacity, which is why the magnetic system is usually neglected as energy reservoir for temperature and strain dynamics [14, 51]. Furthermore, this approximation is favored by the weak magnetostriction of nickel, i.e., the negligible stress on the lattice originating from magnetic excitations.

However, before solving the set of equations of the 2TM (see Eq. 2.2.3 and 2.2.4), it is necessary to model the initial energy deposition by an 100 fs laser pulse at a central wavelength of 800 nm. By utilizing a transfer matrix approach, which treats the light propagation in a multilayered sample more carefully than the simple Lambert-Beer's law, the absorption profile is calculated.

As a result of the 2TM, we get the space- and time-resolved temperature maps of the electrons and the phonons and thus the time-dependent energy density distribution in each subsystem, that is used to calculate the resulting stress profile in the next step. This stress acts as driving force of a linear chain of masses and springs representing a discretization of the inhomogeneous elastic wave equation introduced in chapter 2.2 (see Eq. 2.2.7). Within this model, the masses correspond to a unit cell each, that are coupled to their neighbors via the springs. Thus, we obtain temperature dynamics as well as the coherent and incoherent strain response after the mentioned steps. Finally, we use the transfer matrix algorithm once more to calculate the expected time-dependence of the UXRD-signal of the individual layers in terms of dynamical x-ray diffraction theory.

By comparison of the modeling results and measured strain, we can adjust the thermophysical parameters of each material, that are used in the simulation, within a reasonable range according to literature values (see Tab. 4.1.1) to achieve a good agreement between simulation and measurement for all samples using only one set of parameters.

3.5 Principle of optical determination of the magnetization state via the magneto-optical Kerr effect

Although not taken into account often, the interaction between light and matter is also affected by the magnetic properties of a material. For that, however, it is not the direct coupling of spins and the electro-magnetic wave that is contributing to the occurring effects, since the frequencies of light in the visible part of the spectrum are too fast for the spins [85, 86]. Instead, it is the fact that because of a finite magnetization, that is oriented along a certain direction, the symmetry determined by the crystal structure is broken. This in turn induces an optical anisotropy, which is responsible for all magneto-optical effects.

Magneto-optics started with the discovery of Michael Faraday in 1846, where he observed that the polarization of linearly polarized (LP) light is rotated upon transmission through a piece of glass. The crucial point was that the glass rod was placed in a magnetic field that was oriented parallel to the propagation direction of the incident light [87]. No effect could be denoted when the field was applied perpendicularly or when it was zero. The polarization rotation increased linearly with the external field strength, which clearly confirmed the magnetic origin.

A few years after Faraday the equivalent effect upon reflection was discovered. The so-called magneto-optical Kerr effect (MOKE) describes the change of the polarization state after reflection from a magnetized material [41]. Depending on the relative orientation of the propagation direction of the incident light, the magnetization direction, and the sample surface several different MO Kerr effects are defined. Within the scope of this thesis, I will only treat the polar-MOKE geometry

applied in the following experiments (see Fig. 3.5.1 and 3.5.3). The magnetization of the material is aligned out-of-plane relative to the sample surface by an external magnetic field and lies in the plane of incidence. As for the Faraday effect, the polarization of the previously linearly polarized light is rotated by an angle θ_K relative to the initial polarization axis (see Fig. 3.5.1). This Kerr rotation as well as the additionally occurring ellipticity are directly proportional to the magnetization of the material [42], which is why this effect is excellent in order to study the macroscopic magnetic properties of ferro- and ferrimagnets.

Figure 3.5.1: MO Kerr effect in polar geometry: The polarization of the incident light gets rotated by θ_K upon reflection from a magnetized material. Additionally, the initial linear polarization becomes elliptical. The experimental geometry with a magnetization perpendicular to the sample surface lying in the plane of incidence is called polar-MOKE geometry. Polar-MOKE is mainly sensitive to the M_z-component.
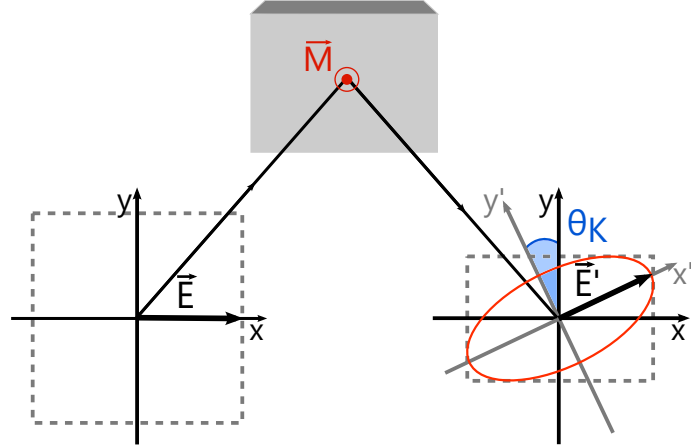
The appearance of these polarization changes, that result from the light-matter interaction, is easily understood in terms of a phenomenological picture. For simplicity, consider a plane wave, that describes a linearly polarized monochromatic light beam, propagating along the z-direction. LP light may always be described by a superposition of a left-circularly polarized und right-circularly polarized component of equal amplitudes (see. Eq. 3.5.1)

$$\vec{E}_{\pm}(\vec{r}, t) = \frac{1}{\sqrt{2}} \tilde{E} (\hat{x} \pm i\hat{y}) e^{i\vec{k}_z \cdot \vec{z} - i\omega t}, \tag{3.5.1}$$

where $\tilde{E}$, $\hat{x}$ and $\hat{y}$, k_z and ω are the amplitude, the unit vectors along the respective directions, the wave vector and the frequency of the light, respectively. Traditionally, it is common to define light of positive helicity as LCP and light of negative helicity as RCP [88].

The remaining question is, how these two components of the LP light interact with the material onto which they are shone. The dielectric tensor $\underline{\varepsilon}(k, \omega)$ determines the propagation of an electromagnetic wave in a medium, which is captured by the Fresnel equations, which typically use the refractive index n instead of $\underline{\varepsilon}(k, \omega)$. The k-dependence of the dielectric tensor is neglected in the following, which is reasonable approximation for visible wavelengths in isotropic materials. The form of $\underline{\varepsilon}(\omega)$ is essentially determined by the crystal symmetry and may be rather complicated for the most general case. Also, the breaking of symmetry, that occurs in a magnetized material, leads to an additional dependence on the magnetization and its direction. However, taking into account certain symmetry considerations, it is possible to find a manageable expression for $\underline{\varepsilon}(\omega)$, as for example for cubic crystals. Assuming a polar-MOKE geometry and a magnetization pointing along one of the crystal axes or along the [111]-direction, one can write the dielectric tensor as follows [85, 88, 89]:

$$\underline{\varepsilon} = \begin{pmatrix} \varepsilon_{xx} & \varepsilon_{xy} & 0 \\ -\varepsilon_{xy} & \varepsilon_{xx} & 0 \\ 0 & 0 & \varepsilon_{zz} \end{pmatrix}. \tag{3.5.2}$$

Here, the off-diagonal elements ε_{xy} of the dielectric tensor $\underline{\varepsilon}(\omega)$ are responsible for the magneto-optical effects and $\varepsilon_{xy} \neq 0$ applies only in materials that exhibit a finite magnetization. As a side remark, these off-diogonal elements ε_{xy} are odd functions of the magnetization M [90], which is

useful in experiments in order to eliminate non-magnetic contributions in the optical signal.
Consider an experimental setting of normal incidence, where the wave vector of the light is
aligned parallel to the magnetization and thus the z-direction $\vec{k} \| \vec{M} \| \hat{z}$, the refractive index of the
corresponding circularly polarized wave is then:

$$n^2_{\pm} = \varepsilon_{xx} \pm i\varepsilon_{xy}. \tag{3.5.3}$$

These relations (Eq. 3.5.3) already highlight the origin of all magneto-optical effects, namely that
LCP and RCP light see each different refractive indices when interacting with a magnetic material:

$$\vec{E}_{\pm}(\vec{r}, t) = \frac{1}{\sqrt{2}} E_0 (\hat{x} \pm i\hat{y}) e^{i\omega n_{\pm} \cdot \vec{z}/c_0 - i\omega t}, \tag{3.5.4}$$

where the relation between wave vector and index of refraction $k = n(\omega)\omega/c_0$ has been exploited
with c_0 the velocity of light in vacuum. Both the amplitude and phase of each wave is affected
differently, which in sum results in an elliptical polarization of the reflected light and a rotation of
the polarization axis by an angle θ_K, respectively.
Now, choosing the geometry such that the reflected beam propagates in positive z-direction, the
reflected waves are defined by $\vec{E}'_L = \vec{E}_+$ and $\vec{E}'_R = \vec{E}_-$ and the Kerr-rotation $\theta_K = \frac{1}{2}(\alpha_L - \alpha_R)$ is
determined by the phase difference between both circularly polarized components relative to their
initial orientation [88]

$$\frac{\vec{E}'_R}{\vec{E}'_L} = \frac{|\vec{E}'_R|}{|\vec{E}'_R|} \cdot e^{i(\alpha_R - \alpha_L)}. \tag{3.5.5}$$
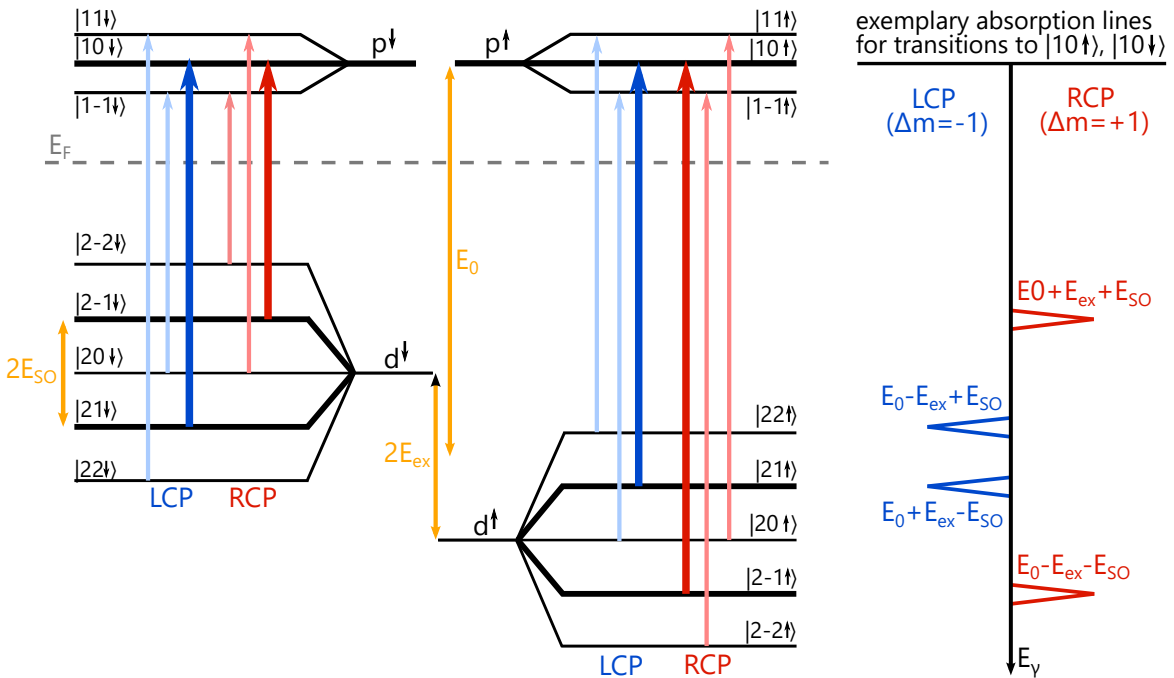
Figure 3.5.2: Helicity-dependent absorption in ferromagnetic materials: Due to the exchange
interaction and the spin-orbit coupling in ferromagnets, the energy levels change relatively to the unperturbed
state E_0. The exchange interaction separates spin up and spin down states, and the SO coupling lifts
the m-degeneracy. In terms of electronic dipole transitions, the absorption spectrum depends then on the
helicity of the light, which is illustrated for particular transitions on the right side. (Figure adapted from
[86])

Since we have now a qualitative understanding of the MO Kerr effect, we pursue the microscopic
origin of the different refractive indices for the circularly polarized waves of opposite helicity. It

must be an intrinsic property of the ferromagnet that links the magnetism to the light-matter interaction. In the range of visible wavelengths, the dielectric tensor is determined essentially by the electronic dipole transitions from a valence band to a state of higher energy. Indeed, this is where the origin of the magneto-optical effects can be found.

As an example, consider a situation of direct transitions from a d-energy level into a p-state, that is also depicted schematically in figure 3.5.2. There are two crucial ingredients for MO effects, i.e., the ferromagnetic exchange-interaction and the spin-orbit (SO) coupling, that both split the degeneracy of the energy states of the electrons. The exchange interaction causes a splitting of spin up and spin down states such that they are shifted relatively to each other by the exchange gap (compare Chap. 2.3). The SO coupling lifts the degeneracy of the magnetic quantum number m within both spin states. Due to the selection rules of electronic dipole transitions, different transitions are allowed for left-circular light ($\Delta m = -1$) and right-circular light ($\Delta m = +1$), which is mirrored directly by the absorption spectra of each helicity (see Fig. 3.5.2, right part). It should be stressed that for this helicity dependent absorption both the exchange interaction as well as the spin-orbit coupling are absolutely necessary. This is why materials that exhibit a strong SO coupling also exhibit a larger MOKE contrast.

Clearly these considerations from above present a very simplified view compared to a real solid, but this picture is, nevertheless, still applicable for materials with an electronic band structure, such as 3d transition metals, for example. Calculations of the dielectric tensor following the mentioned principle, that involves the spin dependent electronic band structure, are conducted nowadays within standard procedures as spin-density functional theory (SDFT) and provide results in good agreement with experimental observations [89]. Furthermore, for explanations and details beyond this basic introduction, I refer to dedicated literature, for example, the cited works within this chapter and the references therein [86, 88, 91].

Finally, the application of the MO Kerr effect in a time-resolved pump-probe experiment is discussed, which measures the magnetization dynamics. Nowadays, time-resolved MOKE is one of the most often applied techniques to study magnetization dynamics [5, 8]. The experimental setup used here is depicted schematically in figure 3.5.3. Measurements are performed using a Ti:Sa laser system, that provides laser pulses with a central wavelength of 800 nm and a pulse duration of about 150 fs at a repetition rate of 1 kHz. These ultrashort laser pulses are separated into a pump pulse and a much weaker probe pulse, that both are directed to the sample via numerous mirrors on individual beam paths. The temporal delay between excitation and detection is adjusted by a motorized delay stage, which is part of the pump path.

Furthermore, the pump power can be adjusted by using a $\lambda/2$-waveplate in combination with a polarizer, before the laser is focused onto the sample. The beam size of the Gaussian pump pulse is about 400 µm up to 1 mm in diameter depending on the position of the focusing lens. In order to ensure a constant overlap of the pump and the probe spot, a CCD-camera tracks the pump beam position, which can be corrected automatically by a motorized mirror.

As mentioned previously, the detection of magnetization dynamics is performed in a polar-MOKE geometry, where the probe light is directed to the side of the sample opposite to the arrival of the excitation pulse. Moreover, the frequency of the probe pulse is doubled compared to the initial 800 nm via a BBO-crystal so that it exhibits a central wavelength of 400 nm. It is focused down to a spot size of about 90×90 µm^2 onto the sample under almost normal incidence, and its reflection is then directed through a Wollaston prism onto balanced photo diodes, that measure the incoming intensity. The Wollaston prism is an optical element that separates the s- and p-polarized light components, which each hit one of the two diodes. By the use of an additional $\lambda/2$-waveplate, it is possible to adjust the polarization before the detector so that the intensity change of both polarization components and thus the polarization rotation can be detected.

The sample is mounted between two pole shoes and Helmholtz coils of an electro-magnet, that generates a magnetic field perpendicular to the sample surface. Thus, it is possible to measure the

out-of-plane component of the magnetization (here: z-component M_z), since the projection of the magnetization onto the wave vector of the incident probe light generates the measured signal. In order to eliminate non-magnetic contributions, we perform measurements with the external field applied along both positive and negative field directions, that are then subtracted from each other. This removes contributions that are independent of the magnetic field and doubles the magnetic signal at the same time, which results in an enhanced measurement contrast.
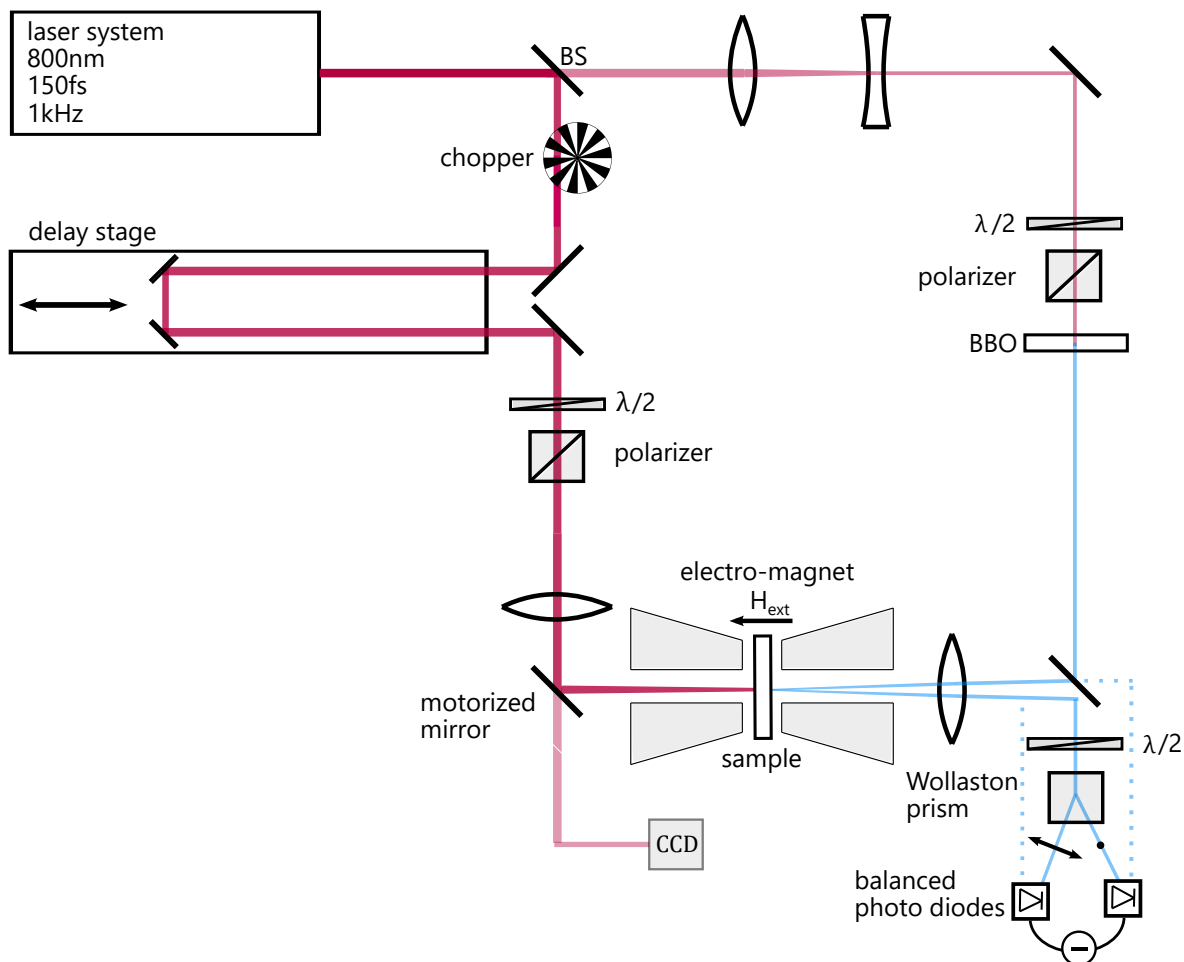
Figure 3.5.3: Experimental polar-MOKE setup: The ultrashort 800 nm-laser pulses, that are generated by a Ti:Sa laser system, are separated into a pump pulse and a much weaker probe pulse, which is frequency doubled afterwards. Both pulses hit the sample, that is placed between the pole shoes of an electro-magnet, from opposite sides. Due to the almost normal incidence of the probing light, we are sensitive to the out-of-plane (oop) component of the magnetization (here M_z). An external magnetic field up to 1 T, that is provided by the electro-magnet, can be applied along the oop direction, hence, align the in-plane magnetization typical for thin films along $\hat{z}$. By small changes of the probe beam path, the setup can be used to measure simple optical reflectivity as well (dotted line).

It is also possible to measure the time-resolved reflectivity with this setup by applying only small changes in the detection beam path, that are indicated by the dotted lines in figure 3.5.3. In order to get information on temperature and strain dynamics of nickel, a back side probe geometry is used for the transient reflectivity too. Before hitting the sample, the probe pulse is separated into one pulse that gets reflected by the sample and a reference beam. The two balanced photo diodes detect the intensity of the two components each, from which the measurement signal results as the difference of both, i.e., the change of reflectivity ΔR (see dotted path in Fig. 3.5.3). This reflectivity change is determined by a temperature-dependent as well as a strain-dependent change of the refractive index.

Strain and Temperature Dynamics

Laser-induced strain dynamics on ultrafast timescales has been subject of active research for more than three decades. The experiments, that are conducted most commonly in an all-optical pump-probe scheme [37, 52], are summarized under the term picosecond ultrasonics and study the elastic properties of a material upon laser-excitation. This experimental approach is applied in a wide field of materials such as metals [38] or semiconductors [92–94]. The lattice response induced by an ultrafast excitation provides insights about physical processes such as electron-phonon coupling and excited carrier diffusion.

Ultrafast X-ray diffraction (UXRD), in addition to optical detection, represents another pump-probe technique that makes strain dynamics quantitatively accessible [36, 39]. Since UXRD is a material-selective technique, it is also possible to detect the response of individual materials within a heterostructure, which is a great advantage over all-optical measurements. By doing so, one gets a detailed picture of the energy transport within the sample. Furthermore, different propagation velocities of heat and sound allow for separate investigation of temperature- and strain dynamics by using an absorbing transducer and a detection layer [31, 33].

These advantages are used within the scope of this thesis in order to characterize the metallic samples introduced in the previous chapter. Within time-resolved x-ray diffraction experiments, that are supported by theoretical modeling, we study the temperature and strain dynamics of the sample structures. In this chapter I present the experimental data of the UXRD measurements and the simulation results. Additionally, these results are compared to all-optical measurements in order to highlight advantages and disadvantages of both detection schemes.

4.1 Characterization of strain and temperature dynamics

As mentioned before, we excite the samples from the platinum side with an 800 nm laser pulse of about 100 fs pulse duration and at a repetition rate of 1 kHz. The incident fluence is 13.2 mJ cm^{-2} for sample 1 (Pt-Cu-Ni) and 2 (Pt-Cu-MgO-Ni) but 7.5 mJ cm^{-2} for sample 3 (Pt-MgO-Cu-Ni), since the laser damage threshold is lowered here compared to the first two samples due to the MgO-barrier that keeps the heat within the transducer layer. The 200 fs x-ray probing pulses are derived from a laser-driven plasma x-ray source, and their energy equals the Cu K$_\alpha$-emission line of 8 keV. The reciprocal space map shows three distinguished Bragg-peaks, that can be assigned to the individual materials Pt, Cu and Ni, and whose time evolution is measured in the experiment (see Chap. 3.3).

This thesis can be seen as one continuation of numerous previous works that study non-equilibrium dynamics in heterostructures from a magnetism perspective [17, 18, 20, 21, 79] as well as from a lattice dynamics point of view [14, 31, 51] in order to analyze the energy transfer processes and heat transport governed by the excited electronic, phonon, and spin degrees of freedom. Here, I aim to combine both observables, i.e., magnetization change and lattice dynamics, which draws a more detailed picture and reduces the number of free modeling parameters drastically. This in turn results in a well-grounded evaluation of existing models. Due to its direct quantitative

character and the long-term expertise of our group, UXRD is a great tool for temperature and strain characterization and for extracting the spatio-temporal energy density distribution from that. In this section, I focus on the main characteristics of the samples and the differences between them regarding the temperature and strain dynamics. From a fundamental perspective, the heat transport behavior of Pt-Cu-Ni has already been discussed in detail in [14]. By means of UXRD measurements and modeling, the authors show that the energy mainly absorbed in the platinum layer is transported by the excited electrons into the nickel film within less than a picosecond. Due to the high electronic heat capacity of nickel and the weak electron-phonon coupling in copper, the energy is distributed initially to platinum and nickel. Only then the copper layer in between is heated by thermalization with the hot neighboring metals.
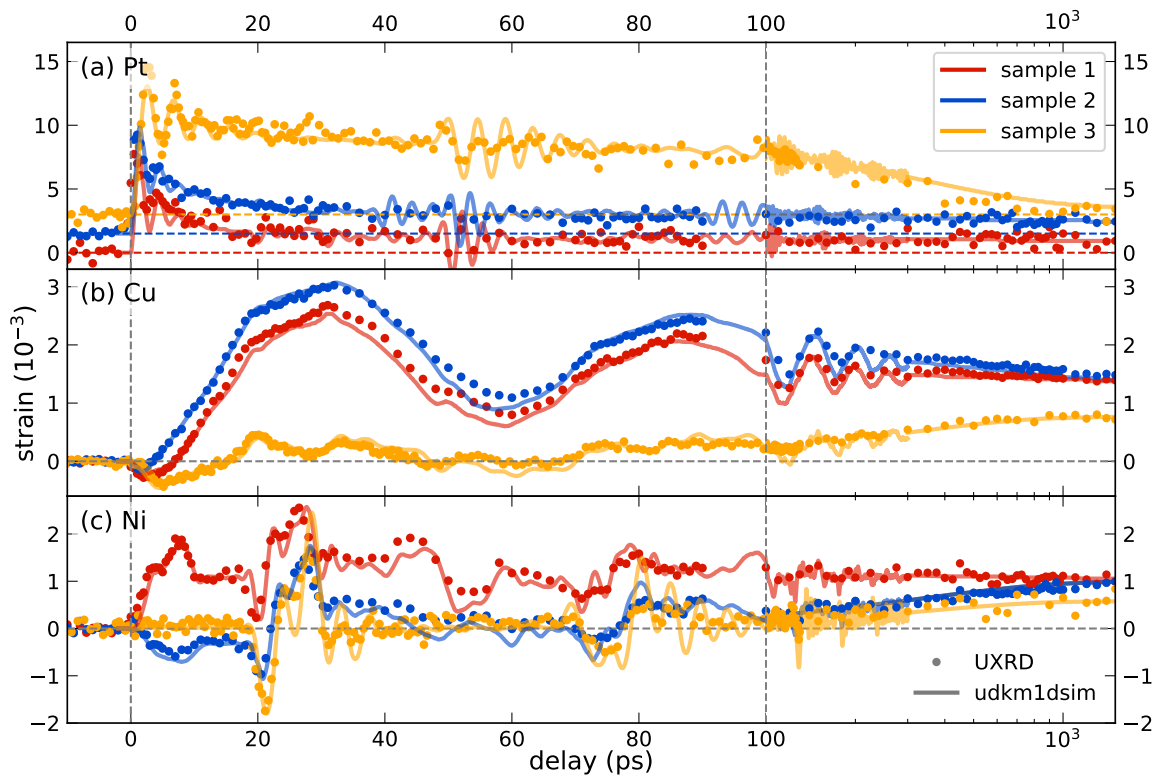
Figure 4.1.1: Average strain dynamics: The measured (symbols) and simulated (solid lines) UXRD transients are depicted for the constituent metal layers (a) Pt, (b) Cu and (c) Ni, where the Pt transients are shifted for clarity. The excitation fluence is $13.2\,\mathrm{mJ\,cm^{-2}}$ for sample 1 and 2 (red, blue) and $7.5\,\mathrm{mJ\,cm^{-2}}$ for sample 3 (orange). Although sample 3 is excited with a much lower fluence, it still exhibits similar Pt strain pulse amplitudes due to the containment of the total absorbed energy within the Pt transducer.

The UXRD data, that are depicted in figure 4.1.1, show the measured strain separately for the constituent metals platinum (a), copper (b) and nickel (c) for the samples 1-3. Starting with Pt-Cu-Ni (red symbols), we observe a pronounced expansion of the platinum transducer directly after the pump pulse arrival, which is followed by thickness oscillations of about 3 ps period, that result from the partial strain pulse reflection at the Pt-Cu interface and the sample surface. The average strain level decreases rapidly after the initial expansion due to heat transport into the adjacent copper and nickel layers until a long lasting plateau is established. However, it is the nickel film not copper that exhibits a similarly rapid expansion directly after the platinum. As mentioned before, the excited electrons, that have a comparably large mean free path in copper, transfer a substantial fraction of the deposited energy into the nickel without having interacted significantly with the copper phonons. Due to the efficient electron-phonon coupling in nickel, the phonon temperature increases clearly faster, causing the rapid expansion via a rapidly rising

expansive stress. Moreover, the Pt strain pulse and its echos arrive in the nickel film at about 25 ps followed by more signatures of propagating strain with decreasing amplitude in 25 ps intervals. These intervals correspond to a half round-trip time of a sound wave within the metallic part of the sample and result from two strain waves generated at the front and at the end of the metal stack that arrive alternating in the nickel film.

At the same time, as a result of the expansion of platinum and nickel, the copper layer is compressed in the first few picoseconds until after 7 ps the thermal expansion starts to prevail. Due to acoustic reflections at the sample surface and the substrate interface, thickness oscillations are generated in the copper. Accordingly, this coherent strain originating from Cu can be also observed in Ni, which is, however, superimposed by the other strain signatures and difficult to recognize. In the second sample (Pt-Cu-MgO-Ni) following next, this long strain pulse is much easier to identify.

The blue symbols in figure 4.1.1 describe the strain dynamics of Pt-Cu-MgO-Ni (sample 2a), that shows a behavior of the platinum and copper layer that is very similar to the corresponding films of the first sample without MgO due to the same optical absorption. Again, we observe a very rapid expansion in Pt and subsequent thickness oscillations as well as a cooling to the adjacent metals. In contrast to the previous sample, the MgO-barrier suppresses the fast energy transport by the electrons into the nickel layer and thus prevents the Ni-expansion observed in the pure metal stack Pt-Cu-Ni. As a consequence, the initial compression of the copper is less pronounced. More importantly, a compression of the nickel induced by the thermal expansion in copper occurs starting at the Cu-Ni interface, which corresponds to the previously mentioned long bipolar strain pulse originating from Cu.

A strong modulation of the nickel strain around 25 ps again indicates the arrival of the Pt strain pulse, which coincides additionally with the expansive component of the bipolar sound wave originating from copper. Because of the long period resulting from the large Cu-thickness, the Ni-strain has a step-like shape with long lasting plateaus superimposed by the short bipolar modulation originating from platinum. Owing to the missing Ni strain pulse, the strain modulations in nickel occur every 50 ps, which is the round-trip time of the sound waves. Further, the slowly increasing background indicates a slow temperature increase, that is governed by phonon heat transport. As a final remark, the agreement of the strain levels on the nanosecond timescale dominated by heat transport to the substrate in all metal layers confirms the same initial energy absorption in both samples.

The situation changes even further in sample 3 (Pt-MgO-Cu-Ni, yellow symbols). In this case, the energy, which we assume to be deposited only in platinum, is confined in the transducer, since the electronic channel to the following layers is interrupted by the insulating MgO. Similar to the previous observations, platinum expands very rapidly immediately after the excitation and displays subsequently thickness oscillations with slightly longer periods due to the increased film thickness. The effect of the MgO-layer is clearly visible in the comparably slow decrease of the average strain level. Due to the slow heat transport by phonons, the energy stays longer in the Pt transducer, which results in a large energy density in the phonon system related to a larger lattice constant. Furthermore, the lattice dynamics of copper are determined by the strain propagation of the Pt sound wave, which leads on average to a weak modulation until the slow thermal expansion dominates from about 100 ps on. Besides, a similar situation is given in nickel. Just as in copper, we observe a slow expansion on long timescales resulting from thermal diffusion through the preceding layers. Again, changes of the strain signal occur because of strain wave propagation. We can identify a sharp but asymmetric bipolar strain pulse of high amplitude returning every 50 ps in the Ni detection layer.
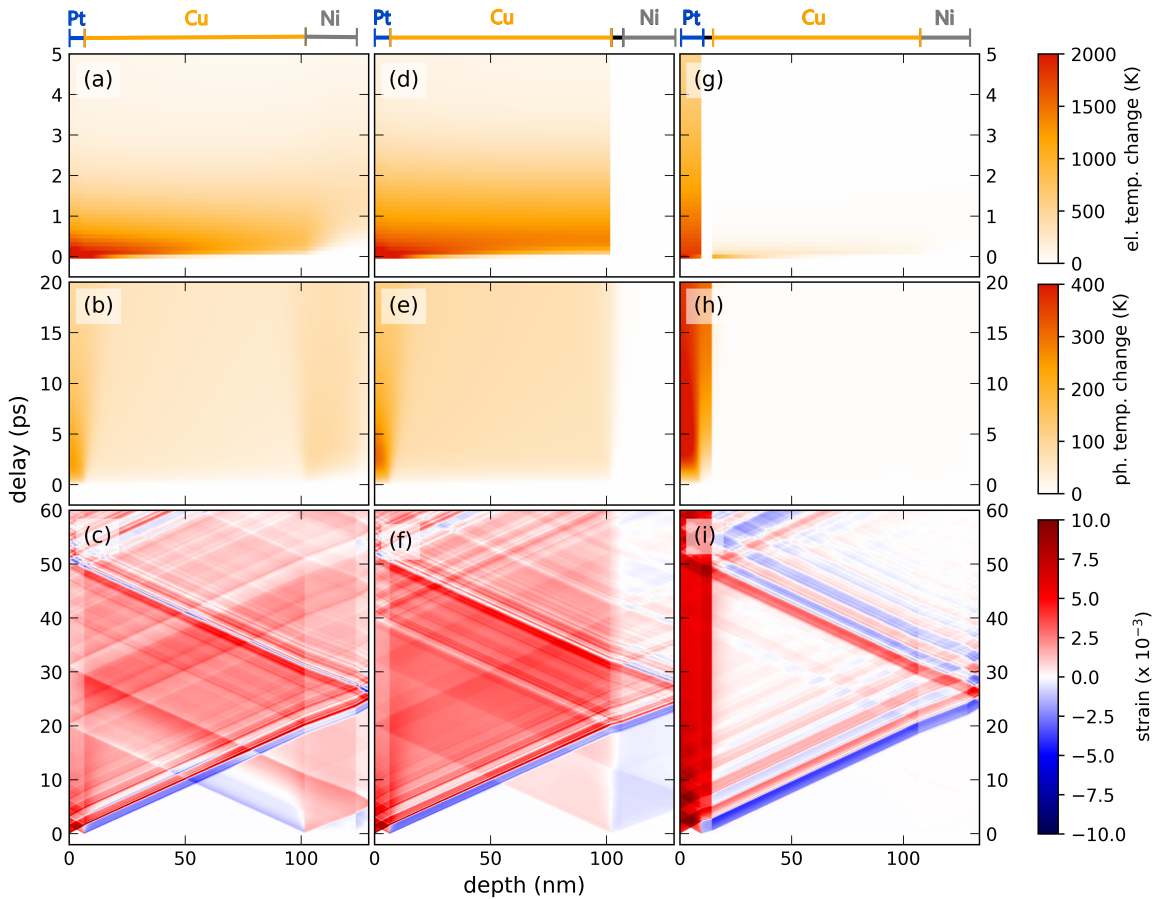
Figure 4.1.2: Simulated spatio-temporal strain and temperature maps: Depicted are the modeled laser-induced dynamics of sample 1 ((a)-(c)), sample 2 ((d)-(f)), and sample 3 ((g)-(i)), where the top, the middle, and the bottom panels display the electronic temperatures, phonon temperatures, and the strain, respectively. It has been shown before that electrons redistribute the absorbed energy very rapidly over the full sample depth in such heterostructures as presented here. As a result, a complex strain profile arises from the excitation of each layer. The initial energy distribution is modified by inserting an insulating MgO film, that suppresses the hot electron transport into the adjacent films and clearly changes the heat and strain response of Ni in particular.

All these observations described above, that can be easily explained taking into account the previous results as well, match very well the expectations regarding the chosen sample designs. This is confirmed not only by the UXRD measurements but also by the simulated UXRD-transients, that are depicted as solid lines in figure 4.1.1 and the spatio-temporal strain and temperature maps in figure 4.1.2. Each column in figure 4.1.2 shows from the top to the bottom the electronic temperatures (a,d,g), the phonon temperatures (b, e, h), and the resulting strain dynamics (c, f, i) of sample 1 (left column) to 3 (right column). In terms of a diffusive two-temperature model, the fast expansion of the nickel layer in Pt-Cu-Ni can be explained, since hot electrons cross the copper layer in less than a picosecond. Significant electron temperature changes arise across the entire sample depth almost instantaneously and map a temperature gradient as commonly expected (compare Fig. 4.1.2a). In contrast, the direction of the heat transport in the phonon subsystem is reversed, since the nickel film is heated before copper (see Fig. 4.1.2b).

This behavior is modified by inserting an insulating MgO layer, that suppresses the electronic transport into the following metal layers (see Fig. 4.1.2d, g). As a result, the temperature increase in these films is slowed down substantially (see Fig. 4.1.2e, h), which in turn leads to a very different strain response. Sound waves are generated only at stress gradients (compare Fig. 4.1.2c, f, i) and exhibit a period of $T = 2 d_i / v_{\mathrm{sound}\,i}$ where d_i is the corresponding film thickness. The

presented UXRD results highlight the great possibilities of tailoring strain responses by suitable combinations of metals with different properties. From the efficient heat conductivity of Cu in combination with the Ni, that draws the energy, pulse shapes can be adjusted independently from the light penetration depth. Apart from that, each generated sound wave is mainly reflected at the sample surface and the metal-glass interface and propagates with a round-trip time corresponding to the thickness of the whole metal stack through the sample.

| parameter	Pt	Cu	Ni	Ta	MgO	glass
γ^S (mJ cm^{-3} K^{-2})	0.74 [95]	0.10 [95]	1.06 [95]	0.38 (0.48) [96]	-	-
C_{ph} (J cm^{-3} K^{-1})	2.85 [97]	3.44 [98]	3.94 [40]	2.33 [96]	3.14 [99]	1.80 [100]
κ_e^0 (W m^{-1} K^{-1})	66.0 (63.7) [101]	496.0 [95]	81.4 [102]	52.0 [103]	-	-
κ_{ph} (W m^{-1} K^{-1})	5.0 (6.7) [101]	5.0	9.6 (15.0) [102]	5.0	2.5 (60) [104]	1.0 [100]
g (PW m^{-3} K^{-1})	375.0 [50]	94.5 [50]	360.0 [50]	100	-	-
ρ (g cm^{-3})	21.45	8.96	8.91	16.68	3.58	2.54 [100]
v_S (nm ps^{-1})	4.2 (4.3) [105]	5.2 [106]	6.3 [107]	4.2 [108]	9.1 [109]	5.7 [100]
α_{el} (10^{-9} K^{-2}) [110]	0.84 (2.2)	0.32	2.70 (3.9)	0.83 (1.1)	-	-
α_{ph} (10^{-5} K^{-1})	0.78 (1.03)	1.40 [110]	1.08 (1.23)	0.56 (0.65)	1.04 [111]	0.37 [100]
Poisson-factor	2.20	1.72	1.60	2.03	2.00	-
Γ_e	0.9 (2.4)	1.3 (1.2)	1.4 (2.1)	1.3 (1.7)	-	-
Γ_{ph}	2.3 (3.0)	1.7	1.6	1.4 (1.7)	1.0	0.03 [100]

Table 4.1.1: Simulation parameters: The thermophysical parameters of all constituent materials in the studied heterostructures assumed in the modeling using the UDKM1DSIM toolbox. The values given in parenthesis are from literature when it disagrees with the value applied in the simulation. The electron and phonon Grüneisen constants are calculated via $\Gamma_{el/ph} = v_S^2 \rho \alpha_{el/ph}/C_{el/ph}$.

The material-specific thermophysical parameters that are used in the udkm1Dsim-simulation are summarized in table 4.1.1. The excellent agreement of UXRD simulation and measurement, that is achieved by use of only one set of parameters for all samples, supports our underlying model and justifies its assumptions. It is possible to predict reliably the lattice dynamics and therefore the temperature dynamics for all sample structures that are based on the Pt-Cu-Ni heterostructure by our model. Hence, elaborate UXRD-measurements are not absolutely necessary. We can easily compare strain and temperature dynamics of Pt-Cu-Ni to the modeling of the inverted counterpart, on which UXRD measurements cannot be conducted currently in the chosen excitation geometry due to limitations of the experimental setup.

Figure 4.1.3 presents the modeled strain response (a) and the averaged electron and phonon

temperatures (b) of sample 1b and 2b over time. As in Pt-Cu-Ni, the Ni-electron temperature as well as the strain in Ni-Cu-Pt increase rapidly directly after the excitation. Although a precise view on the exact shape of the strain dynamics reveals small differences, the main characteristics of both samples are the same, which will become important in the following.

The simulated response of sample 2b with 50 nm MgO (light blue line in Fig. 4.1.3) does not surprise either by any unexpected behavior. In fact, the thick MgO-layer simply delays the arrival of the strain pulses as well as the temperature increase in nickel. In this case, the heat gets into the nickel long after the strain pulses are damped, which causes an almost ideal separation of propagating strain and heat.
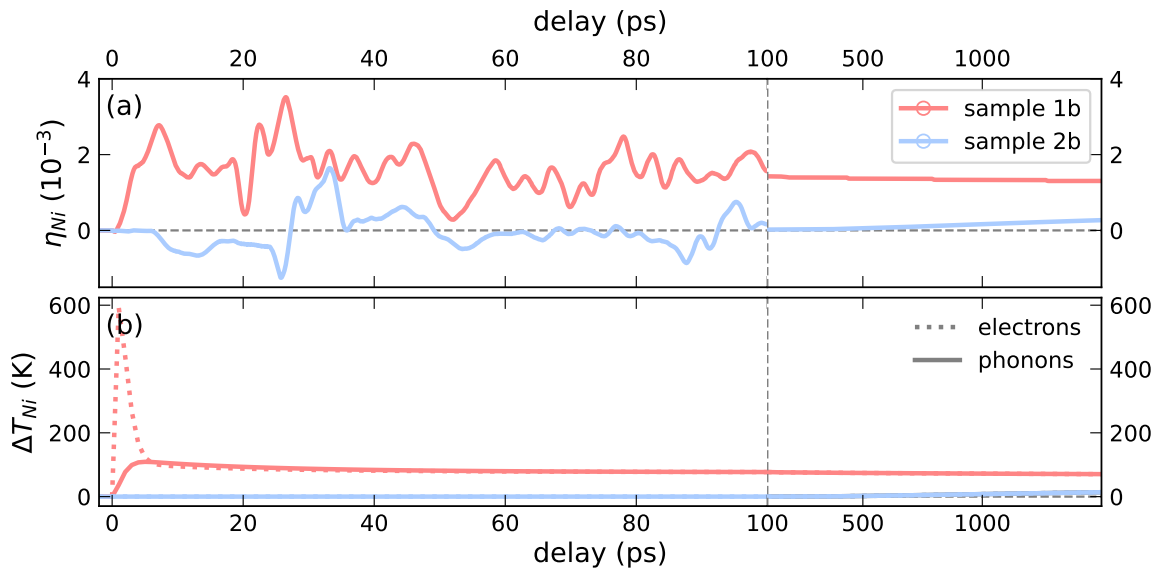
Figure 4.1.3: Laser-induced dynamics in the remaining samples: (a) The average strain and (b) average subsystem temperature response are depicted. Both samples exhibit a similar temperature evolution and therefore strain behavior as their sister samples. While negligible differences in the strain response occur in sample 1b compared to Pt-Cu-Ni, the thicker MgO layer in sample 2b simply delays the sample dynamics. To save computational time, only the quasi-static thermal expansion is plotted after 100 ps in panel (a).

4.2 Temperature and strain determination from transient reflectivity

A different method that provides information about temperature and strain dynamics is the transient reflectivity measurement. Compared to x-ray diffraction measurements, this all-optical technique is significantly easier to apply, which can be a great advantage. A disadvantage, however, is that the measurement signal is not material-selective and that the contributions of the different materials are mixed when measurements are made on multilayered structures containing thin films with respect to the penetration depth of the light. This effect is also clearly visible in the Pt-Cu-Ni results, that are presented in the following section.

Figure 4.2.1 shows the time-dependent reflectivity for sample 1 (top) to sample 3 (bottom). The excitation fluence is kept constant at $11.3\,\mathrm{mJ\,cm^{-2}}$ for all measurements. First of all, some parallels to the UXRD data can be seen in the reflectivity transients. For example, the instantaneous rise of the signal for sample 1a and b indicates the direct energy transfer into the nickel layer. This step-like change can be related to a fast temperature increase, which causes an equally fast change of the refractive index of nickel. In contrast, the average reflectivity signal changes according to the slow heat transport through the MgO barrier in the remaining samples. A general trend of the data is apparent, which for sure provides a decent idea of the temperature dynamics within

the corresponding nickel layer. However, strong oscillations complicate the analysis of the data in each sample except for the inverted sample 1b (Ni-Cu-Pt) significantly. Taking into account the differences between each sample, it becomes obvious that these oscillations occur as soon as a strain pulse propagates into the substrate material. As a consequence to this strain pulse propagation, the refractive index of the SiO_2 becomes locally perturbed, which leads to an additional time-dependent optical interface. This effect is known as time-domain Brillouin scattering [36, 112] and is particularly strong in SiO_2 such that it dominates the presented measurements. Thus, the interpretation of strain dynamics is extremely difficult, which can be seen very well in Pt-MgO-Cu-Ni (orange curve): The strain pulse excited in Pt arrives after 25 ps in the nickel layer and induces a strong change of the reflectivity. Before, the signal stays unaffected due to the lack of heat or strain in nickel. Because of the subsequent propagation of the sound wave into substrate, however, this strain induced initial reflectivity change is followed by strong Brillouin oscillations originating from SiO_2.

Clearly, this is even more extreme in Pt-Cu-Ni, since a strain pulse is also generated directly in nickel after excitation, which is indicated by the following oscillations preventing further conclusions. In fact, only the reflectivity of sample 1b, in which the order of the metal layers is inverted, can be analyzed properly, which stresses the advantage of this sample structure with respect to all-optical experiments. Therefore, for long delays, the average of the measured signal (colored line) is displayed over the original data (light-grey line in the background) to highlight the trend of the signal in those sample that are probed through the substrate.

Apart from the temperature related background, the propagation of the strain pulses originating from nickel and platinum is clearly visible in sample 1b. According to the half round-trip time of the strain pulses within the metal stack of 25 ps modulations occur in the transient. Comparing the amplitudes of these reflectivity changes to the oscillations corresponding to the substrate displayed by the other measurements illustrates the enormous magnitude of the opto-elastic effect in the substrate, which far exceeds that of nickel.

Figure 4.2.1: Time-resolved change of reflectivity of Ni: ΔR is shown for sample 1a (top) to sample 3 (bottom). All curves are shifted for clarity. The meaurements reveal, similar to the UXRD-data but at a qualitative level, the main features of the temperature dynamics: a step-like and slow increase with and without MgO barrier, respectively. Due to the strong strain dependence of the substrate refractive index, the interpretation of the strain dynamics is not straight forward.
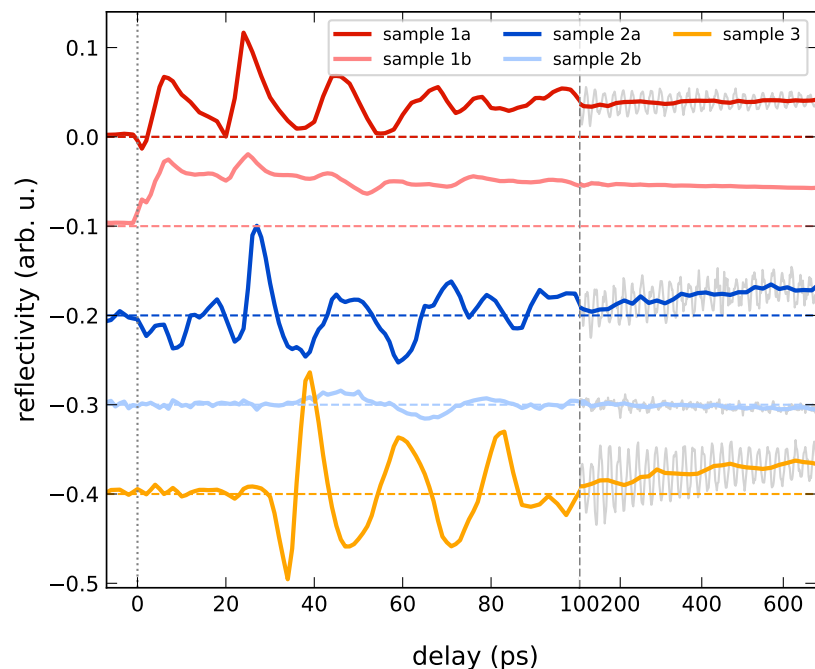
Without precise knowledge of the refractive index and of its temperature and strain dependence for all materials that are within the penetration depth of the probing light, all-optical transient reflectivity yields only qualitative information about the dynamics of the probed material. Nevertheless, in combination with a reasonable modeling of the temperature and strain, this is already

enough to get an instructive picture of the entire structure. Here, for example, we confirm the fast energy transport into the nickel and the related strain pulse generation in sample 1 (Pt-Cu-Ni). In the samples with MgO instead, sound waves arrive depending on the sample thickness at later delays. If we also compare the amplitude of the Brillouin oscillation of sample 2b with all the others, we can conclude from the weak change that the sound pulse generated in the platinum must be quite weak, contrary to expectations. In fact, this result is helpful in order to understand the likewise unexpected behavior of the MOKE-transients, since this sample in total seems to be different than the other Pt-Cu-Ni-heterostuctures.

In summary, UXRD measurements access quantitatively the lattice change of individual materials and thus their temperature evolution, while we obtain only a qualitative overview of the excited dynamics from the simple optical reflectivity measurements. Since a detailed characterization of the samples is beneficial for later interpretation, the additional effort of the UXRD measurements is worthwhile in the context of this thesis, especially when considering the complicated substrate contribution to optical signals.

# Characterization of energy transport by means of demagnetization

In the following chapters the preceding characterization of the strain dynamics and the temperature dynamics, that are derived from UXRD measurements, are now complemented by the investigation of the response of the magnetic system upon laser-excitation. Thus, we obtain a rather complete picture of the excited energy transfer dynamics within the metals. At the center of this thesis are two aspects of magnetization dynamics: ultrafast demagnetization and magnetization precession (Chap. 6). Ultrafast demagnetization is a direct consequence of an as well ultrafast excitation of the electronic system, from which the energy is redistributed among the degrees of freedom of the solid. Therefore, this phenomenon provides information on energy transfer processes and the microscopic interactions between the subsystems. Here, we study magnetization dynamics of Pt-Cu-Ni and Pt-Cu-MgO-Ni, that both exhibit a different energy transport behavior, by measuring the response of the magnetic detection layer using the magneto-optical Kerr effect (MOKE). The MOKE data is compared to simulations of the time-dependent magnetization using a m3TM, that is calibrated by the UXRD results.

5.1 Slow vs. fast dynamics within the m3TM

Following the idea by Jang et al. [113] to use a magnetic layer as an all-optical magnetic thermometer to study non-equilibrium dynamics of a heterostructure, the demagnetization in the Pt-Cu-Ni structures is at the center of this chapter. In the mentioned work, the authors apply a purely phenomenological 3TM to model the response of a thin Co layer sandwiched between Pt, however, under strictly limiting conditions such as small temperature changes of $50\,\mathrm{K}$ corresponding to weak excitations only. From their analysis, they are able to extract the electron-phonon coupling of Pt a lot easier than by reflectivity measurements, for example, demonstrating the potential of this idea. It would be a remarkable success to implement such a thermometer in the most general case, which is, however, still one of the major challenges in ultrafast magnetism, since there is no consistent model that fully describes ultrafast demagnetization and remagnetization correctly.

Within the scope of this thesis, I study the temporal behavior of the magnetization of the buried $20\,\mathrm{nm}$ nickel layer by use of the magneto-optical Kerr effect in sample 1 (Pt-Cu-Ni) and sample 2 (Pt-Cu-MgO-Ni). The energy transport in both heterostructures is very different due to the insulating MgO barrier in the second sample, which is also clearly visible in figure 5.1.1. It illustrates the transient MOKE signal S of each sample after exciting the Pt transducer by $13.8\,\mathrm{mJ\,cm^{-2}}$. An external field of $\mu_0 H_{\mathrm{ext}} = 800\,\mathrm{mT}$ saturates the magnetization in out-of-plane direction, while $400\,\mathrm{nm}$ laser pulses incident from the substrate side opposite to the pump pulse probe the magnetization change upon excitation. The probing through the substrate (see Chap. 3.5), however, comes along with a poor signal-to-noise ratio. Thus, the quality of the static hysteresis data, that is dominated by the paramagnetic substrate contribution, unfortunately does not allow for a calibration of the time-resolved MOKE data in terms of magnetization changes. Nevertheless, it is still possible to compare the relative magnitude of demagnetization in each sample, since the

MOKE signal is proportional to M. In agreement with the previous UXRD results (see Fig. 4.1.1), both structures exhibit the same demagnetization amplitude for large delays. Due to the equal excitation and hence absorption, both samples must exhibit the same temperatures in thermal equilibrium at late delays, which is well confirmed by the demagnetization transients. In contrast, strong differences occur for short delays.

As expected, nickel demagnetizes slowly according to the likewise slow heat transport into the magnetic layer by phonons in sample 2. Despite of this heating, nickel is in a quasi-equilibrium throughout the process and strives only for thermalization with the remaining excited metal layers. After about one nanosecond, a temperature balance over the whole metal stack is established as well as the corresponding minimum demagnetization.
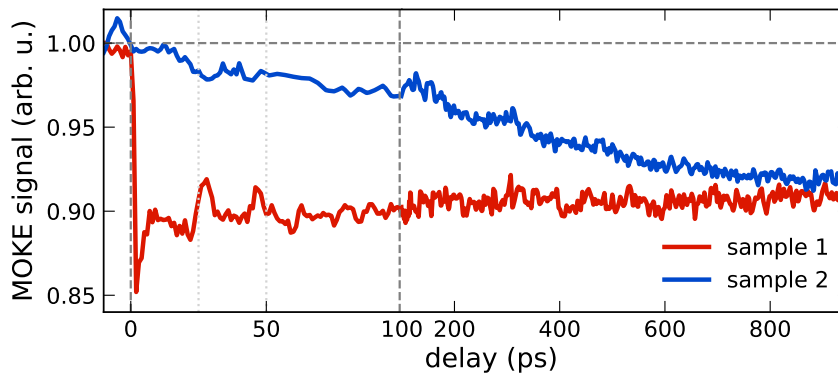
Figure 5.1.1: Fast vs. slow excitation: The MOKE-transients, that are measured with saturated magnetization in out-of-plane direction with $\mu_0 H_{\text{ext}} = 800\,\text{mT}$ for an excitation fluence of $13.8\,\text{mJ}\,\text{cm}^{-2}$, show a very fast demagnetization in sample 1 and and much slower demagnetization in sample 2 according to the speed of energy transfer into the nickel. On long timescales, the demagnetization is determined by the equilibrium temperature of the system and is therefore equal in both samples. The light-gray dotted lines mark the time of arrival of a strain pulse in Pt-Cu-Ni each, that can be clearly observed in the MOKE-signal.

In contrast, sample 1 (Pt-Cu-Ni) exhibits an ultrafast demagnetization almost immediately after excitation in agreement with previous observations in single nickel films [5, 6, 114] as well as other ferromagnetic materials embedded within heterostructures [17, 79]. This ultrafast decrease of magnetization is followed by a remagnetization that is initially fast and slows down significantly after a few picoseconds. Moreover, signatures of strain wave propagation can be clearly observed in the MOKE signal. The timings of the corresponding modulations of the signal marked by dotted lines match very well the time of arrival of the strain pulses in the nickel, which unambiguously shows their origin in the lattice dynamics. However, since this is not the subject of this thesis, this unexpected behavior will not be discussed here further.

In agreement with previous studies for very similar sample structures with an integrated CoPt-multilayer instead of Ni by Bergeard et al. [17], the presented data confirms that the character of energy deposition into the magnetic material is not of great importance regarding ultrafast magnetization manipulation. Both direct photon absorption as well as hot electron pulses are sufficient in terms of ultrafast demagnetization. However, the question remains as to the microscopic origin of this rapid demagnetization. The authors of the mentioned work [17] suggest the Elliott-Yafet spin flip scattering as the dominant mechanism for demagnetization in their experiment on the basis of a qualitative agreement between their measurements and simulations of the transient magnetization. The modeling is performed within the framework of the microscopic three-temperatures-model [64] considering ballistic electron transport responsible for the ultrafast energy transfer into the magnetic layer. Nevertheless, transport effects may play an equally important role in ultrafast demagnetization, especially in the investigated structures, considering the nature of the energy

deposition into the magnetic film. Both approaches, i.e., spin-flip scattering and superdiffusive spin transport, agree that magnetization dynamics are mainly governed by the energy transfer into the spin system and hence the interactions between the electrons, phonons, and spins directly after excitation. Thus, in order to compare simulations of magnetization dynamics to measured data on a quantitative level, it is crucial in any case to consider the remaining subsystem dynamics as well. Pudell et al., for instance, demonstrated by investigating the strain response of Pt-Cu-Ni that a purely diffusive transport model instead of ballistic electrons proposed by Bergeard et al. is sufficient to describe the energy deposition into the buried nickel [14]. This result stresses once again the importance of careful consideration of all subsystems, which is still missing in many works [79, 115, 116].

Although there are several experiments giving evidence for both mechanisms contributing to magnetization dynamics in ferromagnets, i.e., spin-flip scattering and spin transport, it is reasonable to investigate both models separately first. By this means, it is possible to work out possible weaknesses and potential links to other models. Here, the m3TM is tested by comparing its predictions to measured MOKE transients for the two cases of ultrafast and slow excitation in sample 1 and 2, respectively. In contrast to most of the other works, the electron and phonon temperatures, which mainly determine the temporal evolution of the magnetization within the m3TM (see Eq. 5.2.1), are also taken into account experimentally via the lattice dynamics measurements, which are further used to calibrate the corresponding temperature dynamics (see Chap. 4). Since the magnetization does not affect the other subsystems within the model, the energy exchange continues to occur only between electrons and phonons. Thus, the 2TM applied previously to the modeling of the lattice dynamics can be also used for the m3TM simulations with the corresponding thermophysical material parameters. The remaining material constants summarized in the parameter R in equation 5.2.1 are taken from [64] complementing the list in table 4.1.1. The excitation fluence is a free parameter within the modeling. It is interesting to note that it was necessary to assume a significantly higher excitation in the simulation compared to the incident fluence applied in the experiment. This difference is easily explained when considering the assumptions of the multilayer transfer matrix formalism used to calculate the optical absorption. The model predicts a reflectivity of the Pt surface of 94% neglecting any possible roughness or other imperfections. From a simple crosscheck measurement, I determined an actual reflectivity about 80 % for all samples, which in turn leads to a much higher absorption than calculated, although the spatial profile is considered to be correct.

Figure 5.1.2 displays the comparison between the measurements, that are described above, and the calculated m3TM-simulation results. Both MOKE transients are modeled using an excitation fluence that is adjusted with respect to the UXRD simulation fluence considering the different pump pulse angles in both experiments. In order to compare the model to the measured transients, the MOKE data is scaled to match the calculated amount of demagnetization at long delays when the system is in thermal equilibrium. Justified by a comparison to calibrated measurement data (sample 1b), that will be shown below, this scaling approach provides a reliable qualitative picture, that highlights the main characteristics of the m3TM.

Since the m3TM is meant to describe the time-dependent response of the magnetic system upon ultrafast excitation, it is also expected to describe the equilibrium situation before excitation properly. Thus, slow near-equilibrium dynamics, such as occurring in sample 2 (Pt-Cu-MgO-Ni), should be also reproduced very well. In fact, both the m3TM as well as the temperature dependent static magnetization of nickel taken from literature [62] (see Fig. 5.1.2b) are sufficient to predict the magnetization dynamics. Although, the experimentally determined static magnetization $M(T)$ does not exactly match the one calculated from the m3TM (see Fig. 5.1.2c), which leads to small deviations of the calculated time-dependence of the magnetization using the simulated temperatures. Nevertheless, equilibrium situations, such as in sample 2 (Pt-Cu-MgO-Ni), can indeed be well described within the m3TM.

In contrast, extreme deviations between measurement and model occur as soon as energy is

transferred very rapidly into the electronic subsystem so that the total system is driven out of equilibrium, as it is the case in sample 1 (Pt-Cu-Ni) shortly after excitation (see Fig. 5.1.2a). Although the m3TM was not expected to describe the process of demagnetization in this heterostructure sufficiently, since it does not account for transport effects for instance, this disagreement illustrates that a further evaluation of the model is required.
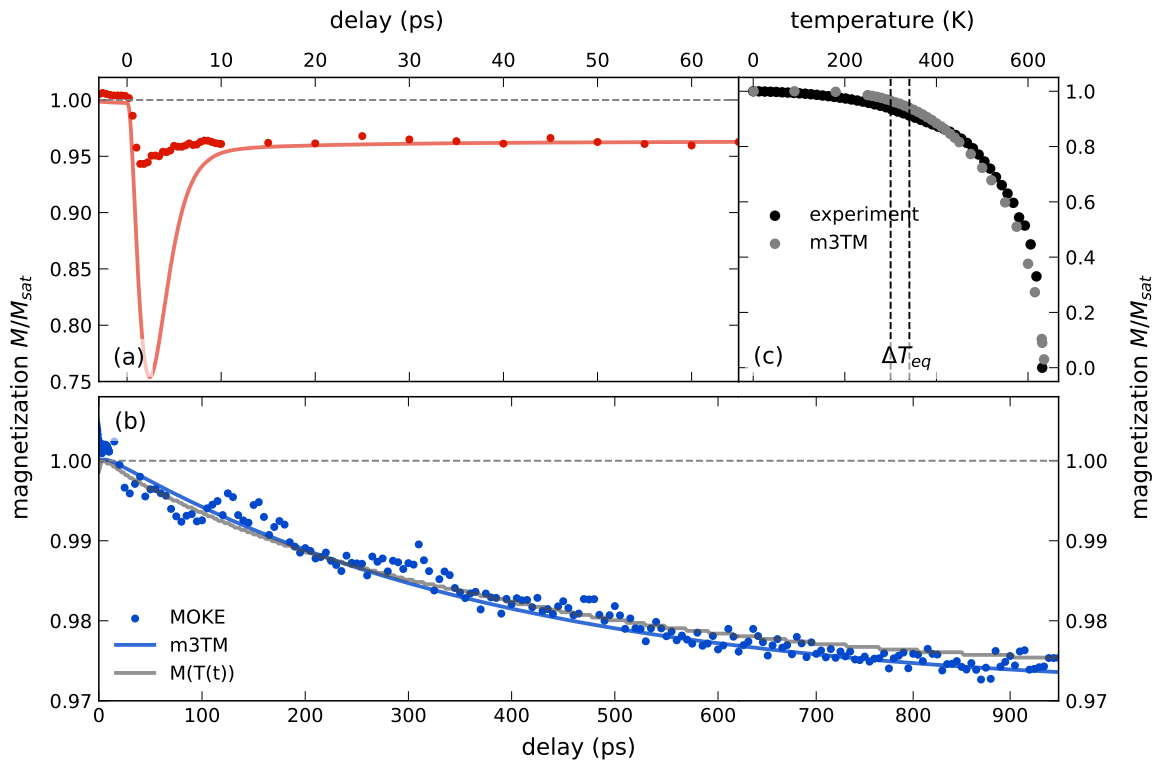
Figure 5.1.2: m3TM modeling: MOKE measurements for Pt-Cu-Ni (a) and Pt-Cu-MgO-Ni (b) are compared to simulations of the m3TM, in which the temperature dynamics are calibrated by the UXRD measurements. Since nickel is in a near-equilibrium in sample 2 (Pt-Cu-MgO-Ni), both the m3TM as well as the static temperature-dependent magnetization (c) are sufficient in order to model the measured transients. Unlike Pt-Cu-Ni, where the simulation does not match the data at all as long as the subsystems are in strong non-equilibrium. The experimental data of the static magnetization in nickel (c) is taken from [62] while the modeled $M(T)$ data is extracted from the simulated magnetization transients for varying initial temperatures before excitation ($t < 0$). The interval marked by the dashed lines in (c) corresponds to the temperature change after equilibration that is required to achieve the observed demagnetization $M/M_{\text{sat}}(1\,\text{ns})$.

5.2 Comparison of the strain thermometer to the magnetic thermometer

For the further analysis of the m3TM, simulations will be compared to measurement data of sample 1b (Ni-Cu-Pt) instead of sample 1 (Pt-Cu-Ni), which is the inverted version of the original structure. In contrast to sample 1, which has to be probed through the paramagnetic substrate, leading to poor quality of the static hysteresis measurement, the magnetic nickel in sample 1b can be accessed directly in the MOKE measurements. This simplifies the interpretation of the static measurement drastically and allows for a reliable calibration of the time-resolved MOKE data, which makes sample 1b ideal for the following analysis. Furthermore, consistent 2TM and UXRD simulations confirm no significant deviations of the temperatures and strain dynamics between both samples at the relevant timescales (see Chap. 4), thus both structures are considered equal. Applying the UXRD simulation fluence that is scaled by the ratio of the experimental fluences $F_{\text{MOKE}}/F_{\text{UXRD}}$ provides a good agreement between measured MOKE transients and calculated

magnetization for various excitation fluences at large delays, as expected for equilibrium situations. This shows above all that a calibration of the measured data using the simulations at late delays is indeed possible, which has been done in the previous section for samples 1 and 2 (see Fig. 5.1.2).

The modeled magnetization dynamics in sample 1 depicted in figure 5.2.1a exhibit a highly exaggerated initial maximum demagnetization ΔM_{max}, i.e., minimum magnetization, as well as a demagnetization time τ_{demag} that does not match with the measured data under the given parameters. Since this disagreement is also reproduced independently for sample 1b, the origin is clearly related to the modeling and cannot be explained by measurement artifacts (see Fig. 5.2.1a). Keeping the temperature dynamics as determined from the strain data, it is not possible to obtain even an approximate agreement between measurement and model for early delays. In this case, the parameter R, that scales the demagnetization rate (see Eq. 5.2.2), is the only remaining free parameter for adjusting the calculated dynamics (see Eq. 5.2.1):

$$\frac{dm}{dt} = Rm\frac{T_{ph}}{T_C}\left(1 - m\coth\left(\frac{mT_C}{T_{el}}\right)\right),$$

(5.2.1)

where R combines a range of material-specific constants, one of which is the spin-flip probability taking into account the underlying mechanism leading to demagnetization:

$$R = \frac{4\alpha_{sf}g\,k_B\,T_C{}^2V_{at}}{(\mu_{at}/\mu_B)E_D{}^2}.$$

(5.2.2)

By increasing R with respect to the value calculated by Koopmans et al. [64], which can be interpreted as an increase of the spin-flip probability α_{sf}, the demagnetization time τ_{demag} is slightly reduced. However, at the same time this results in an amplification of the initial demagnetization so that in turn a total demagnetization occurs at early delays even before the simulated time t_{min}, at which the minimum magnetization is reached, agrees with the data.
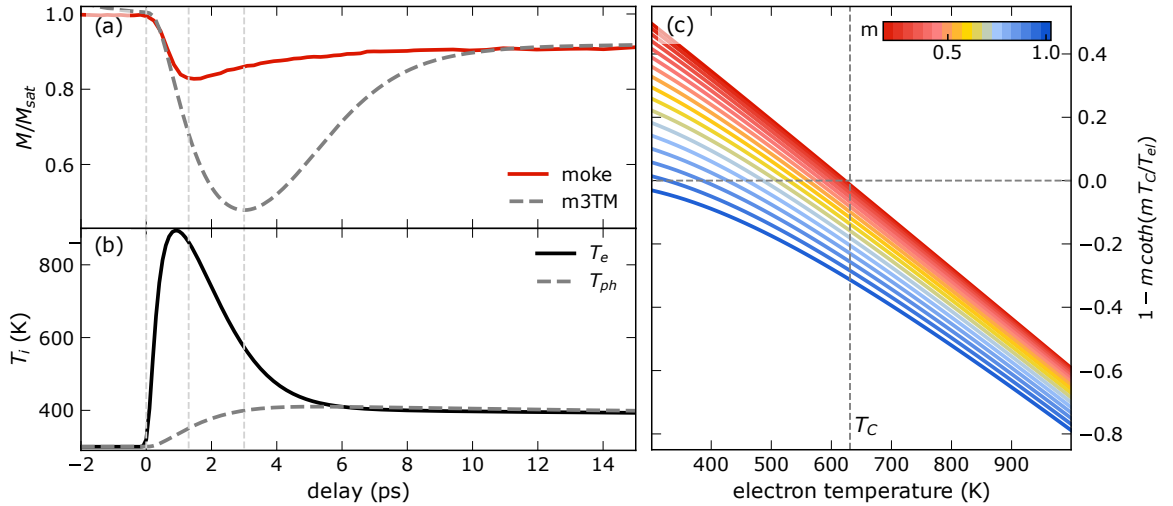
Figure 5.2.1: Characteristics of the m3TM: (a) The measured time-dependent magnetization reaches its minimum significantly earlier than the simulated transient, which is indicated by the dashed lines corresponding to respective minima. The timescales of modeled magnetization and electron and phonon temperatures, that are depicted in panel (b), suggest that the demagnetization time is mainly determined by the electron-phonon coupling in nickel. (c) By decreasing T_{el} the sign of the magnetization change switches at an critical electron temperature from demagnetization ($dm/dt < 0$) to remagnetization ($dm/dt > 0$), which is also governed by the magnetization m (see Eq. 5.2.1). In order to obtain an ultrafast demagnetization within 1 ps, a fast decreasing electron temperature is crucial, which is additionally enhanced by a fast increase of the phonon temperature.

Accordingly, the MOKE data clearly reveal that the temperature calibration to the strain measurements needs to be adjusted in order to match the measured magnetization dynamics. Similar to Jang et al. [113], we use the magnetic layer within the heterostructure as a sensor of energy exchange to complement the information provided by lattice dynamics, which is not sufficiently conclusive on its own on the relevant timescales. However, since the observed discrepancy occurs only within the first picoseconds when the system is not yet thermalized, but agrees very well at large delays, it is import to keep the long-term dynamics unaffected.

Comparing the simulated magnetization transient to the corresponding time-dependent temperatures shows a minimum magnetization appearing only for a considerable decrease of the electron or increase of the phonon temperature (see Fig. 5.2.1a, b). Accordingly, the demagnetization rate must be determined substantially by the electron-phonon-coupling constant in Ni in addition to the direct contribution of g_{Ni} to the scaling parameter R. Due to the direct proportionality of dm/dt to T_{ph}, the de- or remagnetization rate is affected by the phonon temperature. However, it is the electron system making the main impact on the temporal evolution of the magnetization, since the electronic temperature determines the sign of the change of the magnetization dm/dt in equation 5.2.1. The behavior of the decisive factor $(1 - m\coth(mT_C/T_{el}))$ depending on the electron temperature is illustrated for several values of $m = M/M_{sat}$ in figure 5.2.1c. There are two main aspects to note: First, at temperatures high above the Curie point, which is $T_C = 631\,\mathrm{K}$ in the example, the material demagnetizes always. With decreasing temperature, however, the sign of dm/dt switches and induces a remagnetization. Second, the critical temperature corresponding to this sign change shifts to higher temperatures with decreasing magnetization m. The phonon temperature only reinforces these magnetization dynamics, as it directly affects the de- or remagnetization rate (see Eq. 5.2.1).
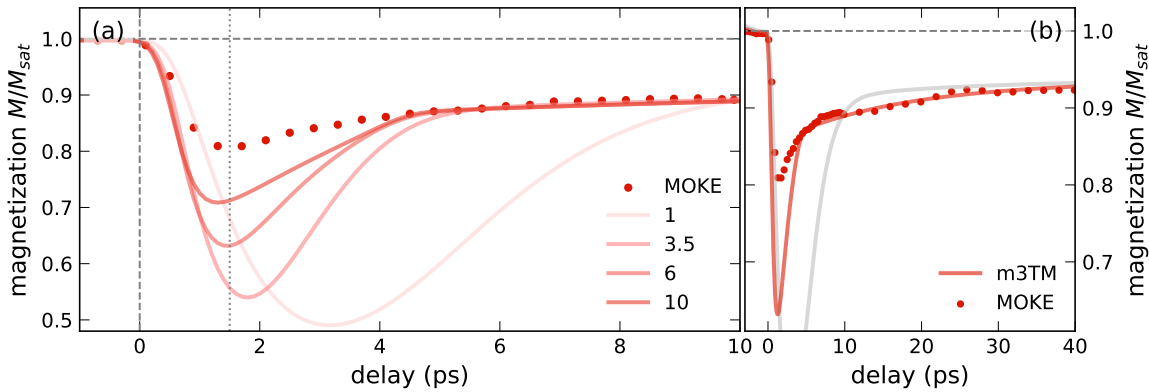
Figure 5.2.2: Electron-Phonon coupling in the m3TM: (a) The influence of the electron-phonon coupling in nickel is illustrated by comparing simulated magnetization transients for varying electron-phonon coupling constants (g_{Ni} from table 4.1.1 multiplied by the indicated factor) to the MOKE signal in Ni-Cu-Pt. (b) The calculation fits the data best assuming an electron-phonon coupling g_{Ni} increased by a factor of six. The gray line represents the initial modeling result, that is initially too slow, but also does not captures the data after 10 ps in thermal equilibrium.

Varying the electron-phonon coupling for the purpose of adjusting the temperature evolution in nickel is a appropriate choice for several reasons. Most importantly, it fulfills the requirement of changing the initial dynamics but not affecting the final equilibrium temperature and hence the magnetization, in contrast to heat capacities that also play an important role for temperature dynamics. Moreover, g is less precisely determined, and values are reported in literature over a wide range [50], while C_i is well known. The resulting transients for varying electron-phonon coupling constants, that are convoluted with a temporal resolution of 200 fs and furthermore weighted with the spatial penetration profile of the probing light, are depicted in figure 5.2.2 together with

the corresponding MOKE data set. The simulated time-dependent magnetization exhibits the expected trend of decreasing demagnetization time τ_{demag} as g_{Ni} increases. Furthermore, the initial demagnetization amplitude is reduced significantly, so the calculations get closer to the measured MOKE signal. With respect to the temporal evolution, an increased electron-phonon coupling of nickel by the factor of six fits the data best, and nicely reproduces the fluence series measured in Ni-Cu-Pt for delays larger than 7 ps (see Fig. 5.2.3). However, the initial demagnetization is still about twice as high compared to the measured transients for each fluence.
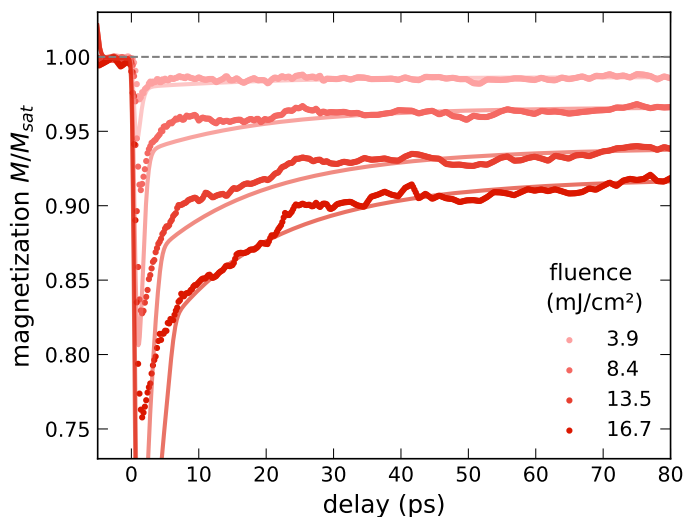
Figure 5.2.3: Fluence-series in Ni-Cu-Pt: The temporal evolution of the magnetization in Ni-Cu-Pt (solid lines) is well reproduced by the m3TM (dashed lines) neglecting the modulations induced by the propagating strain waves and the first few picoseconds. Especially the good fit to the recovery of the magnetization between 8 and 40 ps, that has not been captured by a weaker g_{Ni}, supports the adjusted electron-phonon-coupling in Ni.

Even though an improvement can be reached by increasing the electron-phonon coupling constant, resulting in a faster decrease in electron temperature, the maximum demagnetization ΔM_{max} remains highly overestimated. It would be easy to tailor the simulation until it agrees with the MOKE data by adjusting the temperature dynamics in nickel even further, which, however, is not the aim of this analysis. It is important to note that an increase of g_{Ni} modifies the temperatures dynamics not only in nickel but also in the other metals of the heterostructure, which subsequently affects the strain dynamics leading to deviations from the measured lattice dynamics used for the calibration. Only small changes of g_{Ni} can be compensated by other material parameters in all constituent metal layers. In sample 1, however, the energy distribution among platinum and nickel in the first picoseconds is significantly determined by the electron-phonon coupling in both metals. Since Ni is electronically isolated in the samples with MgO, a significant adjustment of the Pt parameters would result in a more pronounced change of the temperature dynamics in sample 2 and 3. Thus, the extracted thermophysical parameters are fixed to a certain degree, as demonstrated by the good agreement between the UXRD simulations and the measured strain dynamics in all heterostructures using one set of parameters. In fact, the presented results are a well-founded indicator that the deviations between calculated magnetization within the m3TM and the measured MOKE signal result from a more fundamental aspect.
In literature, there are several examples presenting apparently successful modeling of ultrafast magnetization dynamics, also within the framework of the m3TM. In contrast to the simulations in these works, however, the thermophysical parameters used here are calibrated by our UXRD measurements and correspond to independent literature values. A comparison reveals two striking differences, which are an increased electron-phonon coupling constant and a drastically reduced

phonon heat capacity (compare Tab. 5.2.1).

	g_{Ni} ($\times 10^{17}\,\text{W}\,\text{m}^{-3}\,\text{K}^{-1}$)	$C_{\text{phon, Ni}}$ ($\text{J}\,\text{cm}^{-3}\,\text{K}^{-1}$)
UXRD sim	3.60	3.94
Beaurepaire et al. 1996 [5]	8.00	2.20
Koopmans et al. 2010 [64]		
Roth et al. 2012 [116]	40.50	2.33

Table 5.2.1: Comparison of Ni-parameters: The electron-phonon coupling constant and phonon heat capacity of nickel from ultrafast magnetization dynamics modeling and the UXRD calibration are compared.

These adjustments cause a faster increase of the phonon temperature and decrease of the electron temperature, resulting in a significantly shorter demagnetization time compared to the model used initially here. In contrast to the electron-phonon-coupling constant, which is, as discussed before, a rather free parameter, the considered phonon heat capacity, that is only about 60% of the common value, dramatically affects the resulting temperature dynamics not only directly after excitation but also in thermal equilibrium. The corresponding final phonon temperature is significantly higher leading consequently to a stronger demagnetization. So, similar to the analysis presented here, the other studies are unable to describe ultrafast demagnetization simultaneously with the quasi-equilibrium dynamics on larger timescales.

In this thesis supported by two independent experiments, i.e., UXRD and MOKE, the temperature dynamics in thermal equilibrium are determined unquestionable correctly. In contrast to lattice dynamics, however, it is not possible to describe the ultrafast response of the magnetization to the excitation properly using the same material parameters as for modeling UXRD, underlining the difference in timescales of these macroscopic responses. Even more importantly, these results point out a fundamental problem of the m3TM, that is mainly related to the involved 2TM. The essential assumption of temperature models in general is an internal thermal equilibrium of the considered subsystems. In terms of a 2TM, that describes almost the simplest case considering only two heat baths represented by electrons and phonons, this seems not to be adequate on sub-picosecond timescales. However, assuming an internal equilibrium is indeed reasonable for the electronic subsystem, since electrons equilibrate within tens of femtoseconds, as shown by several experiments [48, 49]. In contrast, a non-equilibrium of the phonon system, which includes multiple distinct modes, has been observed remaining up to several 100 ps by recent studies [117–120]. Time-resolved and wave-vector dependent measurements of the phonon population reveal that excited electrons preferentially scatter with high energy phonons from the Brillouin-zone (BZ) edge. Phonon modes near the BZ center, however, are occupied much slower, which is attributed to a weaker electron-phonon coupling and inefficient phonon-phonon scattering [120, 121]. Due to the phonon-mode dependence of the electron-phonon coupling, it can be considered time-dependent possibly explaining the different values extracted from lattice and magnetization response as well as the wide range of literature values. Furthermore, these mentioned studies demonstrate that not all phonons contribute to the non-equilibrium dynamics within the first picoseconds, which rationalizes effectively a smaller phonon heat capacity.

Taking into account those results, the presented analysis shows limitations of the m3TM that have not been discussed in detail so far. In order to describe magnetization dynamics correctly covering both subpicosecond as well as picosecond timescales, modifications regarding the phonon system of the microscopic three-temperatures model are required. For this purpose, a full picture including a careful treatment of all contributing subsystems is necessary, as mentioned already several times throughout this chapter, since it is the interplay between the subsystems governing ultrafast dynamics in solid state materials. Even though the presented investigation demonstrated that the strain response measured by time-resolved x-ray diffraction is probably too slow to calibrate the energy transfer dynamics unambiguously on the subpicosecond timescale, the analysis still benefits

extremely from the combination of UXRD and MOKE, which is undeniably useful in order to obtain a detailed picture of the non-equilibrium state of multilayered samples and a better understanding of the spin dynamics in particular. In terms of an evaluation of the m3TM, lattice dynamics are in fact a well suited experimental technique to complement the magnetization measurements considering the limiting conditions of the model, although other experimental techniques could be more suitable for future studies.

As a final remark, it is good to note that other possible effects contributing to the measured magnetization response have not been discussed yet, including the role of the time-dependent spatial profile of the magnetization, which also has not been investigated experimentally very often so far. As an prominent example, superdiffusive spin transport has to be mentioned. This non-local effect does not necessarily lead to a reduction of the magnetization but to a redistribution of the spins, which consequently conceals the actual demagnetization, especially in optically thick samples. Due to its large thickness of 20 nm relative to the 12 nm skin depth of the 400 nm probing light, it is not possible to probe the nickel layer in the present MOKE experiments homogeneously. As a result, local and non-local effects are weighted differently complicating efforts to compare measurements and models even further.

Comparing the efficiency of excitation mechanisms of magnetization precession

Ultrafast laser excitation of a ferromagnetic material not only induces ultrafast demagnetization, but it can also drive a coherent precessional motion of the magnetic moments, which can be observed as oscillations of the m_z-component in the polar-MOKE experiment typically for hundreds of picoseconds. As already explained in chapter 2.3, there are various mechanisms to excite magnetization precession: by thermally induced changes of the magneto-crystalline anisotropy constants and demagnetization, and due to magneto-elastic coupling, which links lattice dynamics to magnetization.

By analyzing the detected precession amplitudes under variation of the external magnetic field angle with respect to the sample surface in the Pt-Cu-Ni heterostructures introduced in chapter 3, the impact of these driving mechanisms is investigated in this chapter. In general, it is not straightforward to disentangle the respective contributions and treat the driving effects separately. Due to the ultrafast energy deposition into the ferromagnet, the temperature of the system increases rapidly, which is additionally accompanied by an demagnetization and a complex strain response, that, as discussed previously, is composed of an incoherent thermal expansion superimposed by propagating strain waves. All these laser-induced dynamics lead to individual changes of the effective field. However, our tailored sample design of each heterostructure is key in order to consider the driving mechanisms separately. As shown by the UXRD measurements (see Chap. 4), the position of the MgO-layer within the metal stack modifies the resulting temperature and strain dynamics significantly leading to a separation of heat and strain due to their different propagation speed. Since both contributions arrive in the magnetic layer at different times, it is possible to compare the impact of the distinct temperature and strain dynamics on the magnetization under comparable conditions.

6.1 Angle-dependent MOKE-measurements

Just as for the demagnetization measurements, the following experiments were conducted with a polar-MOKE setup applying an indirect excitation geometry, which has been already shown in figure 3.5.3. Instead of an electro-magnet, however, a commercial neodynium permanent magnet is used in order to apply the external field along various angles. The magnet is mounted on a rotation stage above the sample (see Fig. 6.1.1). During the measurement, it is placed as close as possible to the probed sample spot, which leads to an external field strength of $\mu_0 H_{\mathrm{ext}} \approx 400\,\mathrm{mT}$ at the probed sample spot, which is below the saturation field of $\mu_0 H_{\mathrm{sat}} \approx 600\,\mathrm{mT}$ of the investigated nickel films. In this way, the magnetization of the thin nickel film is canted away from the in-plane easy axis along a direction between the external field angle and the sample surface. The rotation axis of the magnet is aligned so that it crosses the probed region to ensure the highest possible homogeneity of the field at this spot.

Figure 6.1.1: Rotatable magnet setup: Instead of the electro-magnet (see Fig. 3.5.3), we use a commercial Neodymium permanent magnet, that is mounted on a rotation stage above the sample and placed as close as possible to the probing spot. Thus, it is possible to apply a constant external magnetic field under an arbitrary angle ϕ with respect to the surface normal. The rotational axis of the permanent magnet is aligned to cross the probed sample spot before each measurement.
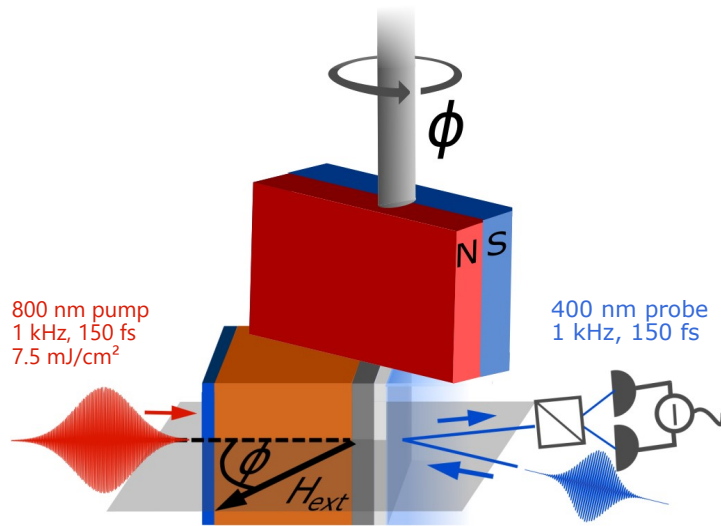
Figure 6.1.2 displays an exemplary measurement series corresponding to sample 1 (Pt-Cu-Ni) upon an excitation fluence of $13.5\,\mathrm{mJ\,cm^{-2}}$. The external magnetic field angle ϕ is varied between $0°$ (out-of-plane direction) and $360°$ in $5°$ steps, and for each field direction the time-dependent polarization rotation of the probe light is detected. The measurement signal exhibits a rapid, step-like change directly after excitation, which is followed by pronounced oscillations of field angle-dependent frequencies and amplitudes observable up to more than $700\,\mathrm{ps}$ (see Fig. 6.1.2a and b). The fast decrease of the signal corresponds to a heat-induced ultrafast demagnetization in nickel, that has been discussed in detail in the previous chapter. In contrast, oscillations are not attributed to a time-dependent change of the absolute value of the magnetization but to its precession, which is excited with varying efficiency under the chosen experimental geometry. The UXRD experiments and the demagnetization measurements demonstrated ultrafast temperature- and strain dynamics and ultrafast demagnetization, respectively, induced in the magnetic Ni-layer of the Pt-Cu-Ni, which can in turn induce changes of the material-specific effective field via an individual contribution that determines the equilibrium orientation of the magnetization. As a consequence to this time-dependent effective field contributions, a torque acts on the magnetization to initiate precession about the effective field direction, which in turn can be detected as an oscillation of the M_z-component in the polar-MOKE experiment.

Panel (b) of figure 6.1.2 shows the results of the full rotation in a 2D colorplot, where the MOKE signal is plotted as a function of time and external field angle. The measured data exhibits a distinct symmetry determined by the relative orientation of $\vec{H}_{\mathrm{ext}}$ with respect to the in-plane direction ($90°$ and $270°$). Additionally, panel (c) shows the Fourier-amplitude as function of frequency and external field angle (s. 6.1.2c) calculated using a discrete Fourier-transformation (FFT) algorithm. Apart from high FFT amplitudes at low frequencies attributed to the slowly varying background in the measurement signal, a distinct peak can be observed for each external field angle in the frequency interval between 5 and 20 GHz, corresponding to the respective oscillation. From these FFT maxima, frequencies and amplitudes of the magnetization precession can be obtained. The FFT-data underline the previously mentioned symmetry of the signal with respect to the magnetic field angle. A clear rise in precession frequency can be seen as the external field is oriented increasingly parallel to the sample plane, i.e., parallel to the easy axis ($90°$ and $270°$), which in turn means a decrease in frequency as $\vec{H}_{\mathrm{ext}}$ is aligned more perpendicular to the surface plane ($0°$ and $180°$). However, small frequency differences, which are clearly visible when comparing $0°$ and $180°$, for example, indicate a less than ideal alignment of the rotation center of the magnet, resulting in stray fields that cause a small asymmetry in opposite field directions (see Fig. 6.1.2c).
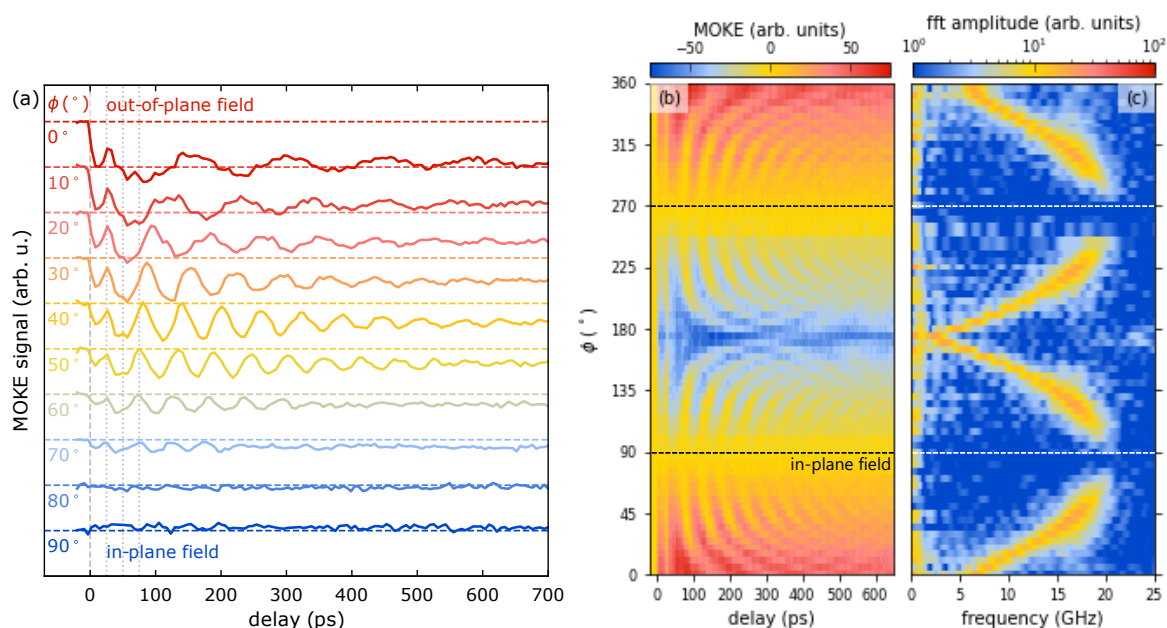
Figure 6.1.2: Angle-dependent magnetization precession: (a) The MOKE signal, that is measured under varying external field angles ϕ with respect to the surface normal, exhibits a distinct angle dependence of the precession frequency and amplitudes. The frequency is mainly determined by the in-plane component of the external magnetic field, explaining the observed increase of f towards 90° and 270° corresponding to an in-plane orientation. (b) A full rotation of the Kerr-signal is plotted as a function of time and field angle. (c) The corresponding Fourier-spectra obtained from each MOKE transient are depicted as a 2D-plot as a function of frequency and field angle. These spectra provide amplitude and frequency of the corresponding magnetization precession.

The observed angle-dependence of the detected oscillations, that is substantially determined by the in-plane component of the external magnetic field, clearly identifies them as spin waves. The rotation of the magnetic field can be considered as an variation of the in-plane field strength, which reaches its maximum for a parallel alignment of the external field with respect to the sample surface. Also, the absolute value of the effective field, which is typically considered when studying magnetization precession, is then at a maximum. As introduced in chapter 2.3, $\vec{H}_{\text{eff}}$ is composed of the material-specific intrinsic anisotropy fields, that are mainly governed by the sample symmetry, and the external magnetic field. The external field contributes to the free energy of the ferromagnetic system via the Zeeman energy and can tilt the magnetization away from its preferential direction. However, its z-component is partially compensated by the field attributed to the shape anisotropy, that is aligned antiparallel, as long as the total external field is below the saturation field strength (see chapter 2.3). As a result, the absolute value of the effective field increases with increasing in-plane field component of the external field $\vec{H}_{\text{ext}}$. Furthermore, since the initial non-equilibrium induced by the ultrashort laser pulse relaxes back significantly faster than the spins respond to the resulting time-dependent torque, the detected magnetization precession can be described by the equilibrium parameters, assigning the precession to the ferromagnetic resonance (FMR), the fundamental spin wave mode with $k = 0$. Since the FMR frequency increases with increasing field strength [122], this can also be observed in the measured data for increasing external field angles.

In contrast to the frequency, the oscillation amplitude is highly sensitive to the driving mechanism and its time dependence and will therefore be carefully analyzed below. It is important to note that in addition to the physical origin to the varying amplitudes, another effect related to the detection occurs causing the detected amplitude to increase with increasingly in-plane alignment of the external field. For an almost in-plane orientation of the magnetic field, the equilibrium

magnetization direction is also almost in-plane. Since the precession occurs around this equilibrium orientation its amplitude has a major M_z-component in this geometry, which provides a higher polar-MOKE signal compared to a precessional motion around an axis with a large out-of-plane component dictated by an out-of-plane orientation of $\vec{H}_{ext}$.

6.2 Heat and coherent strain as driving mechanisms of magnetization precession

To analyze the influence of the varying temperature and strain dynamics in each sample, magnetization precession is investigated in all heterostructures under comparable external excitation conditions. Precession is usually described by four parameters: frequency, amplitude, phase, and decay. It is well known that only the amplitude and the phase of the precession depend on the specific excitation mechanism, while the frequency is only determined by equilibrium parameters, provided that negligible demagnetization is considered [8, 74]. For this reason, the main focus of this chapter is on analyzing the angular dependence of the amplitudes in the individual samples. In order to obtain a measurement signal as large as possible from the buried nickel film, the highest possible fluence of $7.5\,\mathrm{mJ\,cm^{-2}}$ is applied corresponding to small temperature changes of about 20 K, which is limited by the damage threshold of sample 3. Furthermore, favored by the symmetry that has been identified by measuring the full rotation (see Fig. 6.1.2), it is sufficient to narrow down the range of external field angles to $0° - 90°$ (from out-of-plane to in-plane), as the signal is repeated for higher angles. In contrast to the previous MOKE experiment, the measurements here are not performed in a way that eliminates the non-magnetic contributions, as it is typically done in MOKE measurements. A 180°-rotation of the magnet takes much longer compared to switching of the magnetic field by an electro-magnet, so it is foregone for time reasons. This is viable for a qualitative comparison of the characteristics of the measurement signal, since the strong oscillations on picosecond timescales are unambiguously of magnetic origin. Furthermore, the background is also dominated by a magnetic contribution, as can be seen from the sign change of the step-like signal in the full rotation for opposite magnetic field directions (see Fig. 6.1.2b). Temperature- and strain-induced reflectivity changes contribute via an offset to the absolute signal amplitude, which is constant for each transient and therefore does not change the angle-dependence qualitatively.

Figure 6.2.1 displays 2D-colorplots of the measured MOKE signal as a function of time and external field angle corresponding to sample 1 (a, Pt-Cu-Ni), sample 2 (b, Pt-Cu-MgO-Ni), and sample 3 (c, Pt-MgO-Cu-Ni) as well as colorplots of the corresponding FFT spectra as a function of frequency and field angle (d-f). All data sets exhibit oscillations of the M_z-component of the magnetization resulting from the coherent precessional motion of the magnetic moments. As expected, the data shows coincident oscillation frequencies ranging from 5 GHz to 20 GHz for all samples, however, sample-specific angular dependencies of the precession amplitudes can be observed. In sample 1, both time-resolved MOKE data and the corresponding FFT spectra indicate pronounced oscillations attributed to magnetization precession, which occur for external field angles between 0° and 80°. Only at higher angles, they cannot be identified due to a drastically decreased excitation that will be discussed below. A maximum in precession amplitude occurs at about 47°, but also towards smaller field angles strong oscillations can be observed (see Fig. 6.2.1a, d), which is clearly different for the remaining samples 2 and 3 (see Fig. 6.2.1e, f), as for both heterostructures with the integrated MgO layer only one maximum at intermediate field angles can be seen. Furthermore, in sample 3, the oscillations are significantly weaker compared to sample 1 and 2, so they can be barely identified for very small as well as very large angles. For a direct comparison of all sample structures, figure 6.2.1 shows also two illustrative examples of the time-resolved MOKE data measured at $\phi = 43°$ (g) and $\phi = 0°$ (i). Both sample 1-transients (red lines) exhibit particularly strong oscillations, while high amplitudes can be observed only for higher angles in the samples with MgO (blue, yellow line).
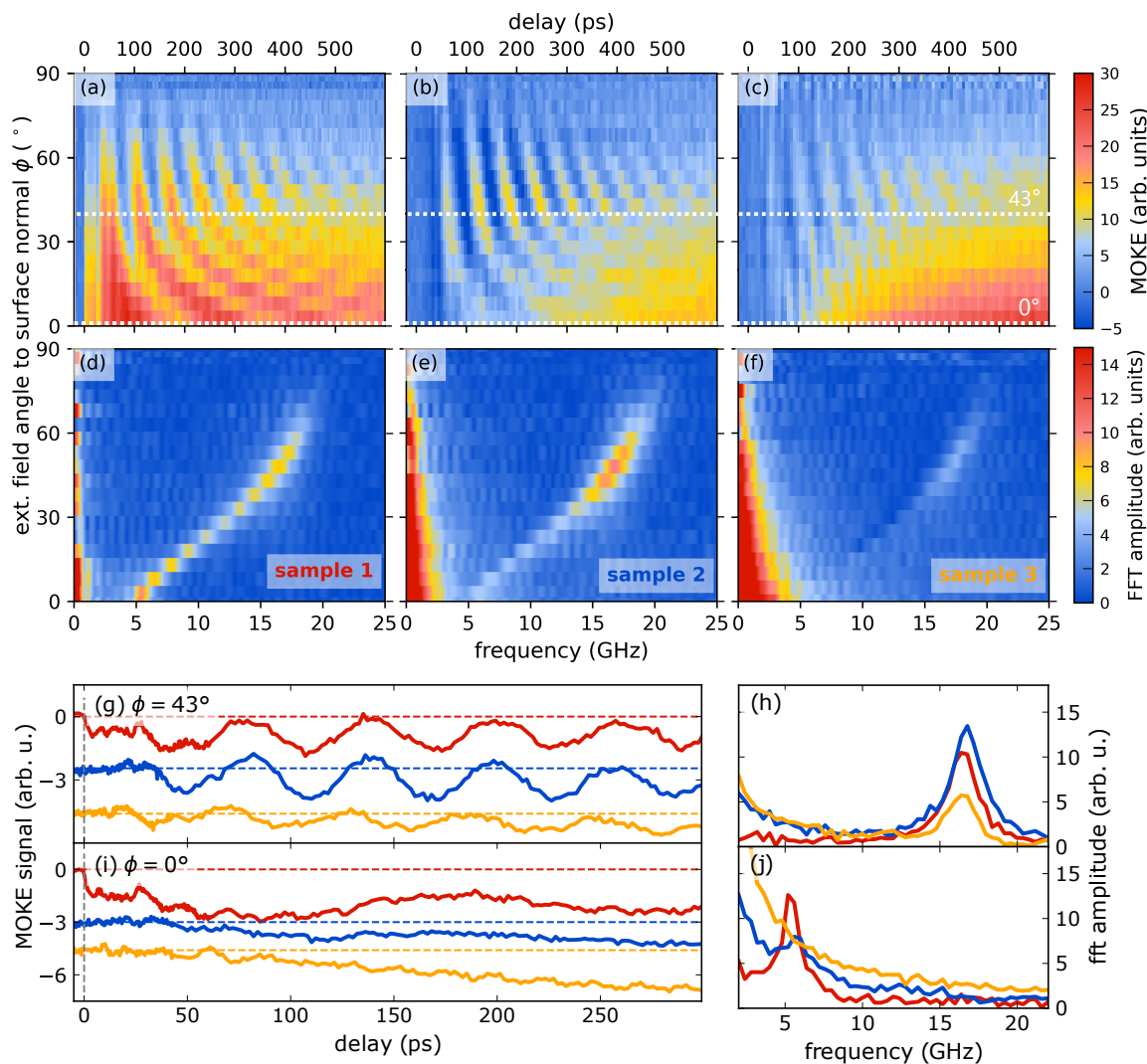
Figure 6.2.1: Sample-dependent magnetization precession: (a)-(c) The MOKE-signal of all samples is depicted as a function of time and external field angle between $0° - 90°$. Pronounced oscillations of the magnetization can be observed in all heterostructures attributed to magnetization precession driven by different mechanisms. Each sample exhibits a distinct angular-dependence of frequency, amplitude, and damping parameter, which can be extracted easily from the FFT spectra, that are depicted in panels (d)-(f) as a function of frequency and external field angle. (g),(i) Representative MOKE-transients measured at $\phi = 43°$ and $\phi = 0°$ (see dotted lines in (a)-(c)) allow for a direct comparison of the excited spin waves in each sample. In contrast to the precession frequencies the spin wave amplitudes are highly sample-dependent, which is illustrated by the FFT-spectra in panels (h), (j).

A more condensed view on the angular dependence of the precession frequencies and amplitudes is given in figure 6.2.2a and b, which summarizes the main characteristics of the measurement signal for all heterostructures. By fitting the FFT-signal for each external field direction (see Fig. 6.2.1h, j) considering a Gaussian function on a background, which correspond to the oscillation peak and to different components of the signal, respectively, the frequency and amplitude of each precession are determined. In order to identify the origin of the precessional motion, it is useful to consider the known temperature and strain dynamics of the individual heterostructures (see Fig. 6.2.2c). As already discussed in chapter 4, temperature and lattice dynamics in nickel change significantly depending on the position of the inserted MgO film, which has been shown unambiguously by UXRD measurements and simulations. The insulating layer prevents an ultrafast energy deposition into the metal films below, resulting in an increasingly simplified temperature

and strain response in nickel the less metals are excited. Accordingly, the strain response in sample 3 (Pt-MgO-Cu-Ni) is comparably simple, since energy is deposited only in Pt. The Pt layer expands very rapidly and generates a very short bipolar strain pulse with a pulse duration of $\tau_{Pt} = 2d_{Pt}/v_{S,\,Pt}$ arriving after $t \approx 25\,\text{ps}$ in the nickel layer (see. Fig. 6.2.2c). By comparing the temporal evolution of lattice dynamics and MOKE signal, one finds that magnetization precession starts with the arrival of the short strain pulse (see Fig. 6.2.1g). Since heat diffusion through MgO occurs on significantly longer timescales and therefore cannot contribute to the excitation, it is clearly the propagating strain pulse that drives magnetization precession in sample 3.

Similarly in sample 2 (Pt-Cu-MgO-Ni): the MgO layer prevents a direct temperature increase in the buried ferromagnetic film but not in Cu, which is also excited by the ultrashort laser pulse, causing a modified lattice response in nickel at early delays in particular. Instead of a single strain pulse originating from Pt, a significantly longer strain pulse is generated in the adjacent Cu layer in addition to the short bipolar strain wave excited in Pt. The long bipolar strain pulse propagates almost instantaneously into the nickel film and deflects the magnetization directly after the laser absorption at $t \approx 0\,\text{ps}$, resulting in comparably high spin wave amplitudes (see Fig. 6.2.1g).
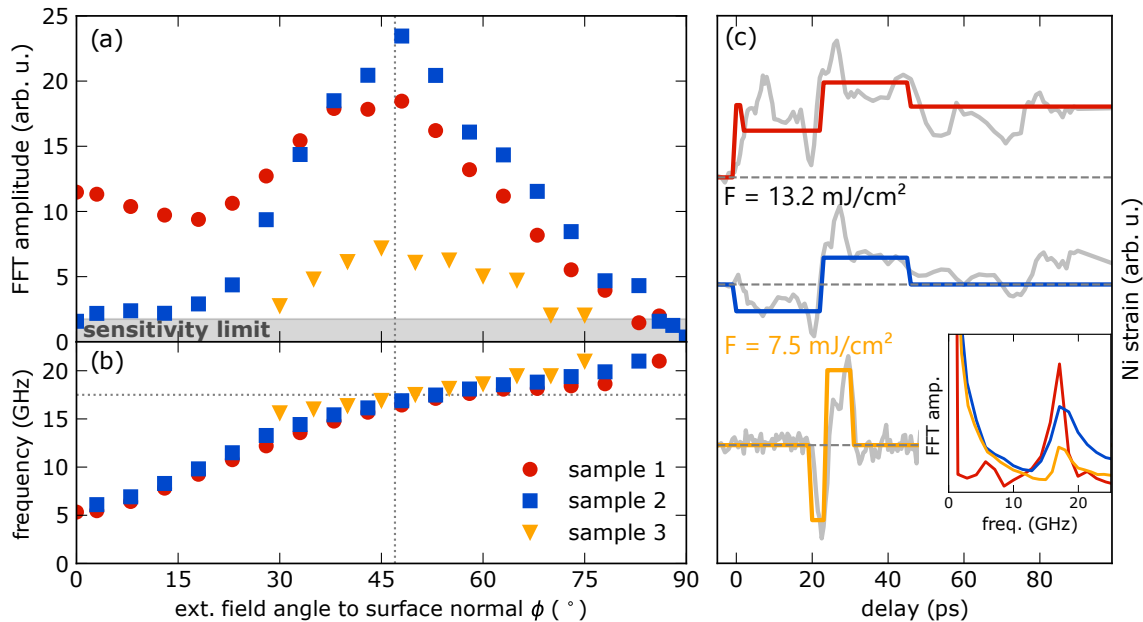
Figure 6.2.2: Distinguishing the excitation mechanism of magnetization precession: The extracted oscillation amplitudes (a) and frequencies (b) are depicted as a function of the external field-angle. While the frequency is independent of the driving mechanism, the amplitudes exhibit a clear sample-dependence, which is attributed to the corresponding temperature and strain dynamics. (c) The specific excitation mechanism is schematically displayed for each sample, which can be identified from the time-resolved strain. Since only strain waves enter Ni within the first 100 ps, they have to be the origin of magnetization precession in sample 2 and 3, where the longer but weaker strain pulse in sample 2 is much more efficient compared to the short bipolar pulse originating from Pt. At 17.5 GHz, the circulation frequency of these recurring strain waves (see inset in (c)), the spin waves are amplified resonantly due to the strain pulse propagation (gray dashed lines), explaining the high amplitudes at 47°. Heat additionally contributes via a step-like change in the effective field due to quasi-static strain and demagnetization, which must be the origin of large precession amplitudes around 0° according to the exclusion principle.

Compared to the previous samples, it is not straightforward to identify the dominating excitation mechanisms of magnetization precession in the first sample (Pt-Cu-Ni) due to the missing MgO film leading to a direct energy deposition into all metallic layers (see Chap. 4.1). The resulting fast temperature rise in nickel has several consequences, as it is accompanied by a rapid thermal expansion, i.e., positive strain affecting the effective field, as well as an ultrafast demagnetization

modifying the shape anisotropy of the film. Thus, two additional thermally induced effects play a role in sample 1, which are summarized as thermal mechanism at this early stage of the analysis, since both effects simultaneously provide mainly constant contributions to the effective field arising at $t \approx 0$. To complete the terminology, the effective field changes corresponding to the propagating strain waves generated in Pt, Cu, and Ni are referred to as strain-induced mechanism, even though it does not include quasi-static strain, which is covered by the thermal mechanism. Magneto-crystalline anisotropy is not considered due to its minor role in nickel.

As discussed, the angular dependence of the precession parameters depicted in figure 6.2.2 indicates in addition to a maximum at $47°$, also high amplitudes at $0°$. The direct comparison of the angle-dependent amplitudes in sample 1 and the samples with MgO suggests the strain mechanism as driving force at larger angles generating the precessions of high amplitudes at $47°$. By implication, the maximum at $0°$ must correspond to the sudden temperature rise in nickel.

To summarize at the half-way mark, the measurements show that propagating strain pulses of bipolar shape are able to induce magnetization precession occurring in all three heterostructures, which is in agreement with previous studies demonstrating this effect [10, 28]. This transient magneto-elastic field is the main driving mechanism of the observed oscillating Kerr-signal corresponding to the samples including MgO (sample 2 and 3) and is the most efficient at an angle of $47°$, as indicated by oscillations with the largest amplitudes there (see Fig. 6.2.2a). In sample 1 (Pt-Cu-Ni), the strain-induced effective field changes are accompanied by heat-induced contributions, that include demagnetization and quasi-static strain due to thermal expansion. This rapid change directly after laser excitation causes high amplitude precessions at smaller angles (see red symbols in Fig. 6.2.2a).

In conclusion, the analysis of the angle-dependent amplitudes complemented by the information from the UXRD measurements allows for assigning the dominating excitation mechanism for magnetization precession, however, the question remains as to the origin of the specific characteristics, especially since both the thermal and strain effect seem to act very similarly, causing only changes in the z-component of the effective field (see Eq. 2.3.13).

6.3 Explaining the field angle-dependence of the driving mechanisms

The observation of strong magnetization precession for external field orientations close to a magnetic hard-axis of the investigated material has been already shown by other studies in literature [25, 54, 74, 77]. In the presented case, this generally occurring effect can be explained by the relative change of the effective field $\Delta H_{\text{eff}}/|H_{\text{eff}}|$, which is largest at $\phi = 0°$, which means a comparably large deflection of the effective field from its equilibrium orientation. With increasing external field angle, however, this relative change of $\vec{H}_{\text{eff}}$ decreases due to the increasing absolute value of $\vec{H}_{\text{eff}}$, which is additionally enhanced by a decreasing m_z-component of the magnetization determining ΔH_{eff} via the shape anisotropy as well as the magneto-elastic field (see Eq. 2.3.13). Hence, provided that the external field strength is below the saturation field and that the effective field change is fast compared to the magnetization precession, the largest torque acting on the magnetization can be expected at $\phi = 0°$.

The observed ultrafast demagnetization and rapid thermal expansion in sample 1 cause such a required fast change of $\vec{H}_{\text{eff}}$ explaining the high oscillation amplitudes at small angles. Although short bipolar strain pulses, such as in sample 3 (Pt-MgO-Cu-Ni), also fulfill these conditions mentioned above, the observed angular dependence of the amplitude does not display the expected behavior of strongest oscillations towards small external field angles. Instead, a maximum at about $47°$ arises, whereas precession are barely detected for an out-of-plane magnetic field orientation. The decisive difference between the thermal and the strain mechanism is the recurring character of the propagating strain pulses due to its reflection at the sample surface and the metal-glass interface. During propagation, it changes the effective field repeatedly, where the relative change of $\vec{H}_{\text{eff}}$, i.e., the excitation strength, per round, is indeed still larger at small

angles: $\Delta H_{\text{eff}}/|H_{\text{eff}}|\,(0°) > H_{\text{eff}}/|H_{\text{eff}}|\,(47°)$. The crucial factor here is given by the relative phase of the propagating strain pulse and the precession. Magnetization precession is amplified when the repetition rate of the strain pulse coincides with the precession frequency, which applies at an external field angle of 47°. The FFT-amplitude of the simulated lattice strain of nickel indicates an orbital frequency of the strain pulses within the metal stack of about 17.5 GHz, which is true for all presented heterostructures due to their similar thicknesses (see inset Fig. 6.2.2c). Since the precession frequency reaches 17.5 GHz at 47° under the chosen experimental configuration, it is resonantly amplified during strain wave propagation, resulting in maximum amplitudes for this magnetic field direction.
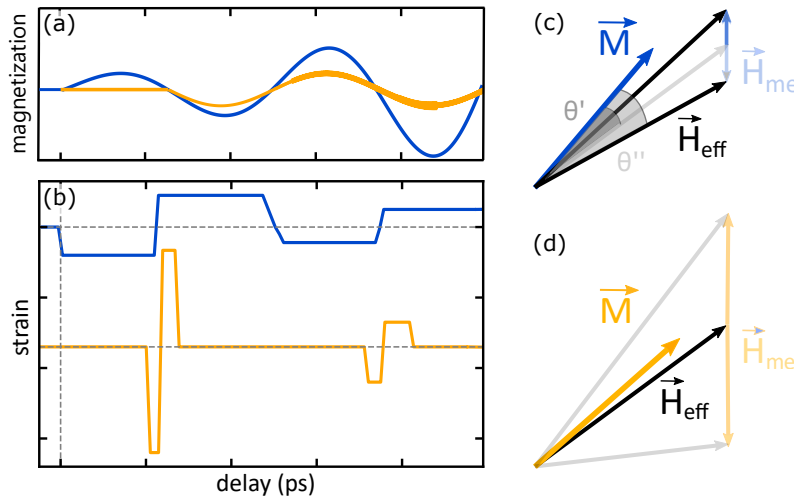

Figure 6.3.1: Magnetization precession driven by coherent strain: The amplitude of the precession driven by differently shaped strain pulses are compared in panel (a). The corresponding strain waves are schematically depicted in panel (b). The precession amplitude is further amplified by propagation of the long strain wave with each change of sign of η in Ni (blue). The effective field is deflected each time to the opposite direction, resulting in an increasing angle θ between the magnetization and the effective field inducing a larger torque (c). Since $\vec{H}_{\text{eff}} \propto -\eta$, the precession is phase shifted by π with respect to the strain. The transient magneto-elastic field originating from the short acoustic pulse (yellow) can be considered as a small deflection of the magnetization at constant intervals, resulting in weak amplification (d).

Furthermore, we can conclude from the difference in amplitude between sample 2 and 3 that the long bipolar strain pulse originating from copper is significantly more efficient than the short strain wave resulting from the Pt expansion, even though the strain wave amplitude of the short pulse is substantially larger. The pulse duration τ_{Cu} determined by the film thickness corresponds to the period of the oscillation of the magnetic moments $\tau_{\text{Cu}} \approx T_{\text{prec}} = 2\pi/\omega_{\text{prec}}$ at $\phi = 47°$, which is highly beneficial in terms of magnetization precession, since the change $\vec{H}_{\text{eff}}$ is in phase with the motion of the spins. The average strain switches from compression to expansion exactly when the magnetization is maximally deflected and has reached its reversal point with respect to the z-direction. Accordingly, the effective field is deflected away from the magnetization, again maximizing the resulting torque. On the contrary, the short pulse is considered only as a small perturbation determined by a small asymmetry between the expansive and compressive strain pulse components, which briefly pushes $\vec{M}$ once in each round-trip similar to pushing a swing. Figure 6.3.1 contrast these two processes schematically.

In summary, the angular dependence of the precession amplitude provides the following key observations so far: Beyond the frequency interval near resonance, the thermal mechanism is substantially more efficient compared to the strain effect, which is evident by comparing of the initial precession amplitudes in all heterostructures at an angle of 0° depicted in figure 6.2.1g.

However, due to their recurring character, short bipolar strain pulses are also able to induce magnetization precession with comparable amplitudes by amplification, as highlighted by sample 3. Strain-induced precession amplitudes even exceed thermally induced oscillations as soon as the pulse duration matches the precession period, which is evident from the high precession amplitudes around 47° corresponding to sample 2 (see Fig. 6.2.2a). By examining the precession phase, which also depends on the driving effect, one finds that resonant excitation (here: by the long strain pulse) is the most efficient of all mechanisms, as will be discussed next.
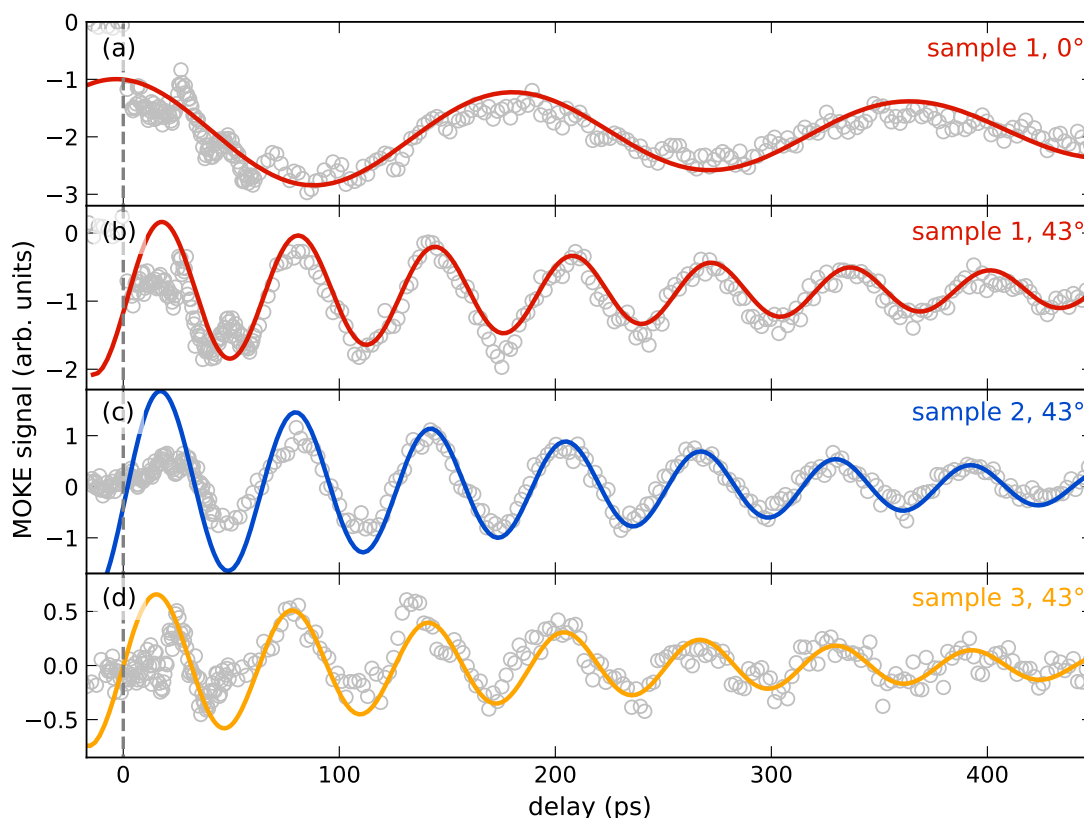
Figure 6.3.2: Angle-dependence of the precession phase: Exemplary MOKE transients (gray symbols) are fitted by a decaying sine oscillation (see Eq. 6.3.1) in order to extract the precession phase, that is determined by the respective driving mechanism. (a) In sample 1, spin waves of large amplitudes are induced by the thermal mechanism at $0°$ indicated by an initial phase of $\delta_0 = \pi/2$. (b) In contrast, it is the long bipolar strain wave originating from Cu that dominates the excitation of magnetization precession around $43°$, resulting in a sine-like oscillation of the M_z-component. (c) This is confirmed by the magnetization precession in sample 2, which is clearly driven by the long strain wave. The coincident phase of the two oscillations (b, c), shows that the resonant acoustic pulse dominates at this angle in both samples. (d) The precession phase of $\delta_0 = \pi$ in sample 3 corresponds to the impulsive excitation via the short strain pulse entering into nickel after 25 ps. To obtain a better fit of the MOKE signal, the thermal background was subtracted in sample 2, 3.

In order to analyze the phase resulting from the excitation by different effects, figure 6.3.2 illustrates exemplary transients attributed to the specific excitation mechanism, which has been identified for each sample before. The MOKE-signal corresponding to sample 1 is compared for external field angles of $0°$ and $43°$ (gray symbols), where spin waves are driven by heat and propagating strain, respectively. By fitting the oscillating Kerr rotation using equation 6.3.1, the precession phase is extracted (red lines). The model considers a sine-oscillation with corresponding frequency ω and phase δ_0, taking into account an exponential decay describing the damping with

a time constant τ:

$$f(t) = A_0 \cdot \sin(\omega t + \delta_0) \cdot e^{-t/\tau} + m \cdot t - f_0. \tag{6.3.1}$$

A linearly increasing background described by a slope m and an intercept f_0 accounts for the slow cooling to the substrate in sample 1. It is worth to mention that considering a superposition of two oscillating components would yield a more realistic description of the excitation process involving both driving mechanisms. However, in each case, the less relevant effect introduces only a tiny phase shift resulting from the different phases and the different amplitude ratio. This minor difference can be hardly fitted. Consequently, this phase shift is neglected within the fitting.

At $0°$ in sample 1, a phase of $\delta_0 \approx \pi/2$ is extracted (see Fig. 6.3.2a), which confirms the temperature-induced change of the effective field to be the dominant excitation mechanism for this geometry, corresponding to a displacing excitation. This kind of excitation is assigned to a step-like modification of the effective field that changes its orientation persistently, resulting in a precessional relaxation of the magnetization towards this new equilibrium ($\delta_0 = \pm \pi/2$). The temperature rise in Ni in sample 1 (Pt-Cu-Ni) induces such an effective field change composed of a magneto-elastic field and a reduction of the shape anisotropy due to the long-lasting quasi-static strain and demagnetization, respectively (see Chap. 4 and 5). The ultrafast component of the demagnetization within the first picosecond can be ruled out to play a considerable role in terms of driving magnetization precession, provided that it is as weak as in this experiment. Such a short-lived change of the effective field, which is similar to the modulation by the short strain pulse, can be also considered simply as a fast deflection of the magnetization, while the effective field does not change. Like a pendulum which starts to swing after of a short push, the magnetization precesses around the equilibrium orientation of $\vec{H}_{\text{eff}}$. Such an excitation induces a sine-oscillation of the m_z-component with a corresponding phase $\delta_0 = 0$ and is referred to as impulsive excitation. Considering the spin wave at $43°$ reveals a phase-shift of the oscillation compared to the transient MOKE signal at $0°$, indicating a change of the dominant excitation mechanism (see. Fig.6.3.2b). The observed Kerr-signal modulation is perfectly in phase with the precession in sample 2 at this angle, which is depicted in panel (c) of figure 6.3.2, highlighting the same dominating driving mechanism, namely the long bipolar strain wave originating from Cu. Both oscillations exhibit a phase of $\delta_0 \approx 0$, which, however, is not attributed to an impulsive excitation. In contrast to a short bipolar strain pulse, the long sound wave does not represent an impulsive mechanism, since the corresponding change of the effective field is not short-lived regarding the spins kinetics (see Fig. 6.3.1b). Instead, the expression displacing excitation with changing sign fits better, which corresponds to a very efficient way to excite spin waves. The phase shift in sample 1 at $43°$ even shows that resonant excitation is even more efficient than the thermal mechanism, which is usually considered as the most important effect.

For completeness of this phase analysis, the strain pulse originating from Pt, triggering magnetization precession in sample 3, leads to an impulsive excitation. Accordingly, a sine-like oscillation is observed (see Fig. 6.3.2d), however, with a phase difference of π with respect to the precession induced by the long strain wave. Due to the dominant expansive component of the short strain pulse, the effective field change is determined by a positive strain contribution $\Delta H_{\text{eff}} \propto -\int \eta \, dt$, while a compression, i.e., negative strain, initiates magnetization precession considering the long strain pulse (compare Fig. 6.2.2c). Due to the delayed arrival of the short strain pulse in nickel after $t \approx T_{\text{prec}}/2 \approx 25\,\text{ps}$, which coincides with the sign change of the long strain wave, the oscillating MOKE-signal is nevertheless in phase at $43°$ for all heterostructures (compare Fig. 6.2.1h).

The slow change of $\vec{H}_{\text{eff}}$ by the long strain pulse in sample 2 enables determining the sign of the magneto-elastic coupling constant b from the initial sign of the magnetization change induced by the compressive strain. During the propagation of the preceding compressive part in nickel, the MOKE data displays an increase of the m_z-component, which corresponds to a deflection of the magnetization towards the external magnetic field with $\Delta \vec{H}_{\text{eff}} > 0$. As soon as the

following expansion enters nickel (at about 25 ps), the change of m_z switches its sign, which leads us to the conclusion that the magneto-elastic field counteracts the external field, which implies $b < 0$ considering a positive strain.

Based on this knowledge, also the major contribution to the thermal mechanism can be distinguished, i.e., thermal expansion or demagnetization due to the temperature increase. Figure 6.3.3 illustrates both counteracting effects and the resulting MOKE signals. Demagnetization is accompanied by a decrease of the shape anisotropy assigned to the demagnetization field, which is mainly governed by the m_z-component of the magnetization (compare Eq. 2.3.13). As a consequence, the effective field is deflected towards the external field direction, resulting in a magnetization precession with positive magnetization change neglecting the initial drop due to demagnetization (see Fig. 6.3.3a and b). In contrast, an expansion of the lattice, positive strain, induces an additional negative effective field contribution, which deflects $\vec{H}_{\text{eff}}$ away from the magnetic field. The resulting torque acts to the opposite direction and triggers a spin wave phase-shifted by π with respect to the demagnetization-induced oscillation. Comparing the sketched MOKE signal to the data clearly reveals that strain is dominating the thermal mechanism, since a cosine precession is observed. This means in summary that magnetization precession is governed by the strain response, and other possible effects play only minor roles in our experiments.
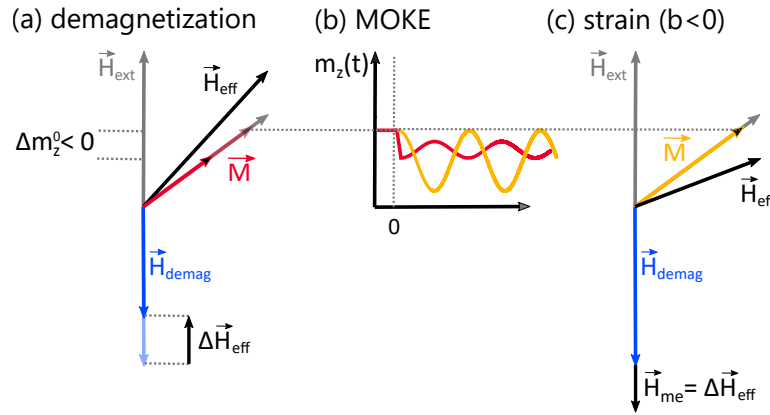

Figure 6.3.3: Temperature-induced effective field changes: (a) Demagnetization decreases the demagnetization field $\vec{H}_{\text{demag}}$ acting against the external magnetic field $\vec{H}_{\text{ext}}$. As a result, the effective field $\vec{H}_{\text{eff}}$ is tilted towards the external field according to the positive effective field change $\Delta\vec{H}_{\text{eff}}$. (b) The temporal evolution of the m_z-component of the magnetization displays, in addition to an decrease of the magnetization magnitude, a precessional motion in positive direction (red line). In contrast, a negative change of the effective field results in a oscillating signal of opposite phase (orange line). (c) Thermal expansion causing positive quasistatic strain induces such an precession due to the negative magneto-elastic field $\vec{H}_{\text{me}}$.

6.4 Modeling of magnetization precession

Finally, I try to estimate the actual importance of the lattice dynamics for the excitation of the precessions by modeling of the magnetization response on the basis of the Landau-Lifshitz-Gilbert equation (see Eq. 2.3.12) using a macrospin approximation. In accordance with other proposed models, the considered effective field 2.3.13 corresponding to the 20 nm nickel film comprises a demagnetization field related to the shape anisotropy, a Zeeman-field, as well as a magneto-elastic coupling term [123, 124]. The free energy is given by:

$$F_{\text{M}}(\vec{m},t) = -(\vec{m} \cdot \mu_0 \vec{H}_{\text{ext}}) + \frac{\mu_0 M_{\text{sat}}}{2} m_z^2$$
$$+ \frac{2b\eta(t)}{M_{\text{sat}}} m_z^2. \tag{6.4.1}$$

By measuring the in- and out-of-plane hystereses in SQUID and static MOKE measurements (see Chap. 3.2), the demagnetization field of $\mu_0 H_{\text{demag}} = 620\,\text{mT}$ was determined. The external field was adjusted with respect to the measured frequencies. The assumed absolute value of $\mu_0 H_{\text{ext}} = 450\,\text{mT}$ is still reasonable regarding the uncertainty of the distance-dependent magnetic field of the permanent magnet. Possible stray field contributions resulting from the setup at the probing spot are neglected in the model, since their influence on the precession frequencies is largely insignificant except for angles close to $\phi = 0°$. Furthermore, a magneto-elastic coupling constant of $b = -7.85 \cdot 10^6\,\text{J m}^{-3}$ is assumed. The input time-dependent strain $\eta(t)$ is taken from the UXRD-simulation, which was calculated in advance for an adjusted simulation fluence. For simplicity, only the magneto-elastic field is time-dependent within the modeling, while the magnetization is assumed to be constant, which is rationalized by the observation that the magnetization precession is mainly determined by the strain response.
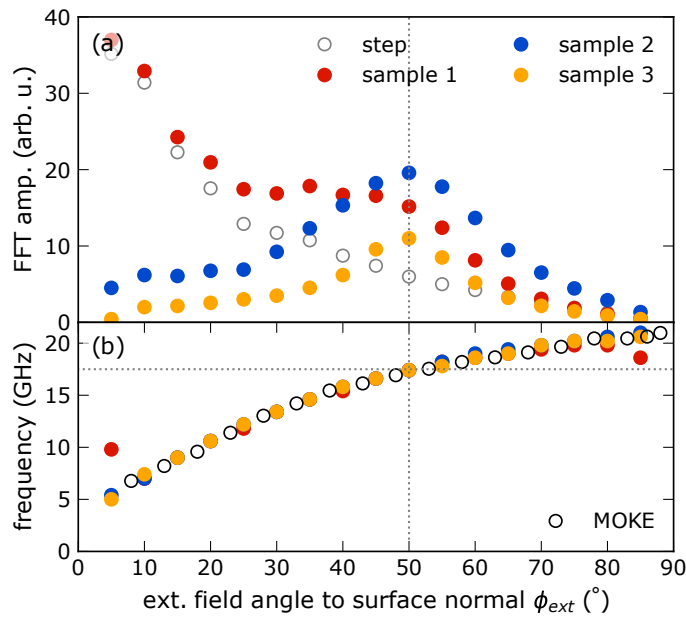

Figure 6.4.1: Theoretical analysis of magnetization precession driven by strain: Analogously to figure 6.2.2, the simulated precession amplitude (a) and frequency (b) are depicted as a function of the external field angle. A good qualitative agreement between measured data and simulation is obtained by considering only the simulated strain as driving mechanism in all samples. As indicated by the dashed lines, propagating strain yields maximum amplitudes at intermediate angles. Deviations around $0°$ in sample 1 can be attributed to the neglected demagnetization, which counteracts the magneto-elastic field from thermal expansion. This is underlined by the gray empty circles in panel (a), which correspond to the analysis of the angle-dependence of magnetization precession driven by the exact quasi-static strain step as in sample 1, neglecting coherent strain contributions.

The characteristics of the simulated magnetization precession in the investigated heterostructures (sample 1-3) are summarized in figure 6.2.2a and b. The simulated time-resolved magnetization transients are analyzed analogously to the measured data. The frequency and amplitude are extracted from the Fourier-spectra of the time-dependent m_z-component for varying external field angles. Panel (b) shows the calculated precession frequencies (colored symbols) for all heterostructures compared to a set of representative frequencies from measurements (black circles), which are in excellent agreement under the chosen effective field parameters. The identical simulated frequencies confirm once again that the observed magnetization precession at weak excitation is mainly determined by the equilibrium parameters. Only amplitude and phase depend on the specific excitation mechanism.

In addition, a good qualitative agreement with respect to the measurements is also obtained for

the angle-dependent precession amplitudes. In sample 2 and 3 with the integrated MgO (blue and orange symbols), the modeled angular dependence of the amplitudes reproduces very well the observations from the experiment. At an external field angle of $\phi = 50°$, which is slightly shifted with respect to the experimental resonance due to the uncertainty of the angle in the measurement, the precession frequency coincides with the repetition rate of the propagating strain pulses, which is indicated by a horizontal dashed line at 17.5 GHz. The excited precession is enhanced resonantly for several times, resulting in maximum amplitudes in sample 2 and 3. Furthermore, the oscillation amplitudes are significantly stronger in sample 2 compared to sample 3 due to the fact that the precession is not only resonantly amplified but also resonantly driven by the long bipolar strain pulse (compare Chap. 6.3).
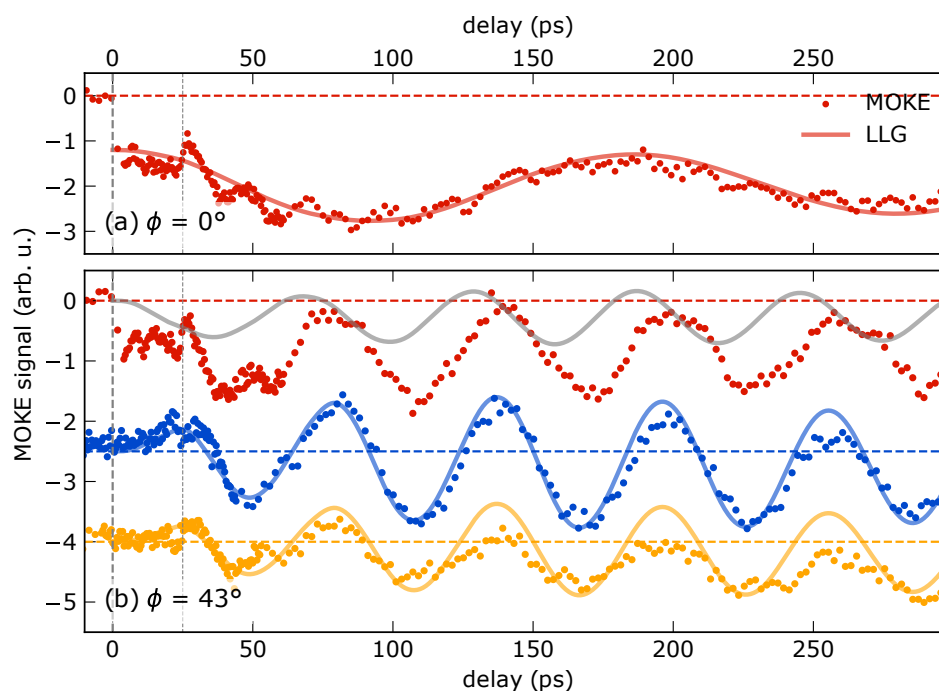
Figure 6.4.2: Time-resolved LLG results: The simulated changes of m_z are compared to the measured data. (a) At $\phi = 0°$, only the spin wave in sample 1 exhibits a significant amplitude. The simulated transient is shifted to negative values accounting for the initial demagnetization, which is not included in the model. (b) At $\phi = 43°$, the LLG simulation provides very good results for samples 2 and 3 (blue, orange). In sample 1 the simulated signal deviates strongly from the MOKE data (gray line). This is due to the neglected demagnetization in the model, that partially compensates the thermal expansion so that the long bipolar strain pulse predominantly drives the magnetization precession.

Considering sample 1 next, the simulation results also confirm that magnetization precession is predominantly determined the time-dependent strain response, although some differences in the angular dependence of the amplitude between simulation and measurement can be seen (red symbols). As in the experiment, particularly high precession amplitudes occur around $0°$ and $47°$, the ratio of the corresponding simulated maxima, however, deviates clearly from the observations. While the amplitudes attributed to the propagating strain-pulses exhibit comparable values to the amplitudes in sample 2, the increase towards small external field angles is heavily overestimated compared to the MOKE-signal (compare Fig. 6.2.2 and 6.4.1). To get a better understanding of this deviation, the angular dependence of magnetization precession induced by a purely step-like strain profile is considered additionally. The resulting amplitudes for a strain-level of $\eta = 0.6 \cdot 10^{-3}$ for $t > 0$ corresponding to the thermal expansion observed in sample 1 are illustrated by empty circles in figure 6.4.1a. The spin wave amplitudes induced by this strain-step are decreasing with increasing external field angle. Taking this into account, the calculated response in sample 1 can

be clearly assigned to an excitation by the superposition of this step-like quasi-static strain and the propagating strain waves. In the experiment, however, the rapid demagnetization counteracts the fast thermal expansion, resulting in an effectively smaller change of the effective field and thus smaller precession amplitudes than in the model (see Fig. 6.3.3).

The role of demagnetization is also reflected by the time-domain LLG-results. Figure 6.4.2 displays examples of calculated transients $\Delta m_z(t)$ at the characteristic angles. By scaling $\Delta m_z(t)$ at $\phi = 0°$ with respect to the measured amplitude, a very good agreement of calculated and observed precession can be obtained (see Fig. 6.4.2a). Accounting for the step-like demagnetization, the simulated transient is shifted vertically, since it is not included in the model. In contrast, scaling the modeled MOKE-transient at $43°$ by the same factor yields a significantly smaller precession amplitude as well as a different phase compared to the measurement (see gray line in Fig. 6.4.2b). Due to the neglected compensating effect of the demagnetization, which reduces the effective field change attributed to thermal expansion, the displacing excitation remains dominant, while the strain wave induces a slight phase shift in the modeling only.

In contrast, the modeled precession in samples 2 and 3 agrees excellently with the measurements, since only lattice dynamics actually play a role in exciting the precession here. The increasing divergence of the transients towards large delays is also assigned to demagnetization due to the slow heat diffusion into nickel slowly reducing the absolute value of the magnetization, which however does not affect the driven precession.

Conclusion

In this thesis I studied the response of the magnetic system of a buried ferromagnetic nickel layer to ultrafast laser excitation of a metallic heterostructure. I analyzed the influence of varied temperature and strain dynamics on two major aspects of magnetization dynamics, i.e., ultrafast demagnetization and magnetization precession, by combining time-resolved MOKE experiments with ultrafast x-ray diffraction. By modeling the measured strain response, I obtained a comprehensive picture of the lattice and temperature dynamics, that are strongly correlated to the spin dynamics. This calibration enabled a quantitative examination of modeling approaches for magnetization dynamics taking into account the remaining subsystems, which is mostly neglected in other works.

The investigated sample structure Pt(7 nm)-Cu(95 nm)-Ni(20 nm) is characterized by an ultrafast energy transport by hot electrons into the buried magnetic film [51]. In addition to this sample, two variants of this heterostructure were focused with an integrated MgO-layer, which modifies the energy exchange of the total system and therefore temperature and strain dynamics, as demonstrated via UXRD. Modeling the quantitatively determined strain response of all layers within the framework of a diffusive 2TM utilizing a single set of parameters yielded the spatio-temporal energy transfer processes within the heterostructures. The very good agreement of the measured data and the simulated lattice dynamics demonstrates the great reliability of the modeling.

While ultrafast demagnetization is known for almost three decades, the fundamental processes related to this phenomenon are still under debate. The m3TM is a commonly applied model to describe demagnetization in ferromagnets, however, under the assumptions of strongly adjusted material parameters, such as the phonon heat capacity, which do not agree with known values determined in independent experiments. Here, I used the temperature dynamics calibrated by UXRD and the transient magnetization detected by tr-MOKE in order to test the m3TM for two limiting cases of ultrafast excitation in Pt-Cu-Ni and slow heating in Pt-Cu-MgO-Ni, taking into account all subsystem involved in the model. The analysis demonstrated that transient magnetization is well captured by the m3TM in thermal equilibrium, ultrafast demagnetization, however, was severely overestimated directly after excitation. An improvement requires a faster transfer of deposited energy from electrons to phonons, which is not captured by the 2TM. Taking into account other studies showing a long-lasting internal non-equilibrium of the phonons, e.g., for a few ps in Ni [120, 121], the presented analysis has suggested that in contrast to lattice dynamics ultrafast demagnetization is sensitive to this initial non-equilibrium. Consequently, a description of this process by assuming a single phonon temperature is not adequate.

In the second main part of this thesis, I compared different excitation mechanisms for magnetization precession for small temperature changes of about 20 K in nickel. Essentially, two effects were considered, namely excitation by propagating strain pulses and nonrecurring step-like excitation due to a rapid temperature rise, resulting in a change of the shape anisotropy as well as an appearance of a magneto-elastic field. Varying the orientation of the external field, which effectively resulted in a tuning of the precession frequency, I investigated systematically the precession amplitude as a function of the external field angle in the Pt-Cu-Ni heterostructures, which has been tailored

specifically in order to separate the driving mechanisms, as confirmed by the strain characterization via UXRD. I identified two main excitation characteristics: Resonant excitation by a strain wave, which is resonant to the precession in terms of both pulse duration and round-trip time, is by far the most efficient to drive magnetization precession. Off-resonance, the efficiency of the strain pulses decreases significantly and the spin wave excitation is governed by step-like changes of the effective field resulting from rapidly heating the ferromagnet. Furthermore, careful analysis of the initial precession phase showed that the contribution of the magneto-elastic field to the effective field, that is attributed to the arising quasi-static strain, outweighs the change in shape anisotropy due to demagnetization when small temperature changes are considered. These results, in particular the crucial role of lattice dynamics in nickel, were confirmed by both experiment and modeling based on the LLG equation taking into account the simulated average strain.

The well-founded results of both experimental parts show the tremendous potential of combining MOKE and UXRD in the interpretation of magnetization dynamics, especially on the picosecond timescale. The reliability of the UXRD modeling of the Pt-Cu-Ni-heterostructures also makes it possible to study other example cases and test hypotheses without the urgent need for experiments.

Due to the direct involvement of the spin system in the energy exchange after ultrafast excitation, ferromagnetic materials are well suited as sensors for microscopic interactions. However, for application in experiments, a reliable theoretical description of laser-induced magnetization dynamics is necessary, which, as shown for the example of the m3TM, still requires some efforts. Furthermore, studies of simpler sample systems, such as homogeneously probed thin films to rule out non-local effects, for example, would be advantageous in terms of further evaluating the m3TM. Most importantly, to make real progress in this field, it is crucial to take into account all involved subsystems when comparing models and experiments.

The presented analysis of magnetization precession offers a variety of starting points for further experiments. One example is to extend the investigation of resonant excitation to other materials exhibiting larger magnetostriction than Ni, such as Galfenol. It would be also much more interesting to look at the effect of temperature-dependent magneto-crystalline anisotropy in comparison to the other mechanisms, which does not play a role in nickel. Cobalt, for example, could be a suitable material, since it has very similar properties to nickel and exhibits additionally anisotropy. Demagnetization is supposed to be even less pronounced for comparable excitation due to the higher Curie temperature, which can be beneficial in terms of strain-induced precession. At the same time spin waves of higher frequencies can be excited [26, 27], which expands the scope regarding resonant excitation and excitation strength, which is mainly determined by the Cu thickness. However, due to the large saturation field in Co, a stronger magnet would be useful to be able to excite the high frequency magnetization precession as well.

In conclusion, I presented an analysis of laser-induced ultrafast demagnetization and magnetization precession in metallic heterostructures, which is complemented by measurements and modeling of strain dynamics. I demonstrated that the evaluation of models describing ultrafast dynamics in solids benefits greatly from the combination of MOKE and UXRD due to the close link between the interacting subsystems, which in turn determine the macroscopic dynamics. However, as the study of precession in particular shows, the combination not only brings advantages in terms of understanding processes on a microscopic level, but also provides fundamental insights regarding the direct relation of lattice and magnetization.

Bibliography

[1] Oleksandr Kovalenko, Thomas Pezeril, and Vasily V Temnov. New concept for magnetization switching by ultrafast acoustic pulses. *Physical review letters*, 110(26):266602, 2013.

[2] Ilya Razdolski, Alexandr Alekhin, Nikita Ilin, Jan P Meyburg, Vladimir Roddatis, Detlef Diesing, Uwe Bovensiepen, and Alexey Melnikov. Nanoscale interface confinement of ultrafast spin transfer torque driving non-uniform spin dynamics. *Nature communications*, 8(1):15007, 2017.

[3] A Stupakiewicz, CS Davies, K Szerenos, D Afanasiev, KS Rabinovich, AV Boris, Andrea Caviglia, AV Kimel, and A Kirilyuk. Ultrafast phononic switching of magnetization. *Nature Physics*, 17(4):489–492, 2021.

[4] Junta Igarashi, Wei Zhang, Quentin Remy, Eva Díaz, Jun-Xiao Lin, Julius Hohlfeld, Michel Hehn, Stéphane Mangin, Jon Gorchon, and Grégory Malinowski. Optically induced ultrafast magnetization switching in ferromagnetic spin valves. *Nature Materials*, pages 1–6, 2023.

[5] Eric Beaurepaire, J-C Merle, A Daunois, and J-Y Bigot. Ultrafast spin dynamics in ferromagnetic nickel. *Physical review letters*, 76(22):4250, 1996.

[6] J Hohlfeld, E Matthias, R Knorren, and KH Bennemann. Nonequilibrium magnetization dynamics of nickel. *Physical review letters*, 78(25):4861, 1997.

[7] C Stamm, N Pontius, T Kachel, M Wietstruk, and HA Dürr. Femtosecond x-ray absorption spectroscopy of spin and orbital angular momentum in photoexcited ni films during ultrafast demagnetization. *Physical Review B*, 81(10):104425, 2010.

[8] M Van Kampen, C Jozsa, JT Kohlhepp, P LeClair, Liesbet Lagae, WJM De Jonge, and B Koopmans. All-optical probe of coherent spin waves. *Physical review letters*, 88(22):227201, 2002.

[9] M Van Kampen, B Koopmans, JT Kohlhepp, and WJM De Jonge. Laser-induced precession in canted-spin ferromagnets. *Journal of magnetism and magnetic materials*, 240(1-3):291–293, 2002.

[10] Ji-Wan Kim, Mircea Vomir, and Jean-Yves Bigot. Ultrafast magnetoacoustics in nickel films. *Physical review letters*, 109(16):166601, 2012.

[11] Sabine Alebrand, Matthias Gottwald, Michel Hehn, Daniel Steil, Mirko Cinchetti, Daniel Lacour, Eric E Fullerton, Martin Aeschlimann, and Stéphane Mangin. Light-induced magnetization reversal of high-anisotropy tbco alloy films. *Applied Physics Letters*, 101(16):162408, 2012.

[12] Stéphane Mangin, M Gottwald, CH Lambert, D Steil, V Uhlíř, L Pang, Michel Hehn, S Alebrand, M Cinchetti, Grégory Malinowski, et al. Engineered materials for all-optical helicity-dependent magnetic switching. *Nature materials*, 13(3):286–292, 2014.

[13] Claudiu D Stanciu, Fredrik Hansteen, Alexey V Kimel, Andrei Kirilyuk, Arata Tsukamoto, Achioshi Itoh, and Th Rasing. All-optical magnetic recording with circularly polarized light. *Physical review letters*, 99(4):047601, 2007.

[14] Jan-Etienne Pudell, Maximilian Mattern, Michel Hehn, Grégory Malinowski, Marc Herzog, and Matias Bargheer. Heat transport without heating?—an ultrafast x-ray perspective into a metal heterostructure. *Advanced Functional Materials*, 30(46):2004555, 2020.

[15] Marc Herzog, Alexander von Reppert, Jan-Etienne Pudell, Carsten Henkel, Matthias Kronseder, Christian H Back, Alexei A Maznev, and Matias Bargheer. Phonon-dominated energy transport in purely metallic heterostructures. *Advanced Functional Materials*, 32(41):2206179, 2022.

[16] M Mattern, A von Reppert, SP Zeuschner, J-E Pudell, F Kühne, D Diesing, M Herzog, and M Bargheer. Electronic energy transport in nanoscale au/fe hetero-structures in the perspective of ultrafast lattice dynamics. *Applied Physics Letters*, 120(9):092401, 2022.

[17] Nicolas Bergeard, Michel Hehn, Stéphane Mangin, Gwladys Lengaigne, François Montaigne, MLM Lalieu, B Koopmans, and Grégory Malinowski. Hot-electron-induced ultrafast demagnetization in co/pt multilayers. *Physical review letters*, 117(14):147203, 2016.

[18] Yong Xu, Marwan Deb, Grégory Malinowski, Michel Hehn, Weisheng Zhao, and Stéphane Mangin. Ultrafast magnetization manipulation using single femtosecond light and hot-electron pulses. *Advanced Materials*, 29(42):1703474, 2017.

[19] Gerard Salvatella, Rafael Gort, Kevin Bühlmann, Simon Däster, Andreas Vaterlaus, and Y Acremann. Ultrafast demagnetization by hot electrons: Diffusion or super-diffusion? *Structural Dynamics*, 3(5):055101, 2016.

[20] Tom Ferté, Nicolas Bergeard, G Malinowski, R Abrudan, T Kachel, K Holldack, Michel Hehn, and Christine Boeglin. Ultrafast hot-electron induced quenching of tb 4 f magnetic order. *Physical Review B*, 96(14):144427, 2017.

[21] T Ferté, N Bergeard, G Malinowski, E Terrier, L Le Guyader, K Holldack, M Hehn, and C Boeglin. Ultrafast demagnetization in buried co80dy20 as fingerprint of hot-electron transport. *Journal of Magnetism and Magnetic Materials*, 485:320–324, 2019.

[22] I Radu, K Vahaplar, C Stamm, T Kachel, N Pontius, HA Dürr, TA Ostler, J Barker, RFL Evans, RW Chantrell, et al. Transient ferromagnetic-like state mediating ultrafast reversal of antiferromagnetically coupled spins. *Nature*, 472(7342):205–208, 2011.

[23] TA Ostler, J Barker, RFL Evans, RW Chantrell, U Atxitia, O Chubykalo-Fesenko, S El Moussaoui, LBPJ Le Guyader, E Mengotti, LJ Heyderman, et al. Ultrafast heating as a sufficient stimulus for magnetization reversal in a ferrimagnet. *Nature communications*, 3(1):666, 2012.

[24] Ettore Carpene, Eduardo Mancini, D Dazzi, Claudia Dallera, Ezio Puppin, and Sandro De Silvestri. Ultrafast three-dimensional magnetization precession and magnetic anisotropy of a photoexcited thin film of iron. *Physical Review B*, 81(6):060415, 2010.

[25] TP Ma, SF Zhang, Y Yang, ZH Chen, HB Zhao, and YZ Wu. Distinguishing the laser-induced spin precession excitation mechanism in fe/mgo (001) through field orientation dependent measurements. *Journal of Applied Physics*, 117(1):013903, 2015.

[26] J-Y Bigot, M Vomir, LHF Andrade, and E Beaurepaire. Ultrafast magnetization dynamics in ferromagnetic cobalt: The role of the anisotropy. *Chemical physics*, 318(1-2):137–146, 2005.

[27] Yooleemi Shin, Mircea Vomir, Dong-Hyun Kim, Phuoc Cao Van, Jong-Ryul Jeong, and Ji-Wan Kim. Quasi-static strain governing ultrafast spin dynamics. *Communications Physics*, 5(1):56, 2022.

[28] AV Scherbakov, AS Salasyuk, AV Akimov, X Liu, M Bombeck, C Brüggemann, DR Yakovlev, VF Sapega, JK Furdyna, and M Bayer. Coherent magnetization precession in ferromagnetic (ga, mn) as induced by picosecond acoustic pulses. *Physical review letters*, 105(11):117204, 2010.

[29] M Bombeck, JV Jäger, AV Scherbakov, T Linnik, DR Yakovlev, X Liu, JK Furdyna, AV Akimov, and M Bayer. Magnetization precession induced by quasitransverse picosecond strain pulses in (311) ferromagnetic (ga, mn) as. *Physical Review B*, 87(6):060302, 2013.

[30] Ji-Wan Kim, Mircea Vomir, and Jean-Yves Bigot. Controlling the spins angular momentum in ferromagnets with sequences of picosecond acoustic pulses. *Scientific reports*, 5(1):8511, 2015.

[31] SP Zeuschner, Tymur Parpiiev, Thomas Pezeril, Arnaud Hillion, Karine Dumesnil, Abdelmadjid Anane, J Pudell, Lisa Willig, Matthias Rössle, Marc Herzog, et al. Tracking picosecond strain pulses in heterostructures that exhibit giant magnetostriction. *Structural Dynamics*, 6(2):024302, 2019.

[32] Steffen Peer Zeuschner, Xi-Guang Wang, Marwan Deb, Elena Popova, Gregory Malinowski, Michel Hehn, Niels Keller, Jamal Berakdar, and Matias Bargheer. Standing spin wave excitation in bi: Yig films via temperature-induced anisotropy changes and magneto-elastic coupling. *Physical Review B*, 106(13):134401, 2022.

[33] Alexander von Reppert, Maximilian Mattern, J-E Pudell, Steffen Peer Zeuschner, Karine Dumesnil, and Matias Bargheer. Unconventional picosecond strain pulses resulting from the saturation of magnetic stress within a photoexcited rare earth layer. *Structural Dynamics*, 7(2):024303, 2020.

[34] Maximilian Mattern, Alexander von Reppert, Steffen Peer Zeuschner, Jan-Etienne Pudell, Marc Herzog, and Matias Bargheer. Concepts and use cases for picosecond ultrasonics with x-rays. *arXiv preprint arXiv:2302.14116*, 2023.

[35] Daniela Zahn, Florian Jakobs, Yoav William Windsor, Hélène Seiler, Thomas Vasileiadis, Tim A Butcher, Yingpeng Qi, Dieter Engel, Unai Atxitia, Jan Vorberger, et al. Lattice dynamics and ultrafast energy flow between electrons, spins, and phonons in a 3d ferromagnet. *Physical Review Research*, 3(2):023032, 2021.

[36] Andre Bojahr, Marc Herzog, Steffen Mitzscherling, Lena Maerten, Daniel Schick, J Goldshteyn, Wolfram Leitenberger, R Shayduk, P Gaal, and Matias Bargheer. Brillouin scattering of visible and hard x-ray photons from optically synthesized phonon wavepackets. *Optics express*, 21(18):21188–21197, 2013.

[37] C Thomsen, Holger T Grahn, Humphrey J Maris, and Jan Tauc. Surface generation and detection of phonons by picosecond light pulses. *Physical Review B*, 34(6):4129, 1986.

[38] Oliver B Wright. Ultrafast nonequilibrium stress generation in gold and silver. *Physical Review B*, 49(14):9985, 1994.

[39] Matthieu Nicoul, Uladzimir Shymanovich, Alexander Tarasevitch, Dietrich von der Linde, and Klaus Sokolowski-Tinten. Picosecond acoustic response of a laser-heated gold-film studied with time-resolved x-ray diffraction. *Applied Physics Letters*, 98(19):191902, 2011.

[40] T Saito, O Matsuda, and OB Wright. Picosecond acoustic phonon pulse generation in nickel and chromium. *Physical Review B*, 67(20):205421, 2003.

[41] John Kerr. Xliii. on rotation of the plane of polarization by reflection from the pole of a magnet. *The London, Edinburgh, and Dublin Philosophical Magazine and Journal of Science*, 3(19):321–343, 1877.

[42] Andrei Kirilyuk, Alexey V Kimel, and Theo Rasing. Ultrafast optical manipulation of magnetic order. *Reviews of Modern Physics*, 82(3):2731, 2010.

[43] Alexander von Reppert. *Magnetic strain contributions in laser-excited metals studied by time-resolved X-ray diffraction*. PhD thesis, University of Potsdam, Institute for Physics and Astronomy, 2021.

[44] Jean-Yves Bigot and Mircea Vomir. Ultrafast magnetization dynamics of nanostructures. *Annalen der Physik*, 525(1-2):2–30, 2013.

[45] Alexander Block, Matz Liebel, Renwen Yu, Marat Spector, Yonatan Sivan, FJ García de Abajo, and Niek F van Hulst. Tracking ultrafast hot-electron diffusion in space and time by ultrafast thermomodulation microscopy. *Science advances*, 5(5):eaav8965, 2019.

[46] Alexey Melnikov, Ilya Razdolski, Tim O Wehling, Evangelos Th Papaioannou, Vladimir Roddatis, Paul Fumagalli, Oleg Aktsipetrov, Alexander I Lichtenstein, and Uwe Bovensiepen. Ultrafast transport of laser-excited spin-polarized carriers in au/fe/mgo (001). *Physical review letters*, 107(7):076601, 2011.

[47] AIH Persson, Amélie Jarnac, Xiaocui Wang, H Enquist, A Jurgilaitis, and Jörgen Larsson. Studies of electron diffusion in photo-excited ni using time-resolved x-ray diffraction. *Applied Physics Letters*, 109(20):203115, 2016.

[48] H-S Rhie, HA Dürr, and W Eberhardt. Femtosecond electron and spin dynamics in n i/w (110) films. *Physical review letters*, 90(24):247201, 2003.

[49] Phoebe Tengdin, Wenjing You, Cong Chen, Xun Shi, Dmitriy Zusin, Yingchao Zhang, Christian Gentry, Adam Blonsky, Mark Keller, Peter M Oppeneer, et al. Critical behavior within 20 fs drives the out-of-equilibrium laser-induced magnetic phase transition in nickel. *Science advances*, 4(3):eaap9744, 2018.

[50] Zhibin Lin, Leonid V Zhigilei, and Vittorio Celli. Electron-phonon coupling and electron heat capacity of metals under conditions of strong electron-phonon nonequilibrium. *Physical Review B*, 77(7):075133, 2008.

[51] J Pudell, AA Maznev, Marc Herzog, M Kronseder, Christian H Back, Gregory Malinowski, Alexander von Reppert, and Matias Bargheer. Layer specific observation of slow thermal equilibration in ultrathin metallic nanostructures by femtosecond x-ray diffraction. *Nature communications*, 9(1):1–7, 2018.

[52] C Thomsen, J Strait, Z Vardeny, Humphrey J Maris, J Tauc, and JJ Hauser. Coherent phonon generation and detection by picosecond light pulses. *Physical review letters*, 53(10):989, 1984.

[53] Pascal Ruello and Vitalyi E Gusev. Physical mechanisms of coherent acoustic phonons generation by ultrafast laser action. *Ultrasonics*, 56:21–35, 2015.

[54] HB Zhao, D Talbayev, QG Yang, G Lüpke, AT Hanbicki, CH Li, OMJ van't Erve, G Kioseoglou, and BT Jonker. Ultrafast magnetization dynamics of epitaxial fe films on algaas (001). *Applied Physics Letters*, 86(15):152512, 2005.

[55] Lisa Willig, Alexander von Reppert, Marwan Deb, F Ganss, O Hellwig, and Matias Bargheer. Finite-size effects in ultrafast remagnetization dynamics of fept. *Physical Review B*, 100(22):224408, 2019.

[56] Osamu Matsuda, Maria Cristina Larciprete, Roberto Li Voti, and Oliver B Wright. Fundamentals of picosecond laser ultrasonics. *Ultrasonics*, 56:3–20, 2015.

[57] Rudolf Gross, Achim Marx, Dietrich Einzel, and Stephan Geprägs. Festkörperphysik. In *Festkörperphysik*. de Gruyter, 2018.

[58] Daniel Schick. udkm1dsim–a python toolbox for simulating 1d ultrafast dynamics in condensed matter. *Computer Physics Communications*, 266:108031, 2021.

[59] M Mattern, J-E Pudell, G Laskin, A von Reppert, and Matias Bargheer. Analysis of the temperature-and fluence-dependent magnetic stress in laser-excited srruo3. *Structural Dynamics*, 8(2):024302, 2021.

[60] Joachim Stöhr and Hans Christoph Siegmann. Magnetism. *Solid-State Sciences. Springer, Berlin, Heidelberg*, 5:236, 2006.

[61] John MD Coey. *Magnetism and magnetic materials*. Cambridge university press, 2010.

[62] J Crangle and GM Goodman. The magnetization of pure iron and nickel. *Proceedings of the Royal Society of London. A. Mathematical and Physical Sciences*, 321(1547):477–491, 1971.

[63] Peter J Meschter, James W Wright, Charlie R Brooks, and Thomas G Kollie. Physical contributions to the heat capacity of nickel. *Journal of Physics and Chemistry of Solids*, 42(9):861–871, 1981.

[64] B Koopmans, G Malinowski, F Dalla Longa, D Steiauf, M Fähnle, T Roth, M Cinchetti, and M Aeschlimann. Explaining the paradoxical diversity of ultrafast laser-induced demagnetization. *Nature materials*, 9(3):259–265, 2010.

[65] Marco Battiato, Karel Carva, and Peter M Oppeneer. Superdiffusive spin transport as a mechanism of ultrafast demagnetization. *Physical review letters*, 105(2):027203, 2010.

[66] Marco Battiato, Karel Carva, and Peter M Oppeneer. Theory of laser-induced ultrafast superdiffusive spin transport in layered heterostructures. *Physical Review B*, 86(2):024404, 2012.

[67] Gregory Malinowski, F Dalla Longa, JHH Rietjens, PV Paluskar, R Huijink, HJM Swagten, and B Koopmans. Control of speed and efficiency of ultrafast demagnetization by direct transfer of spin angular momentum. *Nature Physics*, 4(11):855–858, 2008.

[68] Christian Dornes, Yves Acremann, Matteo Savoini, Martin Kubli, Martin J Neugebauer, Elsa Abreu, Lucas Huber, Gabriel Lantz, Carlos AF Vaz, Henrik Lemke, et al. The ultrafast einstein–de haas effect. *Nature*, 565(7738):209–212, 2019.

[69] Sonja R Tauchert, Mikhail Volkov, Dominik Ehberger, D Kazenwadel, Martin Evers, Hannah Lange, Andreas Donges, Alexander Book, W Kreuzpaintner, U Nowak, et al. Polarized phonons carry angular momentum in ultrafast demagnetization. *Nature*, 602(7895):73–77, 2022.

[70] Emrah Turgut, Justin M Shaw, Patrik Grychtol, Hans T Nembach, Dennis Rudolf, Roman Adam, Martin Aeschlimann, Claus M Schneider, Thomas J Silva, Margaret M Murnane, et al. Controlling the competition between optically induced ultrafast spin-flip scattering and spin transport in magnetic multilayers. *Physical review letters*, 110(19):197201, 2013.

[71] TL Linnik, AV Scherbakov, DR Yakovlev, X Liu, JK Furdyna, and M Bayer. Theory of magnetization precession induced by a picosecond strain pulse in ferromagnetic semiconductor (ga, mn) as. *Physical Review B*, 84(21):214432, 2011.

[72] L Baselgia, M Warden, F Waldner, Stuart L Hutton, John E Drumheller, YQ He, PE Wigen, and M Maryško. Derivation of the resonance frequency from the free energy of ferromagnets. *Physical Review B*, 38(4):2237, 1988.

[73] H-P Klein and E Kneller. Variation of magnetocrystalline anisotropy of iron with field and temperature. *Physical Review*, 144(2):372, 1966.

[74] VN Kats, TL Linnik, AS Salasyuk, AW Rushforth, M Wang, P Wadley, Andrey V Akimov, SA Cavill, V Holy, AM Kalashnikova, et al. Ultrafast changes of magnetic anisotropy driven by laser-generated coherent and noncoherent phonons in metallic films. *Physical Review B*, 93(21):214422, 2016.

[75] Ji-Wan Kim and Jean-Yves Bigot. Magnetization precession induced by picosecond acoustic pulses in a freestanding film acting as an acoustic cavity. *Physical Review B*, 95(14):144422, 2017.

[76] Wei-Gang Yang and Holger Schmidt. Acoustic control of magnetism toward energy-efficient applications. *Applied Physics Reviews*, 8(2):021304, 2021.

[77] AA Rzhevsky, BB Krichevtsov, DE Bürgler, and CM Schneider. Magnetization dynamics induced by ultrashort optical pulses in fe/ cr thin films. *Physical Review B*, 75(22):224434, 2007.

[78] S Tanuma, T Shiratori, Tetsuya Kimura, K Goto, S Ichimura, and Cedric J Powell. Experimental determination of electron inelastic mean free paths in 13 elemental solids in the 50 to 5000 ev energy range by elastic-peak electron spectroscopy. *Surface and Interface Analysis*, 37(11):833–845, 2005.

[79] Nicolas Bergeard, Michel Hehn, Karel Carva, Pavel Baláž, Stéphane Mangin, and Gregory Malinowski. Tailoring femtosecond hot-electron pulses for ultrafast spin manipulation. *Applied Physics Letters*, 117(22):222408, 2020.

[80] Renjun Zhang and Roy F Willis. Thickness-dependent curie temperatures of ultrathin magnetic films: effect of the range of spin-spin interactions. *Physical review letters*, 86(12):2665, 2001.

[81] F Huang, MT Kief, GJ Mankey, and RF Willis. Magnetism in the few-monolayers limit: A surface magneto-optic kerr-effect study of the magnetic behavior of ultrathin films of co, ni, and co-ni alloys on cu (100) and cu (111). *Physical Review B*, 49(6):3962, 1994.

[82] Flavio Zamponi, Zunaira Ansari, C v Korff Schmising, Philip Rothhardt, Nickolai Zhavoronkov, Michael Woerner, Thomas Elsaesser, Matias Bargheer, Timo Trobitzsch-Ryll, and Michael Haschke. Femtosecond hard x-ray plasma sources with a kilohertz repetition rate. *Applied Physics A*, 96:51–58, 2009.

[83] Daniel Schick, Andre Bojahr, Marc Herzog, C von Korff Schmising, Roman Shayduk, Wolfram Leitenberger, P Gaal, and Matias Bargheer. Normalization schemes for ultrafast x-ray diffraction using a table-top laser-driven plasma source. *Review of Scientific Instruments*, 83(2):025104, 2012.

[84] Des McMorrow and Jens Als-Nielsen. *Elements of modern x-ray physics*. John Wiley & Sons, 2011.

[85] PS Pershan. Magneto-optical effects. *Journal of applied physics*, 38(3):1482–1490, 1967.

[86] Jaroslav Hamrle. *Magneto-optical determination of the in-depth magnetization profile in magnetic multilayers*. PhD thesis, Université Paris Sud-Paris XI, 2003.

[87] Michael Faraday. I. experimental researches in electricity.—nineteenth series. *Philosophical Transactions of the Royal Society of London*, 136:1–20, 1846.

[88] Pieter M Oppeneer. *Theory of the magneto-optical Kerr effect in ferromagnetic compounds*. PhD thesis, TU Dresden, 1999.

[89] H Ebert. Magneto-optical effects in transition metal systems. *Reports on Progress in Physics*, 59(12):1665, 1996.

[90] Satoru Sugano and Norimichi Kojima. *Magneto-optics*, volume 128. Springer Science & Business Media, 2013.

[91] Paul Fumagalli and Joachim Schoenes. *Magneto-optics: An introduction*. Walter de Gruyter GmbH & Co KG, 2021.

[92] P Babilotte, E Morozov, P Ruello, D Mounier, M Edely, JM Breteau, A Bulou, and V Gusev. Physical mechanism of coherent acoustic phonons generation and detection in gaas semiconductor. In *Journal of Physics: Conference Series*, volume 92, page 012019. IOP Publishing, 2007.

[93] P Babilotte, P Ruello, D Mounier, Thomas Pezeril, G Vaudel, M Edely, Jean-Marc Breteau, V Gusev, and K Blary. Femtosecond laser generation and detection of high-frequency acoustic phonons in gaas semiconductors. *Physical Review B*, 81(24):245207, 2010.

[94] ESK Young, AV Akimov, RP Campion, AJ Kent, and V Gusev. Picosecond strain pulses generated by a supersonically expanding electron-hole plasma in gaas. *Physical Review B*, 86(15):155207, 2012.

[95] J Hohlfeld, S-S Wellershoff, J Güdde, U Conrad, V Jähnke, and E Matthias. Electron and lattice dynamics following optical excitation of metals. *Chemical Physics*, 251(1-3):237–258, 2000.

[96] V Yu Bodryakov. Correlation between temperature dependences of thermal expansivity and heat capacity up to the melting point of tantalum. *High Temperature*, 54(3):316–321, 2016.

[97] Roman Shayduk, Vedran Vonk, Björn Arndt, Dirk Franz, Jörg Strempfer, Sonia Francoual, Thomas F Keller, Tobias Spitzbart, and Andreas Stierle. Nanosecond laser pulse heating of a platinum surface studied by pump-probe x-ray diffraction. *Applied Physics Letters*, 109(4):043107, 2016.

[98] HE Elsayed-Ali, TB Norris, MA Pessot, and GA Mourou. Time-resolved observation of electron-phonon relaxation in copper. *Physical Review Letters*, 58(12):1212, 1987.

[99] THK Barron, WT Berg, and JA Morrison. On the heat capacity of crystalline magnesium oxide. *Proceedings of the Royal Society of London. Series A. Mathematical and Physical Sciences*, 250(1260):70–83, 1959.

[100] Corning Incorporated. *Corning 1737 AMLCD Glass*, 2002.

[101] MJ Duggin. The thermal conductivities of aluminium and platinum. *Journal of Physics D: Applied Physics*, 3(5):L21, 1970.

[102] X Zheng, DG Cahill, P Krasnochtchekov, RS Averback, and J-C Zhao. High-throughput thermal conductivity measurements of nickel solid solutions and the applicability of the wiedemann–franz law. *Acta Materialia*, 55(15):5177–5185, 2007.

[103] IV Savchenko and SV Stankus. Thermal conductivity and thermal diffusivity of tantalum in the temperature range from 293 to 1800 k. *Thermophysics and Aeromechanics*, 15(4):679–682, 2008.

[104] Glen A Slack. Thermal conductivity of mgo, al 2 o 3, mg al 2 o 4, and fe 3 o 4 crystals from 3° to 300° k. *Physical Review*, 126(2):427, 1962.

[105] RE Macfarlane, JA Rayne, and CK Jones. Anomalous temperature dependence of shear modulus c 44 for platinum. *Physics Letters*, 18(2):91–92, 1965.

[106] HM Ledbetter and ER Naimon. Elastic properties of metals and alloys. ii. copper. *Journal of physical and chemical reference data*, 3(4):897–935, 1974.

[107] JR Neighbours, FW Bratten, and Charles S Smith. The elastic constants of nickel. *Journal of Applied Physics*, 23(4):389–393, 1952.

[108] Frank H Featherston and JR Neighbours. Elastic constants of tantalum, tungsten, and molybdenum. *Physical Review*, 130(4):1324, 1963.

[109] Orson L Anderson and P Andreatch Jr. Pressure derivatives of elastic constants of single-crystal mgo at 23° and-195.8° c. *Journal of the American Ceramic Society*, 49(8):404–409, 1966.

[110] Rappal Sangameswara Krishnan, Ramachandran Srinivasan, and S Devanarayanan. *Thermal expansion of crystals: international series in the science of the solid state*. Elsevier, 1979.

[111] AS Rao and K Narender. Studies on thermophysical properties of cao and mgo by-ray attenuation. *Journal of Thermodynamics*, 2014, 2014.

[112] André Bojahr, Marc Herzog, Daniel Schick, Ionela Vrejoiu, and Matias Bargheer. Calibrated real-time detection of nonlinearly propagating strain waves. *Physical Review B*, 86(14):144306, 2012.

[113] Hyejin Jang, Johannes Kimling, and David G Cahill. Nonequilibrium heat transport in pt and ru probed by an ultrathin co thermometer. *Physical Review B*, 101(6):064304, 2020.

[114] Wenjing You, Phoebe Tengdin, Cong Chen, Xun Shi, Dmitriy Zusin, Yingchao Zhang, Christian Gentry, Adam Blonsky, Mark Keller, Peter M Oppeneer, et al. Revealing the nature of the ultrafast magnetic phase transition in ni by correlating extreme ultraviolet magneto-optic and photoemission spectroscopies. *Physical review letters*, 121(7):077204, 2018.

[115] Bert Koopmans, JJM Ruigrok, Francesco Dalla Longa, and WJM De Jonge. Unifying ultrafast magnetization dynamics. *Physical review letters*, 95(26):267207, 2005.

[116] T Roth, AJ Schellekens, S Alebrand, O Schmitt, D Steil, B Koopmans, M Cinchetti, and M Aeschlimann. Temperature dependence of laser-induced demagnetization in ni: A key for identifying the underlying mechanism. *Physical Review X*, 2(2):021006, 2012.

[117] T Chase, M Trigo, AH Reid, R Li, T Vecchione, X Shen, S Weathersby, R Coffee, N Hartmann, DA Reis, et al. Ultrafast electron diffraction from non-equilibrium phonons in femtosecond laser heated au films. *Applied Physics Letters*, 108(4):041909, 2016.

[118] Lutz Waldecker, Roman Bertoni, Ralph Ernstorfer, and Jan Vorberger. Electron-phonon coupling and energy flow in a simple metal beyond the two-temperature approximation. *Physical Review X*, 6(2):021003, 2016.

[119] Lutz Waldecker, Roman Bertoni, H Hübener, Thomas Brumme, Thomas Vasileiadis, Daniela Zahn, Angel Rubio, and Ralph Ernstorfer. Momentum-resolved view of electron-phonon coupling in multilayer wse 2. *Physical Review Letters*, 119(3):036803, 2017.

[120] Pablo Maldonado, T Chase, AH Reid, X Shen, RK Li, K Carva, T Payer, M Horn Von Hoegen, K Sokolowski-Tinten, XJ Wang, et al. Tracking the ultrafast nonequilibrium energy flow between electronic and lattice degrees of freedom in crystalline nickel. *Physical Review B*, 101(10):100302, 2020.

[121] Pablo Maldonado, Karel Carva, Martina Flammer, and Peter M Oppeneer. Theory of out-of-equilibrium ultrafast relaxation dynamics in metals. *Physical Review B*, 96(17):174439, 2017.

[122] Charles Kittel. On the theory of ferromagnetic resonance absorption. *Physical review*, 73(2):155, 1948.

[123] Mathias Weiler, Lukas Dreher, Christian Heeg, Hans Huebl, Rudolf Gross, Martin S Brandt, and Sebastian TB Gönnenwein. Elastically driven ferromagnetic resonance in nickel thin films. *Physical review letters*, 106(11):117601, 2011.

[124] Lukas Dreher, Mathias Weiler, Matthias Pernpeintner, Hans Huebl, Rudolf Gross, Martin S Brandt, and Sebastian TB Gönnenwein. Surface acoustic wave driven ferromagnetic resonance in nickel thin films: Theory and experiment. *Physical Review B*, 86(13):134415, 2012.

Danksagung

Zum Abschluss möchte ich die Gelegenheit nutzen, um mich bei einer Reihe von Personen zu bedanken, die Anteil an der Entstehung dieser Arbeit haben und mich auch darüber hinaus unterstützt und geprägt haben.

Zunächst möchte ich Prof. Matias Bargheer ganz herzlich für die Unterstützung, durch die ich viel lernen konnte, und seine stetige Ermutigung danken, über meine Komfortzone hinauszugehen. Deine zahlreichen Impulse und Gedankenantöße haben den Fortschritt dieser Arbeit enorm begünstigt und diese sehr bereichert. Sein Enthusiasmus haben immer wieder aufs Neue die Faszination und Wissbegierde in mir geweckt, die mich zu allen Mühen motivieren.

Ganz besonders danke ich Alexander von Reppert für seine stetige Betreuung und richtungsweisende Hilfestellung während meiner gesamten Zeit in der UDKM. Ich bewundere sehr, wie du mit deinem breiten Wissen stets allen zur Seite stehst, und bin sehr dankbar, dass auch ich zu den Leuten zähle, die deine Unterstützung erfahren haben und von dir lernen durften. Ich hoffe, dass ich dies irgendwann mit ebenso viel Einsatz und Engagement weitergeben kann.

Weiterhin danke ich Maximilian Mattern für seine fachliche Unterstützung aber vor allem auch für sein stets offenes Ohr und seine immense Hilfsbereitschaft. Unsere Gespräche über Physik sowie darüber hinaus haben mir stets geholfen, meine Gedanken zu sortieren.

Nicht unerwähnt möchte ich die übrigen Mitglieder der UDKM-Arbeitsgruppe der Uni Potsdam lassen, die durch ihre unheimlich freundliche und offene Art maßgeblich dazu beigetragen haben, dass ich motiviert und mit Freude zur Uni gekommen bin.

Dank euch allen wird mein Physikstudium immer eine unvergessliche Zeit bleiben.

Abschließend möchte ich mich bei meinen Freunden bedanken, die mit viel Geduld mein Einsiedler-Dasein in Phasen intensiver Arbeit akzeptieren und mir weiterhin zur Seite stehen. Ich bin wirklich dankbar dafür, da das nicht selbstverständlich ist.

Und zuallerletzt gilt mein ganz besonderer Dank meinen Eltern und meiner Schwester. Ihr seid mir der größte Rückhalt überhaupt durch euren Glauben an mich, eure Unterstützung und euren Rat. Ihr bietet mir ein zu Hause, aus dem ich immer wieder neue Kraft schöpfen kann, die mich auf meinen Weg trägt.

Statement of Authorship

I hereby certify that this master thesis was written independently and without assistance from third parties. Other than the stated sources and aids were not used. Parts of the sources that have been used verbatim or in substance are identified as such. This master thesis has not been presented in the same or similar form to any audit authority and was not published.

Hiermit versichere ich, dass die vorliegende Masterarbeit selbstständig und ohne Hilfe Dritter verfasst habe. Andere als die angegebenen Quellen und Hilfsmittel wurden nicht verwendet. Die den benutzten Quellen wörtlich oder inhaltlich entnommenen Abschnitte sind als solche kenntlich gemacht. Diese Masterarbeit hat in gleicher oder ähnlicher Form noch keiner Prüfungsbehörde vorgelegen und wurde auch nicht veröffentlicht.

Potsdam, 30.04.2023   (Jasmin Jarecki)